THE CELL BIOLOGY OF CELLUOSE DEPOSITION IN SECONDARY CELL WALLS OF PROTOXYLEM TRACHEARY ELEMENTS IN *ARABIDOPSIS THALIANA*

by

Yoichiro Watanabe

B.Sc. The University of British Columbia, 2010

B.A. The University of British Columbia, 2010

A THESIS SUBMITTED IN PARTIAL FULFILLMENT OF

THE REQUIREMENTS FOR THE DEGREE OF

DOCTOR OF PHILOSOPHY

in

THE FACULTY OF GRADUATE AND POSTDOCTORAL STUDIES

(Botany)

THE UNIVERSITY OF BRITISH COLUMBIA

(Vancouver)

April 2018

Abstract

Cellulose is the most abundant polymer in nature and is a major component of both primary and secondary cell walls in plants. The cellulose produced in these different walls are synthesized by completely independent sets of non-redundant CELLULOSE SYNTHASE (CESA) enzymes. In the last decade, live cell imaging techniques have answered a number of fundamental questions regarding CESA dynamics and organization in the primary cell wall. However, attempts to repeat these experiments in cells producing secondary cell walls has been met with limited success due to the fact that cells forming secondary walls are deep inside plant organs. The development of an inducible system driving the ectopic expression of the master regulator for protoxylem tracheary element development, VASCULAR RELATED NAC-DOMAIN7 (VND7), has generated a valuable biological tool to track secondary cell wall synthesis via live-cell imaging.

With these tools, I was able to directly visualize secondary cell wall-specific CESA complexes moving around the plasma membrane, and to quantify that they move at a significantly faster rate than primary cell wall-specific complexes (Chapter 2). Additionally, bundling of the underlying cortical microtubules causes the densities of the CESA complexes to be much higher during secondary wall synthesis than during primary wall synthesis, giving a possible explanation for the rapid and abundant development of these walls (Chapter 2). Analysis of the transition from primary to secondary cell wall production revealed that primary wall-specific CESAs are selectively targeted into distinct pre-vacuolar compartments for degradation to the lytic vacuole, while secondary cell wall-specific CESAs accumulate (Chapter 3). Finally, *cesa* mutants were investigated to explore the effects of the loss of each of the three CESAs involved in secondary cell wall cellulose synthesis on both the wall patterning and localization of their interacting partners. While the loss of a CESA causes significant defects in secondary cell wall cellulose patterning, the loss of CESA7 specifically resulted in the complete loss in patterning, indicating a possible role for CESA7 in anchoring the CESA complexes to the underlying cortical microtubules. Taken together, these results refine our model of how plant cells coordinate their cellulose synthesis machinery during secondary cell wall production.

Lay Summary

Cellulose is a biopolymer made of glucose sugars linked end to end. It is an essential component of cell walls that surround each and every plant cell. Woody cells of the plant xylem are particularly rich in cellulose, which can make up over 50% of their cell walls, giving these cells their strength. Enzymes called cellulose synthases make cellulose at the surface of cells and extrude it into the cell wall. Using high-resolution microscopy, I directly observed and analyzed cellulose synthase enzymes during the development of xylem cells. I show that during their development, cells change the set of cellulose synthase enzymes that they use to make cellulose. Additionally, I show how the loss of one of the cellulose synthase enzymes affects the structure and patterning of cell walls. Together this work outlines how xylem cells control the behavior of cellulose synthesizing enzymes during formation of woody tissue.

Preface

A version of Chapter 1 has been published as part of a review article Meents, MJ, Watanabe, Y, and Samuels, AL (2017) The cell biology of secondary cell wall biosynthesis. *Annals of Botany*. The portion included in this thesis was written by Yoichiro Watanabe with the assistance of Miranda J Meents and A Lacey Samuels.

A version of Chapter 2 has been published as: Watanabe, Y, Meents MJ, McDonnell, LM, Barkwill, S, Sampathkumar, A, Cartwright, HN, Demura, T, Ehrhardt DW, Samuels AL and Mansfield SD (2015) Visualization of cellulose synthases in *Arabidopsis* secondary cell walls. *Science* **350**: 198-203 © Copyright American Association for the Advancement of Science, 2015 (DOI:10.1126/science.aac7446). Yoichiro Watanabe, Lacey Samuels, and Shawn Mansfield designed the research experiments. Yoichiro Watanabe with the assistance of Arun Sampathkumar and Heather N Cartwright performed all experiments except for TEM, which was carried out by Miranda J Meents, and cellulose content analysis which was carried out by Sarah Barkwill. Yoichiro Watanabe generated all figures. All authors contributed to the writing of the manuscript.

A version of Chapter 3 has been submitted as a research article for peer review. The project was conceived by Staffan Persson and Shawn D Mansfield. Experiments were designed by Yoichiro Watanabe, Rene Schneider, A Lacey Samuels, Staffan Persson and Shawn D Mansfield. Generation of plant lines was carried out by Sarah Barkwill and Yoichiro Watanabe. Microscopy experiments and data analysis were carried out by Yoichiro Watanabe and Rene Schneider. Cell wall analysis was carried out by Rene Schneider. Generation of antibodies was performed by Joseph L Hill. Westerns were performed by Eliana Gonzales-Vigil. Figures 3-1, 3-4 and 3-5 were generated by Rene Schneider, and Figure 3-9 was generated by Eliana Gonzales-Vigil. All remaining figures were generated by Yoichiro Watanabe. All authors contributed to the writing of the manuscript.

For Chapter 4, Taku Demura, A Lacey Samuels, Shawn D Mansfield, Yuto Takenaka and Yoichiro Watanabe identified the research question and designed the research. Plant

lines were generated by Yoichiro Watanabe with the assistance of Lynn Chen, Sarah B Barkwill, and Jan Xue. Fluorescently tagged CESA4 and CESA8 constructs were generated by Joseph L Hill. Yoichiro Watanabe performed all microscopy experiments and data analysis.

Table of Contents

List of Tables

List of Figures

List of Symbols

°C	Degrees Celsius
kDa	Kilo Dalton
g	grams
h	Hour(s)
L	Liter
µ	Micro (prefix) – 10^{-6}
m	Meters
M	Molar
MDa	Million Daltons
n	Nano (prefix) 10^{-9}

List of Abbreviations

At	*Arabidopsis thaliana*
bacl	*baculities-like* mutant
BcsA	Bacterial cellulose biosynthesis Subunit A protein
proCaMV35S	*Cauliflower Mosaic Virus 35S* Promoter
CC	COMPANION OF CELLULOSE protein
CESA	CELLULOSE SYNTHASE protein
CMU	CELLULOSE-MICROTUBLE UNCOUPLING protein
CoIP	Co-immunoprecipitation
Col-0	Columbia-0 Arabidopsis ecotype
CSC	Cellulose synthase complex
CSI	CELLULOSE SYNTHASE INTERACTING protein
CTL	CHITINASE-LIKE protein
DCB	2,6-dichlorobenzonitrile
DEX	Dexamethasone
DMSO	Dimethyl sulfoxide
DNA	Deoxyribonucleic acid
DP	Degree of polymerization
Ds	*Dissociation element* (transposable element)
eli	*ectopic lignin* mutant
et al.	*et alia* (Latin)
fra	*fragile fiber* mutant
FRAP	Fluorescence recovery after photobleaching
FTIR	Fourier-transform infrared spectroscopy
GFP	Green fluorescent protein
GH9	Glycosyl Hydrolase Family 9
GM	Germination media
GR	Glucocorticoid Receptor Protein
HCl	Hydrochloric acid
irx	*irregular xylem* mutant

LM10	Leeds Monoclonal Antibody 10 – epitope feruloyated 1,4-linked β-D-galactan
MDa	Million Daltons
MAP	Microtubule-Associated Protein
MASC	Microtubule-Associated CESA Compartment
MES	2-(*N*-morpholino)ethanesulfonic acid
min	Minute(s)
MFA	Microfibril angle
MS	Mursahige and Skoog medium
mRFP	Monomeric red fluorescent protein
mur	*murus* (from Latin meaning wall) mutant
NAC	NAM, ATAF, and CUC domain transcription factor
NG	Neon Green fluorescent protein
NMR	Nuclear Magnetic Resonance
PCW	Primary cell wall
PIPs	Phosphatidyl inositol phosphates
PI	Propidium iodide
PIP	Phosphatidylinositol phosphate
PM	Plasma membrane
pro	Promoter
RAB	Ras superfamily monomeric G protein
RHO-GTPase	RHO OF PLANT – Guanosine Triphosphatase
rsw	*radial swelling* mutant
S4B	Pontamine fast scarlet 4B dye
SCW	Secondary Cell Wall
SmaCC	Small CESA compartment
SuSy	SUCROSE SYNTHASE protein
T-DNA	Transfer-deoxyribonucleic acid
tdT	Tandem TOMATO fluorescent protein
TEM	Transmission electron microscopy
TUB	TUBULIN β subunit
UDP-Glucose	Uridine diphosphate glucose

UGPases	UDP-Glucose pyrophosphorylases
VND	VASCULAR-RELATED NAC DOMAIN transcription factor
Wm	Wortmannin
WT	*wild-type*
YFP	Yellow fluorescent protein

Acknowledgments

First and foremost, I want to thank my supervisors, Dr. A. Lacey Samuels and Dr. Shawn D. Mansfield. Not only have they given me this amazing opportunity to work on this project but both Lacey and Shawn have been amazing mentors giving me exceptional training, advice and support through my many years in their labs. Their seemingly unwavering faith in my abilities and their patience with me at times, is something I cannot thank them enough for.

To my all-star committee, Dr. Patrick Martone and Dr. Abel Rosado. Thank you for all the advice, support, helpful criticisms and insight into my research project and thesis. As well thank you for challenging me to think outside the box when it came to my research. I would also like to thank the late Dr. Carl Douglas who served on my committee and who provided me with exceptional insight and advice in my project especially during its early stages.

To Samuels and Mansfield lab members past and present, thank you for making the lab a wonderful place to work, and for being such amazing co-workers and friends! I'd like to give a special thanks to Dr. Heather McFarlane for being the best mentor a fledgling undergrad could ask for. As well, Dr. Mathias Schuetz for also being an awesome mentor and for being so providing such helpful insight and advice with at numerous stages of my research. Thank you to Miranda J. Meents for her support in running experiments and writing. To my previous undergraduate assistants, Kristen Chan, Anson Liu and Jan Xue for helping me at various stages of my project, especially when it came to generating constructs and plant lines.

I would also like to thank my amazing collaborators, Dr. Arun Sampathakumar, Dr. Heather Cartwright, Dr. David Ehrhardt, Dr. Rene Schneider, Dr. Staffan Persson, Dr. Joseph Hill, Dr. Yuto Takenaka and Dr. Taku Demura for working with me on these projects and for providing their expertise and assistance. These projects would not have been as successful without their help and insight.

Funding for this work was provided in the form of NSERC Post-Graduate Scholarship-Doctoral from Natural Sciences and Engineering Research Council of Canada, a Four Year Doctoral Fellowship from the University of British Columbia and Department of Botany Entrance Scholarship. Additional funding was provided from the Working on Walls CREATE grant which included support for travel to collaborating labs where several key pieces of data were generated.

Thank you to my parents, Takao and Phuong, and my sisters Mary and Sachiko for their love and support. Thank you to my friends, for all your support and words of encouragement. I would especially like to thank my friend Julie S. for all her help and advice. I would finally like to Michelle C. for her love, companionship, support and belief in me even through the most difficult of times.

Chapter 1: Introduction

Cellulose in plant secondary cell walls (SCW) imparts rigidity and strength, providing physiological support to the plant. In xylem tracheary elements, the cellulose in SCWs is deposited in specific patterned domains. This thesis explores how CELLULOSE SYNTHASE (CESA) enzyme complexes (CSC) are transported to and move through the plasma membrane (PM) of developing xylem cells, depositing this important and abundant biopolymer.

1.1 Plant cell walls and cellulose

One of the most important features of plants that has allowed them to dominate the terrestrial environment is their strong yet flexible matrix, the plant cell wall. This matrix of mainly polysaccharides is the main load-bearing structure of the plant at both the cellular and physiological levels. At the cellular level, the plant cell wall dictates the shape of the cell, allowing for the large variation in cell shapes seen in plants that are necessary for the various functions within the plant (reviewed in Doblin *et al.* 2010). Cell walls also resist the immense turgor pressure caused by the osmotic flow of water into the plant cell's vacuole. This turgor pressure is essential for plants to remain rigid at the physiological level, and the loss of this pressure results in plants losing their rigidity and eventually wilting (reviewed in Taiz and Zeiger 2015). The ability of cell walls to withstand immense pressure is also necessary for the plant to carry out transpiration, the process by which water is carried through the plant from its roots to the leaves. Additionally, at the physiological level, plant cell walls can also act as the main load-bearing component of the entire plant. This is especially true for larger plants such as trees and other plants with woody tissue in which the cell walls support the weight of the whole plant.

This immensely varied function of plant cell walls requires that the cell wall be structurally and compositionally plastic to allow for its various functions. One of the main categorical classifications for this variation are primary and secondary cell walls. Plant cell walls can be classified as either primary or secondary depending on when they were laid

down. The majority of all plant cell walls have a primary cell wall (PCW), which is laid down during cell division and expansion. One of the key roles of the PCW is to resist cellular turgor pressure, which is not only important for the rigidity of the plant but also an important driver of cell expansion. As such the PCW not only needs to be rigid enough to resist the forces exerted on it by turgidity but also flexible and extendable to allow for cell growth. The expansion of the wall is irreversible, involving the integration of new components into the extending wall preventing it from becoming thinner and weaker (reviewed in Cosgrove 2005).

Following PCW expansion, some cells, especially those associated with the vascular system, also form SCWs. By depositing a SCW, the cell greatly increases its rigidity and strength, providing physiological support for the overall plant and a means to accommodate long distance water transport in tracheids and vessel elements. These SCWs can be deposited in discrete regions and not throughout the entirety of cell, resulting in a range of complex patterns varying from spiral or hoop-like patterns to pitted or reticulate patterns (Esau, 1977). Though only a certain subset of cells form SCWs, in many woody plants such as trees, the majority of the plants mass is composed of SCWs.

Both the PCW and SCWs are mainly composed of a complex network of polysaccharides that are synthesized and deposited by the cell itself. Although similar in this sense, the two walls differ in composition of the polysaccharide network. For example, the matrix polysaccharides, pectin and hemicelluloses, differ extensively in relative abundance and polysaccharide make up between the two walls (Scheller and Ulvskov 2010; Harholt *et al.* 2010). For example, in many PCWs of dicot plants, pectins can compose up to 50% of the wall (Harholt *et al.* 2010) and use xyloglucan as the main hemicellulose (Cosgrove 2005). In contrast, SCWs of dicots usually contain little to no pectin and use glucoronoxylan as the main hemicellulose instead (Scheller and Ulvskov 2010). These heterogenic polysaccharide polymers are synthesized in the Golgi and exported via vesicles to the plasma membrane (PM) where they integrate into the cell wall via physical interactions, and enzymatic crosslinking reactions (Cosgrove 2005).

Further, lignin polymers found in SCWs further strengthen the cross-linked network of polysaccharides imparting increased strength and rigidity to the wall (Boerjan *et al.* 2003).

Despite these differences, both the PCW and SCWs use cellulose microfibrils as the major load bearing structural component of the wall. Cellulose is the most abundant polymer in the SCW (comprising up to 80%), and a major component in PCW (comprising between 20 to 30%) (reviewed in McNeil *et al.* 1984). As such, cellulose is often referred to the most abundant biopolymer on earth with an estimated annual production of 10^{10} to 10^{11} tons produced annually (Hon 1994). Cellulose is composed of linear, un-branched chains of glucose molecules polymerized from UDP-glucose (uridine diphosphate-glucose) linked by a β-(1-4) bonds (reviewed in Hon 1994). This β-(1-4) linkage between glucose molecules means that cellobiose is the primary repeating unit of cellulose and imparts a number of key physical and chemical properties that differ greatly from other linear glucose polymers such as starch (α-(1-4) linked) and callose (β-(1-3) linked) (Brown *et al.* 1996). One of the key properties that the β-(1-4) linkage imparts is the ability to form many intra- and intermolecular hydrogen bonds between cellulose chains (Kim *et al.* 2013). This leads to the aggregation of several chains to form crystalline arrays of parallel chains known as microfibrils. These insoluble, relatively inelastic, cable-like microfibrils wrap around the cells in spatially arranged overlapping layers serving as a scaffold for the matrix polysaccharides, and in the SCWs, lignin polymers, that make up the remainder of the cell wall (Schneider *et al.* 2016).

The overall structure of the cellulose microfibrils can be quite varied and does differ between PCW and SCWs (McNeil *et al.* 1984). The crystalline state, and therefore the degree of crystallinity, of these microfibrils is one of the features that can differ and is determined by the arrangement of the individual chains with respect to each other within the array (Brown and Saxena 2007). In nature, the most common crystalline state (allomorph) of cellulose produced is cellulose I, which can be further divided into two sub-allomorphs, cellulose Iα and Iβ, which differ slightly in respect to arrangement of hydrogen bonding, molecular conformation and crystal structure (VanderHart *et al.* 1984; Nishiyama 2009). Although the amounts of each sub-allomorph vary among organisms

(e.g. algae and bacteria are rich in Iα, while many vascular plants are rich in Iβ), each microfibril can contain both types, and some of the physical properties of the microfibril will depend on this ratio (VanderHart *et al.* 1984; Brown and Saxena 2007). How this ratio and therefore the degree of crystallinity is controlled during synthesis is still not understood.

Another important feature of cellulose is the degree of polymerization (DP) of the cellulose chain. The range in DP of vascular plants can be quite large, however, generally the DP in the PCWs (~ 2000 glucose molecules) is much shorter than the DP of cellulose in SCWs (greater than 8000) (McNeil *et al.* 1984; Joshi and Mansfield 2007). However, like crystallinity, what cellular and enzymatic processes control this remains poorly understood. Still, one can hypothesize that the strength of the microfibril and the network overall might be affected by the DP of the cellulose chain (Fujita *et al.* 2011). Shorter chains would be easier to separate and manipulate, which would then make them ideal for walls that are going through expansion such as PCWs. In contrast, longer chains would be less susceptible to slippage and be more rigid, features important for SCWs.

The spatial organization of cellulose microfibrils also differs between PCW and SCWs. In PCWs microfibrils are organized in a network fashion, however, they are generally aligned transverse to the axis of elongation. This is important as this mediates anisotropic growth of the cell as it elongates by providing structural resistance to expansion in the lateral dimension (reviewed in Wasteneys *et al.* 2006). In SCWs, cellulose microfibrils are arranged in a highly organized fashion. This is highlighted in the SCWs of xylem vessels and tracheids of wood, where cellulose is deposited in three distinct layers, S1 to S3 (Kerr and Bailey 1934; Wardrop and Preston 1947; Barnett and Bonham 2004; Abe and Funada 2005). Within each layer the microfibrils have the same longitudinal angle, known as the microfibril angle (MFA) (Wardrop and Harada 1965; Harada and Côté 1985). The first and last layers, S1 and S3, are nearly transverse to the plane of elongation while the thickest layer, S2, is near longitudinal (Wardrop and Preston 1947). Since tensile strength is greatest parallel to the orientation of microfibrils, varying degrees of orientation allows strength to be maintained in multiple directions (Barnett and Bonham

2004). Developmentally, MFA can vary depending on tissue age and environmental stress. For example, juvenile wood in trees have particularly high MFA, which decreases stiffness but increases flexibility, allowing them to bend and compensate for physical stresses such as wind (Barnett and Bonham 2004). As the wood ages, MFA decreases, stiffening the stem providing support for the increased weight (Barnett and Bonham 2004). In line with this, Cave (1968) showed that a reduction of MFA from 40° to 10° increased the overall stiffness of wood fivefold. This highlights the importance cellulose MFAs have on the overall quality of xylem in woody plants.

1.2 Biosynthesis of cellulose

As discussed in the previous section, cellulose plays an important structural and compositional role in the wall, especially in the SCW. Thus, the properties of wood are inherently affected by the properties of the cellulose synthesized. Given this importance, understanding the process of cellulose synthesis has been a major focus of research, and major advances have been made over the past couple of decades. In order to investigate the trafficking and movement of SCW cellulose synthase complexes, it is necessary to understand the composition and organization of these enzyme complexes.

1.2.1 CELLULOSE SYNTHASE (CESA) enzymes

In plants, cellulose is synthesized by enzymes called CELLULOSE SYNTHASES (CESAs) located in the PM (reviewed in McFarlane *et al.* 2014). These enzymes are homologous to, and named after, the BACTERIAL CELLULOSE BIOSYNTHESIS subunit A (BcsA) protein which is the catalytic subunit for cellulose synthesis in bacteria (Saxena *et al.* 1990; Wong *et al.* 1990; Delmer 1999). Each CESA is hypothesized to synthesize a single glucan chain by polymerizing glucose derived from cytosolic UDP-glucose (uridine diphosphate-glucose). This hypothesis is strongly supported by x-ray crystallography studies of the BcsA cellulose synthase complex of the bacteria *Rhodobacter sphaeroides,* demonstrating that when this cellulose synthase was expressed in *E. coli* and solubilized in detergent, it remained associated with one glucan chain (Morgan *et al.* 2013). This work

was significant as it provided strong evidence that each CESA enzyme has the catalytic structure necessary to carry out polymerization (Morgan *et al.* 2013; Omadjela *et al.* 2013). Although the crystal structure of plant CESAs remains to be resolved, computationally predicted structures of a cotton SCW CESA modeled on the bacterial CESA suggest that plant and bacterial CESAs have similar features, further supporting a one-CESA-one-glucan-chain model (Slabaugh *et al.* 2014; Sethaphong *et al.* 2015).

The number of *CESA* genes in the genome varies among plant species, with different sets of CESAs required for cellulose synthesis in PCWs and SCWs (Carroll and Specht 2011). In *Arabidopsis* for example, CESA1, CESA3, and one of CESA2/5/6/9 are required for PCW production, while CESA4, CESA7, and CESA8 are needed for SCW production (Persson *et al.* 2005). Null mutations to either *cesa1* or *cesa3* show lethality to either the embryo or gametophyte due to severe deficiencies in cellulose, indicating that these CESAs are not redundant to each other (Arioli *et al.* 1998; Persson *et al.* 2007). In contrast, null mutants of *CESA6* show reduced elongation of dark-grown hypocotyls as a result of a minor cellulose deficiency, but are still viable (Fagard *et al.* 2000). This is due, in part, to the redundancy to other CESA6-class members (Desprez *et al.* 2007). Interestingly, although *cesa2/cesa6* double mutants did not have a reduction in total cellulose content when compared to *cesa6* null mutants, they did exhibit additive phenotypes such as lateral swelling of root cells, which suggested more randomized orientations of cellulose microfibrils (Persson *et al.* 2007). This is interesting as it suggests functional diversity among the CESA6-class members that may extend into control of cellulose deposition and/or its quality, and not merely its synthesis. Indeed, functional specialization of CESA6-class members has been shown to occur to in certain cell types. For example, in Arabidopsis epidermal seed coat cells, radial walls are strengthened by CESA2 and CESA9, while pockets of pectinaceous mucilage are anchored to the epidermal cells by cellulose chains specifically produced by CESA5 (Mendu *et al.* 2011).

The CESAs involved in SCW synthesis were first identified by their characteristic irregular xylem (*irx*) phenotype in Arabidopsis stem sections (Turner and Somerville 1997), now considered a diagnostic phenotype for SCW disruption of many kinds.

Additionally, plant lines with mutations in *CESA4*^{irx5}, *CESA7*^{irx3}, *and CESA8*^{irx1} had approximately 70% less cellulose than wild-type (WT) plants (Taylor *et al.* 1999, 2000, 2003). However, not all SCW CESA mutants have an irregular xylem phenotype. The missense *fragile fiber* (*fra*) mutants, *cesa7*^{fra5} and *cesa8*^{fra6}, have normal vessels but reduced SCW thickness in fibers and a significant decrease in cellulose content (Zhong *et al.* 2003). Mutations in SCW CESAs can also affect PCW components, as the missense mutant *cesa7*^{mur10} has altered pectin and xyloglucan structures, predicted to be a result of perturbed cell wall integrity signaling (Bosca *et al.* 2006). Expression analyses using either antibodies raised against the class-specific region unique to each SCW CESA, or GFP tagging of CESA7, revealed that all three proteins are present at the same time in developing tracheary xylem and interfascicular fibers (Taylor *et al.* 2003; Gardiner *et al.* 2003) . Together, these results implicate CESA4, CESA7 and CESA8 in SCW production.

1.2.2 CESA complex (CSC) formation and function

Although each CESA is believed to be capable of glucan synthesis independently, *in planta*, cellulose is synthesized at the PM by a multi-protein complex called the cellulose synthase complex (CSC) (Figure 1-1). Freeze fracture/transmission electron microscopy (TEM) or negative staining/TEM of various moss and vascular plant PMs showed hexameric rosette structures approximately 25 nm in diameter on the extracellular face (Mueller and Brown 1980; Giddings *et al.* 1980), with a larger 40 nm globular structure on the cytosolic face (Browling *et al.* 2008). In freeze fracture images of xylem vessels from *Lepidium sativum* roots, rosettes were only seen in domains where SCW is forming (Herth 1985). Antibody labeling against the catalytic domain of CESAs confirmed that the rosettes seen in freeze fracture/TEM in developing cotton fibers did indeed contain CESA proteins (Kimura *et al.* 1999), verifying the interpretation that a rosette corresponds to a single CSC. Historically, it was believed that 36 or more CESAs made up a complete CSC, based on the number of chains that would account for the observed microfibril widths, and the six-fold symmetry of rosettes (McFarlane *et al.* 2014). However, recent work using improved analytical techniques and computational

modeling have shown that CSCs are more likely to be composed of either 18 CESAs (Newman *et al.* 2013; Oehme *et al.* 2015; Vandavasi *et al.* 2015; Nixon *et al.* 2016) or 24 CESAs (Fernandes *et al.* 2011; Thomas *et al.* 2013; Oehme *et al.* 2015). With each CESA weighing about 120 kDa, the emerging model of the CSC is a hexamer of CESA trimers or tetramers together weighing at least 2 MDa, producing 18 to 24 β-(1-4) glucan chains that assemble into a microfibril (Figure 1-1).

Each CSC must also contain a mix of at least three types of CESA proteins. Co-immunoprecipitation (CoIP) experiments demonstrated that when one of the three CESAs is lost, the large CSC complex is no longer detected, the remaining two CESAs no longer interact and they accumulate to lower levels compered to WT, and this was the case in both PCW CESAs (Desprez *et al.* 2007) and SCW CESAs (Taylor *et al.* 2003). Furthermore, quantitative Western blots, and CoIP followed by mass spectrometry quantification, have suggested that the three CESA classes have a stoichiometric ratio of 1:1:1 within a complex (Hill Jr. *et al.* 2014; Gonneau *et al.* 2014). Interestingly, null mutants of SCW *CESAs* are still able to produce some cellulose, albeit with altered crystallinity and lower abundance (Taylor *et al.* 2003). It may be that the other classes of CESA can partially compensate for the absent CESA class. This hypothesis is supported by studies showing partial complementation of a SCW *cesa8* mutant by an ectopically driven PCW CESA1, and of a PCW *cesa3* mutant by SCW CESA7 (Carroll *et al.* 2012). Alternatively, the remaining CESAs may form aberrant CSCs or act as monomers, producing cellulose of lower quality on their own (Arioli *et al.* 1998). Cellulose production and complex formation was observed in isolated membranes from *Physcomitrella patens* protoplasts overexpressing only *PpCESA5* (Cho *et al.* 2015). Furthermore, heterologous expression of a single *Populus trichocarpa* SCW CESA, *Ptt*CESA8, in the yeast *Pichia pastoris,* resulted in the formation of protein complexes and cellulose microfibril production (Purushotham *et al.* 2016). In yeast expressing *Ptt*CESA8 with N-terminus truncations, microfibrils were not formed, although the production of cellulose chains continued (Purushotham *et al.* 2016). As the N-terminus is a region important in CESA-CESA interactions, this indicates that CSC formation is required for aggregation of cellulose into microfibrils.

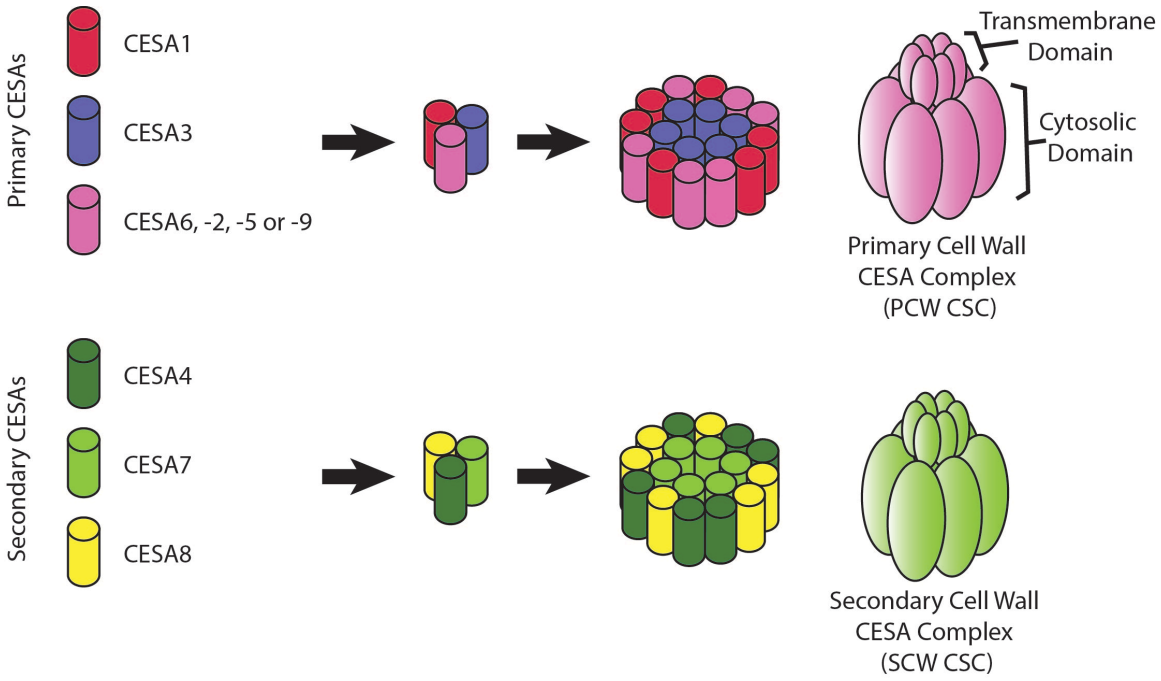

Figure 1-1: Arabidopsis CESA organization in CELLULOSE SYNTHASE COMPLEXES (CSCs)
Arabidopsis has 10 CELLULOSE SYNTHASEs (CESA) of which CESA1,3 and -6-class (-2,-5,-6, or -9) are required for primary cell wall cellulose synthesis. CESA4,7 and -8 are required for secondary cell wall cellulose synthesis. Each CESA can interact with its interacting partners to form homo- and heterodimers and in total, between 18-24 CESAs come together to form a hexameric CESA complex (CSC).

It is not currently understood why multiple CESA isoforms are needed to form a complete CSC or why different CESAs appear to have distinct functions. Genomic analysis of several plant species revealed that the specialization of CESA classes has persisted through much of the evolution of land plants (Carroll and Specht 2011). Primary amino acid sequence comparisons indicate that the hyper-variable and class-specific regions of CESAs are more conserved among orthologs than paralogs, leading to the hypothesis that the conserved amino acids within a class of CESAs reflect functional specialization (Pear *et al.* 1996; Doblin *et al.* 2002). Part of this specialization may be conferred by phosphorylation, as these regions contain several highly conserved phosphorylation sites, which have been shown with site directed mutagenesis and phosphorylation assays to be involved in regulating CESA activity with site directed mutagenesis and phosphorylation assays (Taylor 2007; Chen *et al.* 2010; Sánchez-Rodríguez *et al.* 2017). However, other domains such as the far N-terminus and C-terminus contain sequences that are highly conserved in some CESA classes but lost in others, implying that specificity may extend beyond the previously proposed regions (Carroll and Specht 2011). Recent work creating a comprehensive set of hybrid SCW CESAs, in which several domains from the three SCW CESAs in Arabidopsis were swapped and then tested for complementation of SCW *cesa* mutants, showed that class-specificity was not dependent on either the class-specific or hypervariable domains (Kumar *et al.* 2017). Instead, the suite of CESAs may be required because each CESA isoform has a specific location and fit within the complex (J Wang *et al.* 2006; Kumar *et al.* 2017). Analyses of chimeric PCW CESAs have shown that when the C-terminal half of CESA3 is fused to the N-terminal half of CESA1 and transformed into *cesa1*^{rsw1} mutants, a dominant-negative effect on plant growth was found, implying that the non-functional chimeric protein was occupying the site of the normal functioning CESAs (J Wang *et al.* 2006). The hybrid SCW CESA swapping experiments show that CESA8 is most accepting of other CESA domains, suggesting it may have a peripheral position in the complex, while CESA7 was the least accepting of other CESA domains, implying it may be in a more constrained position (Kumar *et al.* 2017). Still, it is difficult to conclude that

the multiple isoforms exist to play structural roles in a complete CSC until we have a higher resolution view of how each CESA interacts with its partners.

Assembly of CSCs from the CESA monomers is believed to occur in the Golgi apparatus (Haigler and Brown 1986). Although rosettes have been observed in the endoplasmic reticulum (ER) in a single freeze-fracture image (Rudolph 1987), little additional evidence suggests that complex formation begins here. Indeed, other freeze-fracture imaging (Haigler and Brown 1986) and fluorescent microscopy of tagged PCW and SCW CESAs (Paredez *et al.* 2006; Wightman and Turner 2008, 2010a; Crowell *et al.* 2009; Gutierrez *et al.* 2009) have not detected rosettes or significant CESA fluorescent label in pre-Golgi compartments. Further evidence for complex formation in the Golgi comes from analysis of the Golgi-localized STELLO proteins (Zhang *et al.* 2016). STELLOs were shown to interact with PCW and SCW CESAs in the Golgi, and the STELLO double mutant had altered distribution of CESAs in the Golgi, a reduction in PCW and SCW complex formation, decreased PCW CSC delivery to the PM and altered CESA dynamics there (Zhang *et al.* 2016). This highlights the importance of the Golgi in CSC formation, and provides evidence that proper complex formation affects the function of the CESAs at the PM. However, it is still unclear how STELLOs might mediate CESA complex formation in the Golgi and if other proteins are involved.

1.2.3 CSCs at the plasma membrane

The dynamics of cellulose synthesis at the PM is another area of cellulose biology that has been extensively investigated, but due to technical limitations, these experiments were all performed on PCW CESAs. Fluorescently-tagged PCW CESAs in CSCs have been shown to move through the PM (Paredez *et al.* 2006). This movement is thought to be powered by the polymerizing activity of the CSCs pushing against the newly synthesized cellulose microfibril embedded in the wall (Herth 1980; Diotallevi and Mulder 2007; Debolt *et al.* 2007). Imaging of fluorescently-tagged PCW CSCs showed that they move in linear, bi-directional trajectories at speeds of 70 to 500 nm per minute, which has been proposed to correspond to 300 to 1000 glucose molecules per minute (Paredez

et al. 2006). CSC speeds increase at higher temperatures, a property that has been proposed to regulate the growth rate of the cell (Fujita *et al.* 2011). All of these measurements of PCW CESA velocities were measured in the epidermal cells of Arabidopsis hypocotyls using spinning-disk confocal microscopy. However, direct measurements of SCW CESA using the same technique is challenging as the cells that produce SCWs, such as fibers and tracheary xylem, are deep within tissue which causes a sharp decrease in resolution during imaging due to having to image through several layers of cells (Gardiner *et al.* 2003; Wightman and Turner 2008; Wightman *et al.* 2009). Despite this, a number of key observations have been made using the native tracheary elements of Arabidopsis roots and live cell imaging. Gardiner *et al.* (2003) showed that the localization of SCW CESAs to the banded SCW domains in these cells is dependent on the presence of all three SCW CESA partners as with the loss of any one, the remaining CESAs no longer appear in banded patterns. Additionally, similarly to PCW CESAs, SCW CESAs are localized in intracellular compartments such as Golgi, that continually migrate throughout the cell and pause at domains of SCW synthesis, which are hypothesized to correspond to delivery of CSCs to the PM (Wightman and Turner 2008, 2010a).

The localization of CSCs in SCW domains of developing xylem cells has also been found to be dependent on CESA acylation (Kumar *et al.* 2016). Such post-translational modifications have been proposed to increase the hydrophobicity of the CESAs, increasing their association with the PM lipids and ensuring CSCs remain in the PM as the extruded cellulose microfibril pushes the CSC, down, depressing the membrane (Diotallevi and Mulder 2007; Kumar *et al.* 2016). The addition of acyl-groups to the CESAs may facilitate formation of lipid micro-domains that have been hypothesized to be crucial for CSC function (Guerriero *et al.* 2010; Kumar *et al.* 2016), although this has not been experimentally tested. Cells with patterned SCW deposition provide an opportunity to test if the membrane environment around CSCs differs from other types of membranes. The high density of SCW CSCs should enrich any associated membrane features in the SCW domains, which would then be distinct from the other membrane domains that lack CSCs.

Both the speed of CSCs as they move through the lipid environment of the PM, and the lifetime of a CSCs at the PM could influence the cellulose properties of SCWs such as the length of the cellulose chains in the wall, i.e. degree of polymerization (Bashline *et al.* 2014). If lifetime determines degree of cellulose polymerization, then we would expect the pool of SCW CESAs to have a longer half-life, as cellulose chains in SCWs are usually greater than three times longer than in PCWs (McNeil *et al.* 1984; Joshi and Mansfield 2007). Due to the high density of CSCs at the PM, and the difficulty tracking a particle travelling the circumference of the cell, the lifetime of CSCs at the PM has not been directly measured. The lifetime at the PM of PCW CSCs was indirectly estimated to be about 21 minutes, based on freeze fracture of cells from the moss *Funaria hygrometrica* after treatment with monensin, an inhibitor of the Golgi mediated secretion pathway (Rudolph and Schnepf 1988). These values are comparable to the estimated lifetime of 5 to 20 minutes from live-cell imaging of PCW CSC delivery and densities at the PM (Sampathkumar *et al.* 2013; Bashline *et al.* 2013). In Western blot analysis, levels of the cotton (*Gossypium hirsutum*) SCW CESA *Gh*CESA1 rapidly declined after protein synthesis inhibition by cycloheximide, while other membrane proteins persisted for well over four hours (Jacob-Wilk *et al.* 2006). The authors estimated that the SCW CESAs have a half-life of less than 30 minutes. These estimates all support the view of CESAs as actively turning over in both PCW and SCW production, consistent with the large population of intracellular CESAs seen in live cell imaging (Wightman and Turner 2008; Crowell *et al.* 2009; Gutierrez *et al.* 2009). Given the similarity in estimated lifetimes of PCW and SCW CESAs, the large increase in cellulose chain length in SCWs compared to PCWs may instead be dependent on other factors such as the speed of cellulose synthesis, or overall membrane fluidity, however further experimental work is required to test this hypothesis.

1.2.4 Microtubule guidance of CSCs

CSCs closely follow the tracks of cortical microtubules (MTs) lying underneath the PM in both PCW (Paredez *et al.* 2006; Fujita *et al.* 2011) and SCW synthesis (Wightman and Turner 2008, 2010a), supporting the hypothesis that cortical MTs dictate the

orientation of cellulose deposition in cell walls (Ledbetter and Porter 1963). This is highlighted in SCW synthesis, where treatment with the MT depolymerizing drug oryzalin, led to the loss of CSC banding patterns at SCW domains (Gardiner *et al.* 2003; Wightman and Turner 2008). In PCWs this MT guidance has been shown to be dependent on the Cellulose Synthase Interacting (CSI)1/POM2 (Gu *et al.* 2010; Li *et al.* 2012; Bringmann *et al.* 2012; Lei *et al.* 2012) and the closely related CSI3 (Lei *et al.*, 2013). These proteins interact with both PCW CESAs and MTs, and are important for co-alignment of CSCs and MTs (Gu *et al.* 2010; Li *et al.* 2012; Bringmann *et al.* 2012; Lei *et al.* 2013). Recently, CSI1/POM2 was also shown to be enriched in MT pull-downs in Arabidopsis SCW-producing cell cultures (Derbyshire *et al.* 2015). Aberrant SCW formation was then observed in cells where CSI1/POM2 knocked-down using RNAi (Derbyshire *et al.* 2015). Similar patterning defects were recently characterized in native tracheary elements of Arabidopsis and rice (*Oryza sativa*) knock-downs (Schneider *et al.,* 2017). This study also showed that CSI1/POM2 colocalizes and co-migrates with SCW CSCs at the PM. Loss of CSI1/POM2 results in the uncoupling of CSC trajectories from MT tracks during early stages of SCW formation, further supporting a role for these proteins in SCW patterning (Schneider *et al.,* 2017).

Although CSI1/POM2 suggests a mechanism for MT-guidance of CSCs, CSCs may in turn exert force on the underlying cortical MTs leading to cross-talk between CSCs and MT patterning and dynamics. Indeed, disruption of cellulose synthesis during PCW production with CESA inhibitors, or via mutations, has been shown to alter the cortical MT network (Fisher and Cyr 1998; Paredez *et al.* 2008). This is highlighted in mutants of the Cellulose synthase-Microtubule Uncoupling (CMU) proteins, where the force of CSC movement along a linear trajectory was able to displace MTs that they encountered (Liu *et al.* 2016). CMU proteins bind MTs *in vitro*, and are hypothesized to anchor the MTs to the PM (Liu *et al.* 2016). The displacement force exerted by CSCs on the underlying cortical MTs may help explain the observed cross-talk between CSCs and MT patterning and movement. Companion of Cellulose Synthase (CC) has also been shown to link CESAs to MTs, as fluorescently-tagged CC colocalized and moved with CESA particles at the PM

indicating that CC may be a part of CSCs (Endler *et al.* 2015). Loss of these proteins decreased CESA delivery to the PM and CESA velocity during salt-stress (Endler *et al.* 2015). Additionally, loss of CCs severely inhibited MT re-formation, while the presence of CCs promoted MT polymerization (Endler *et al.* 2015). The roles of CCs and CMUs have yet to be explored during SCW synthesis, although they have been identified in cells undergoing SCW formation (Derbyshire *et al.* 2015). Thus, it is reasonable to hypothesize that both sets of proteins play a role in ensuring that CSCs remain within the strict confines of SCW-forming PM domains, similar to CSI1/POM2. This may be especially important in SCW production given the large density of CSCs present in these domains, which may lead to larger forces on the underlying cortical MTs. The loss of these proteins might lead to more diffuse SCW domains as the MTs would no longer restrict CSC movement.

1.2.5 Trafficking of CSCs

The CSC at the PM are the product of the CESA gene product being synthesized at the ER and trafficking through the ER and Golgi apparatus. As previously mentioned, complex assembly is believed to occur at the Golgi apparatus. Membrane protein complex assembly in the Golgi is unusual, as assembly of membrane bound complexes typically occurs in the ER (Wightman and Turner 2010b). Still, live cell imaging of fluorescently tagged CESAs have revealed that CESAs accumulate with the Golgi and are located in the periphery of Golgi cisternae giving a characteristic ring like structure (Paredez *et al.* 2006; Crowell *et al.* 2009; Gutierrez *et al.* 2009) (Figure 1-2). This is consistent with electron microscopy work that shows complete rosettes located at the peripheries of the trans-cisternae of the Golgi (Haigler and Brown 1986). Interestingly, the recently identified Golgi-localized STELLO proteins are necessary for the maintenance of this localization to the periphery of the Golgi (Zhang *et al.* 2016). Though their exact role remains to be resolved, proper complex formation is diminished with the loss of STELLO proteins as shown through blue-native polyacrylamide gel electrophoresis and quantitative western blots using both PCW and SCW CESA specific antibodies (Zhang *et al.* 2016). This data

further supports the theory that CESAs accumulation within the Golgi is important for complex formation.

From the Golgi, CSCs can be secreted to the PM, as Golgi pause close to the location of insertion (Wightman and Turner 2008; Crowell *et al.* 2009; Sampathkumar *et al.* 2013) (Figure 1-2). In addition, CSCs appear to be inserted via Golgi-derived vesicles called Small-CESA containing compartments (SmaCCs) (Gutierrez *et al.* 2009). These SmaCCs partially co-localize with the *trans*-Golgi Network (TGN) marker V-type Proton ATPase subunit A1 (VHA-a1), inferring that they may be derived from the TGN (Crowell *et al.* 2009). However, SmaCCs themselves also represent a diverse population of other compartments as they have also been observed to be involved in endocytosis and recycling (Crowell *et al.* 2009; Gutierrez *et al.* 2009). The endocytic nature of SmaCCs is strongly supported by data showing that CESA internalization under stress coincides with accumulation of a population of SmaCCs tethered to MTs, termed Microtubule Associated Cellulose Synthase Compartments (MASCs) (Crowell *et al.* 2009; Fujimoto *et al.* 2015). Furthermore, PCW CESA signal near the PM colocalizes with clathrin light chains (CLC) before the formation of distinct MASC, implying that CESAs are endocytosed via a clathrin-dependent pathway (Miart *et al.* 2014). Together, these data have led to the hypothesis that SmaCCs are involved in routine recycling of CESAs from the PM to the TGN before re-secretion (Bashline *et al.* 2013). Interestingly, CESA endocytosis does not colocalize with FM 4-64, a standard endocytic marker (Gutierrez *et al.* 2009), which may reflect exclusion of this dye from the lipids around an endocytosing CSC. Despite this apparent contradiction, it is likely that SmaCCs are a mixed population of endocytic and exocytic compartments, because CESAs are known to be rapidly internalized and to have a relatively short life-span at the PM (Jacob-Wilk *et al.* 2006). Indeed it has been shown that there is continuous insertion and removal of CSCs from the PM (Rudolph and Schnepf 1988; Rudolph *et al.* 1989; Wightman and Turner 2008). Thus, it is possible to hypothesize that a putative mechanism for regulating CSC activity is through the accumulation or generation of MASCs/SmaCCs.

The importance of endocytosis in CESA function is further demonstrated by data showing that loss of the clathrin adaptor proteins, μ2/AP2M or TWD-40-2, results in an increase in CESA signal at the PM (Bashline *et al.* 2013; Bashline *et al*. 2015). The loss of both adapter proteins leads to decreases in CSC velocities and deficiencies in cellulose content (Bashline *et al.* 2015). In line with this, sterols deficient mutants, display a severe decrease in cellulose content (Schrick *et al.* 2004). As sterols are known to be important for the internalization of other PM proteins via clathrin mediated endocytosis (Men *et al.* 2008), it is tempting to hypothesize that the observed cellulose decrease in sterol deficient mutants maybe due to hinderance of endocytosis of CESAs. In terms of SCW production, CESA endocytosis was also found to be important during fiber development in rice (Xiong *et al*. 2010). A dynamin-related protein implicated in clathrin-mediated endocytosis, DRP2B, had aberrant SCW structures in fibers when overexpressed or lost (Xiong *et al.* 2010). The function of CESA endocytosis is not currently known, but given the decrease in cellulose quality or quantity in mutants deficient in CESA internalization, endocytosis may be a quality control mechanism ensuring degradation of non-functional CESAs, while functional proteins are integrated into new CSCs for re-secretion (Bashline *et al,* 2013; Bashline *et al*. 2015). The mechanism by which CESAs are targeted for endocytosis has not been elucidated, as it occurs infrequently under normal conditions (Bashline *et al.* 2013), but clues may be provided by studying the transition from PCW to SCW synthesis (Z Li *et al.* 2016a), when PCW CESAs may be internalized in bulk.

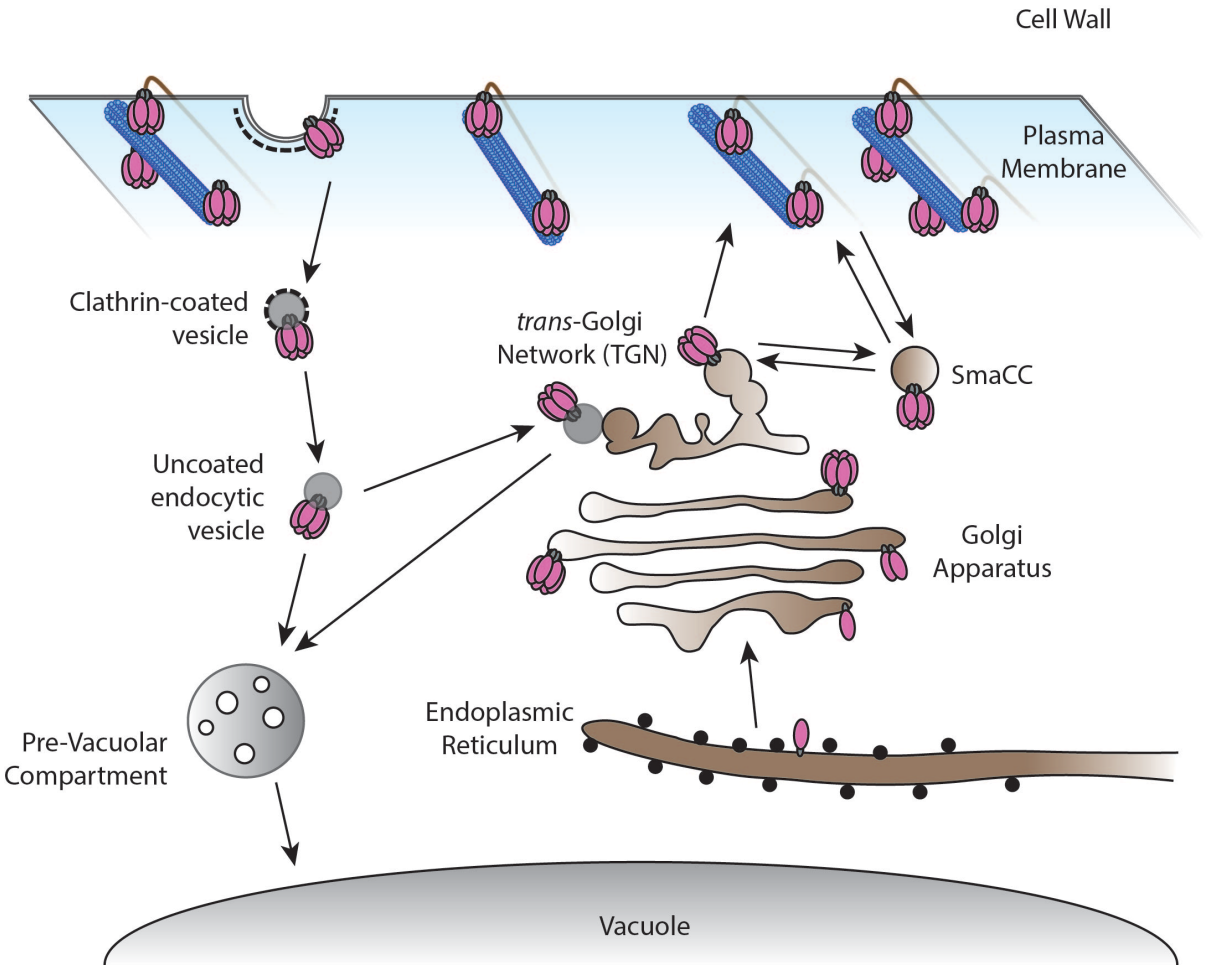

Figure 1-2: Trafficking of CSCs to and from the plasma membrane

CESAs are synthesized at the endoplasmic reticulum (ER) and transported to the Golgi where they are generally found at the peripheries. At the Golgi, CESAs are believed to dimerize/oligomerize with other CESAs and interact with other proteins to form CSCs, which then get processed through to the *trans*-Golgi network (TGN). From there, CSCs can be delivered to the plasma membrane (PM) by small CESA-containing compartments (SmaCCs). At the PM, CSCs move along tracks of cortical microtubules (MTs) as they extrude cellulose microfibirls into the apoplast. CSCs are internalized through either clathrin-mediated endocytosis (CME) or another pathway involving MTs that results a specialized SmaCC called microtubule-associated CESA compartments (MASCs). From there it is believed that they can be recycled back to the PM or targeted to pre-vacuolar compartments (PVCs) for degradation in the lytic vacuole.

1.2.6 Targeting of SmaCCs to secondary cell wall domains

After secretory SmaCCs form at the Golgi, they must next be targeted to their site of exocytosis at the forming SCW. SmaCCs and other secretory vesicles are targeted to cortical MT arrays that line regions of the PM where the SCW is being actively deposited (Oda *et al.* 2015). This is highlighted in Arabidopsis metaxylem cell cultures, where MT patterning was shown to be established and maintained by recruitment of the MT depolymerizing protein kinesin-13A to specific PM regions (Oda and Fukuda 2012b, 2013). This important patterning function of MTs was leveraged to identify and characterize other important players in SCW secretion via a MT pull-down and proteomics analysis in Arabidopsis xylem cell culture (Derbyshire *et al.* 2015). Among the 600+ identified proteins, several of the MT associated proteins, including MAP65 and AIR9, displayed altered SCW patterning when knocked down or overexpressed.

In plant cells, actin microfilaments are responsible for myosin-mediated cytoplasmic streaming of cellular contents, including the Golgi and post-Golgi vesicles (Tominaga and Ito 2015). Live cell imaging in PCW-producing cells showed that SmaCCs travel along endoplasmic actin microfilaments throughout the cell (Sampathkumar *et al.* 2013). Actin disruption by drug treatment or actin mutants resulted in an uneven accumulation of CESAs at the PM near Golgi stacks (Crowell *et al.* 2009; Gutierrez *et al.* 2009; Sampathkumar *et al.* 2013), indicating that while CESAs were successfully delivered to the PM in the absence of actin, their distribution was altered. Actin has also been implicated in proper SCW patterning, as disruption of actin polymerization resulted in aberrant MT banding and SCW patterning in *Zinnia* xylem cell cultures (Kobayashi *et al.* 1988), and loss of CESA banding in native Arabidopsis root tracheary elements (Wightman and Turner 2008). This phenotype may be a result of altered pausing of Golgi in regions close to SCWs, as paused Golgi go on to deliver CSCs to the PM in cells producing both PCWs and SCWs (Wightman and Turner 2008; Crowell *et al.* 2009; Gutierrez *et al.* 2009; Sampathkumar *et al.* 2013; Schneider *et al.* 2017). However, Golgi pausing at SCW domains continued when the MTs lining them were depolymerized, implicating actin in the process of Golgi pausing (Wightman and Turner 2008; Schneider *et al.* 2017).

SmaCCs and other secretory vesicles must also be tethered to their target membranes prior to fusion. Tethering of vesicles to the PM in eukaryotes can be facilitated by the octomeric exocyst complex, which interact with proteins on vesicles and their target membranes (reviewed in Synek *et al.* 2014). Two exocyst components, EXO70A1 and EXO84B, localize to SCW domains, and mutants in *exo70A1* and *exo84b* have aberrant SCW patterning, with an accumulation of large vesicles in developing tracheary elements (Li *et al.* 2013; Vukašinović *et al.* 2017). While CESA banding at SCW domains was disrupted in *exo70A1* and *exo84B* mutants, patterned secretion of laccases did not appear to be affected (Vukašinović *et al.* 2017), suggesting luminal secreted proteins may traffic in different vesicles than the membrane-bound CESAs. In developing xylem, a population of post-Golgi vesicles containing the Vesicle Tethering1 (VETH) and Conserved Oligomeric Golgi (COG) protein complex are associated with the MTs lining SCW domains (Oda *et al.* 2015). Furthermore, fluorescence resonance energy transfer (FRET) microscopy showed that members of the exocyst complex interact with the VETH-COG complex (Vukašinović *et al.* 2017). However, VETH labelled compartments track the plus-ends of MTs, and are therefore not fully compatible with certain populations of SmaCCs/MASCs (Oda *et al.* 2015), which are associated with both plus- and minus-ends (Gutierrez *et al.* 2009), again suggesting the presence of multiple populations of SmaCC vesicles.

Additionally, proper vesicle targeting to the PM is dependent on the composition of phosphatidylinositol phosphate (PIP) lipids on the different organelle membranes (Krishnamoorthy *et al.* 2014; Heilmann and Heilmann 2015). Differentially phosphorylated PIPs have important roles in establishing membrane identity and allowing docking of distinct kinds of proteins. The phosphorylation state of PIPs is regulated by various kinases (PIPKs) and phosphatases (PTases). In Arabidopsis roots, the PIP kinase PIP4K, and other endomembrane machinery, is associated with budding secretory vesicles containing PCW hemicelluloses (Kang *et al.* 2011). The PIP kinase PI3K, which produces PI3P lipids, has been shown to be essential for proper delivery of PCW CESAs to the PM (Fujimoto *et al.* 2015). PI-binding proteins may have a conserved function in SCW-

producing cells, helping to establish the membrane identity of secretory vesicles and their target membranes, allowing for proper budding and tethering of vesicles destined for the SCW. This is supported by a study showing reduced SCW thickness in Arabidopsis fiber cells in a PIP phosphatase mutant (*fra3*) (Zhong *et al.* 2004).

1.2.7 Non-CESA proteins involved in cellulose synthesis

In addition to microtubule-associated proteins, a number of other proteins have been implicated in cellulose production in SCW synthesis (Figure 1-3). One such protein, Sucrose Synthase (SuSy), is an enzyme that catalyzes the cleavage of sucrose in the presence of UDP to form UDP-glucose and fructose (Winter and Huber 2000). SuSy is therefore hypothesized to be the source of UDP-glucose used by the CESA enzymes to produce cellulose (Haigler *et al.* 2001). Through immuno-fluorescence and immuno-TEM, these enzymes have been localized to the PM at sites of cell wall production in developing cotton fibers (Amor *et al.* 1995; Haigler *et al.* 2001) and *Zinnia elegans* tracheary element culture cells (Salnikov *et al.* 2001) similar to CESAs. Additionally, co-immunoprecipitation experiments of *Populus* developing xylem tissue using CESA as bait, have identified SuSys as interacting with CESAs possibly indicating their presence within a functional CSC (Song *et al.* 2010). Overexpression of SuSy in tobacco led to changes in plant growth, but not cellulose levels (Coleman *et al.* 2006), while in poplar, SuSy overexpression produced increased cellulose, with higher crystallinity, without changes to the plant growth (Coleman *et al.* 2009). Thus, it has been hypothesized that SuSy proteins may channel UDP-glucose directly to CESAs within CSCs for cellulose production. However, the importance of SuSy may vary among species, as in *Arabidopsis*, the loss of four of the six SuSy genes (*SuSy1/2/3/4*) results in no obvious defects in plant growth or cellulose content (Barratt *et al.* 2009). This indicates that UDP-Glucose can be sourced via an alternate pathway involving invertases, which hydrolyzes sucrose to fructose and glucose, and UDP-glucose pyrophosphorylase (UGPase) which catalyzes the formation of UDP-Glucose from glucose-1-phosphate (Barratt *et al.* 2009; Park *et al.* 2010). Indeed, the loss of either of these proteins in *Arabidopsis* results in defects in plant growth and decreases

CESA transcript levels (Barratt *et al.* 2009; Park *et al.* 2010). However, cell wall analyses were not performed on these mutants and a more recent study has shown that the quadruple *susy1/2/3/4* mutant still retains a near *wild-type* level of SuSy activity in the vasculature (Baroja-Fernandez *et al.* 2012). Given these conflicting data, and the fact that there is no direct evidence for either SuSy or UPGases physically interacting with CESAs, the exact role of SuSy, invertases and UGPases in cellulose production remains to be resolved.

In addition to SuSy, the functions of the majority of other non-CESA proteins associated with cellulose synthesis remains elusive. One such protein, KORRIGAN (KOR), is a membrane-bound endo-(1,4)-β-glucanase that is a member of the glycosyl hydrolase family 9 (GH9) group of enzymes that has been linked to control of cellulose crystallinity across plant species (Maloney and Mansfield 2010; Maloney *et al.* 2011). In PCWs, loss of KOR or its endoglucanase activity resulted in decreased CSC velocity and defects in MT organization (Paredez *et al.* 2008), ultimately leading to decreases in cellulose content (Lane *et al.* 2001; Sato *et al.* 2001). The importance of KOR in SCW cellulose synthesis is reflected by its identification as one of the first irregular xylem (*irx2*) mutants (Szyjanowicz *et al.* 2004). Recently it has been shown through yeast two-hybrid screens, bimolecular fluorescence complementation (BiFC), and live cell imaging, that in PCWs, KOR directly interacts with CESAs and is a part of CSCs (Vain *et al.* 2014; Mansoori *et al.* 2014). Given its importance, a number of hypothesis about KOR's role in cellulose synthesis have been made including relieving tensional stress generated during cellulose synthesis or release a glucan chain (Somerville 2006). Although GH9s have been well characterized in bacteria and are able to degrade crystalline cellulose *in vitro,* plants GH9s lack a cellulose-binding domain and are unable to hydrolyze crystalline cellulose (Nicol *et al.* 1998). As such the exact substrate and molecular role of plant GH9's, including KOR, remains to be determined. This is a common theme among many of the other proteins linked to cellulose synthesis, especially those associated with SCW cellulose synthesis, including Tracheary Element Differentiation-Related6 (TED6) and TED7, trans-membrane proteins that may be a part of CSCs in SCWs (Endo *et al.* 2009; Rejab *et al.* 2015); COBRA-LIKE4, a

lipid anchored protein with a putative cellulose-binding domain (Li *et al.* 2003; Liu *et al.* 2013); and CHITINASE-LIKE1(CTL1)/POM1 and CTL2, which can bind to glucan polymers, but lacks glucanase activity (Zhang *et al.* 2004; Sanchez-Rodriguez *et al.* 2012). Mutation or loss of any of these genes results in reduced cellulose content and quality within SCWs, making investigation into how each of these gene products contributes to SCW cellulose biosynthesis exciting areas of future study.

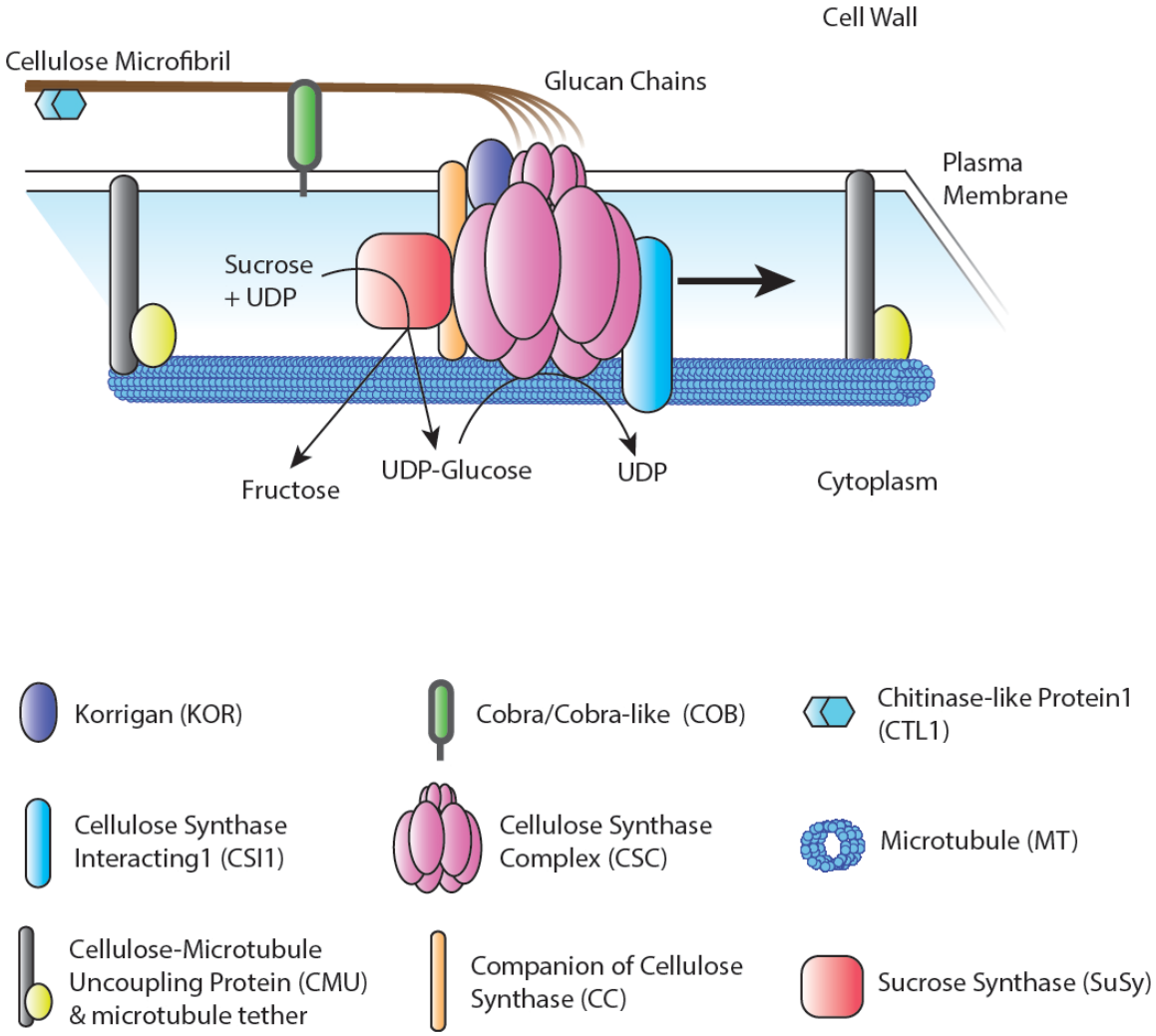

Figure 1-3: Several non-CESA proteins are involved in cellulose production

A simplified representation of proteins that affect cellulose synthesis. The movement of CSCs at the PM is driven by its catalytic activity and the polymerization of glucan chains into cellulose microfibirls. The substrate of CESAs, UDP-Glucose, is in some cases provided by an associated SuSy. As CSC travel along the PM, they are tethered by CSI1 proteins to cortical microtubules that are anchored by CMU proteins. CSCs can also affect MT dynamics through CC proteins. KOR and CTL1 have been shown to bind to cellulose, though their exact functions are yet to be determined. Loss of any of these proteins has been shown to affect cellulose quality and alter CESA velocity and trajectory.

1.3 Tracheary xylem cells as a model for secondary cell wall formation

Over the last decade, live cell imaging of CESAs has immensely improved our understanding of trafficking and activity of CSCs. However, as mentioned earlier, much of this work has focused on PCW CSCs due to the relative ease in imaging them at the plants' surface. Previous work done on SCW CSCs used the developing native tracheary elements of Arabidopsis primary root protoxylem as a model system (Gardiner *et al.* 2003; Wightman and Turner 2008; Wightman *et al.* 2009). This has an advantage over other cell types that produce SCWs as the SCWs are deposited in a relatively short time, in discrete PM domains that result in spiral or annular wall thickenings and be imaged reliably at the elongation zone of a growing root tip (Gardiner *et al.* 2003).

1.3.1 Difficulties of imaging native tracheary elements

Though a number of key observations (that have been discussed in previous sections) have been made by using native tracheary xylem cells in combination with live-cell imaging, it became clear from these efforts that the decrease in resolution caused by having to image through the depth of tissue made it difficult to visualize individual CSCs at the PM in these cells and instead, only faint bands of fluorescence were observed in the area of SCW deposition (Figure 1-4A). These bands of fluorescent CESA7 were also visualized in longitudinal sections of stems in the elongating zone (McDonnell 2010). Thus, the challenges of imaging these cell types deep within tissue has historically limited researchers' abilities to track individual CSCs during SCW synthesis, thus leaving a number of questions about their trafficking and movement through the PM.

For example, one such question is whether SCW CSCs produce cellulose at a faster rate that PCW CSCs? As discussed previously, CSCs move along the PM as they synthesize cellulose and this rate of movement, is often hypothesized to be a proxy for their rate of cellulose synthesis. Given our inability to resolve individual SCW CSCs, previous estimates of SCW CSC movement used an indirect method to measure CSC velocity with Fluorescence Loss in Photobleaching (FLIP) (Wightman *et al.* 2009). Employing this

method, a prolonged bleaching period destroys the fluorescent protein signal from an area adjacent to an area of interest. The loss of fluorescence in the area of interest is then used as a proxy for the movement of particles in the bilayer as they move in into the bleached region of interest (Wightman *et al.* 2009). Using this method, an indirect measurement of velocities of fluorescent-tagged structures was calculated to be in excess of 7 µm per second (Wightman *et al.* 2009). This was the first attempt to measure the speed of SCW CSCs in live cells but these velocities greatly exceed the directly observed velocities of PCW CSCs that have an average of 330 nm per minute. The authors hypothesized that this large increase is due to CSC containing intracellular compartments underneath the SCW masking the signal from the membrane localized CSCs (Wightman *et al.* 2009). Indeed, these intercellular compartments were clearly seen in longitudinal sections of Arabidopsis lines with YFP-CESA7 (McDonnell 2010). Thus, in order to accurately measure CSC velocities, a system where SCW formation occurs in cells on the plant surface is needed to permit the resolution required to visualize individual SCW CSCs with confocal live cell imaging techniques.

1.3.2 The inducible VASCULAR-RELATED NAC-DOMAIN 7 system

A recent development that may alleviate the problem of imaging through the depth of the tissue is the development of transformed plants with an inducible gene expression system that drives ectopic expression of one of the two VASCULAR-RELATED NAC-DOMAIN (VND) transcription factors: VND6 and VND7 (Yamaguchi *et al.* 2010). VND6 and VND7 are master regulators of vessel or tracheary element cell fate and their expression is sufficient to drive differentiation to these elements (Kubo *et al.* 2005). Yamaguchi *et al*. (2010) constructed a chimeric gene system containing either VND6 or VND7 fused to the activation domain of herpes virus VP16 protein and the glucocorticoid receptor (GR) domain under control of the constitutive *Cauliflower Mosaic Virus 35S* (*CaMV35S*) promoter. The presence of the GR domain ensures that in the absence of a glucocorticoid hormone, such as dexamethasone (DEX), the chimeric VND6/VND7 construct remains inactive in the cytosol (Aoyama and Chua 1997). This system permits

for the stable transformation for plants that can be induced to form SCWs ectopically, even in epidermal cells (Yamaguchi *et al.* 2010)(Figure 1-4B). The advent of this system has proved useful already for use in live cell imaging techniques and has been successfully used to study the localization and movement of lignin biosynthesis associated proteins (Schuetz *et al.* 2014) and vesicle fusion machinery (Vukašinović *et al.* 2017) during SCW formation. By crossing these lines with fluorescently tagged CESAs, such as YFP-CESA7, one can potentially visualize and track CSCs as they deposit SCW with high resolution.

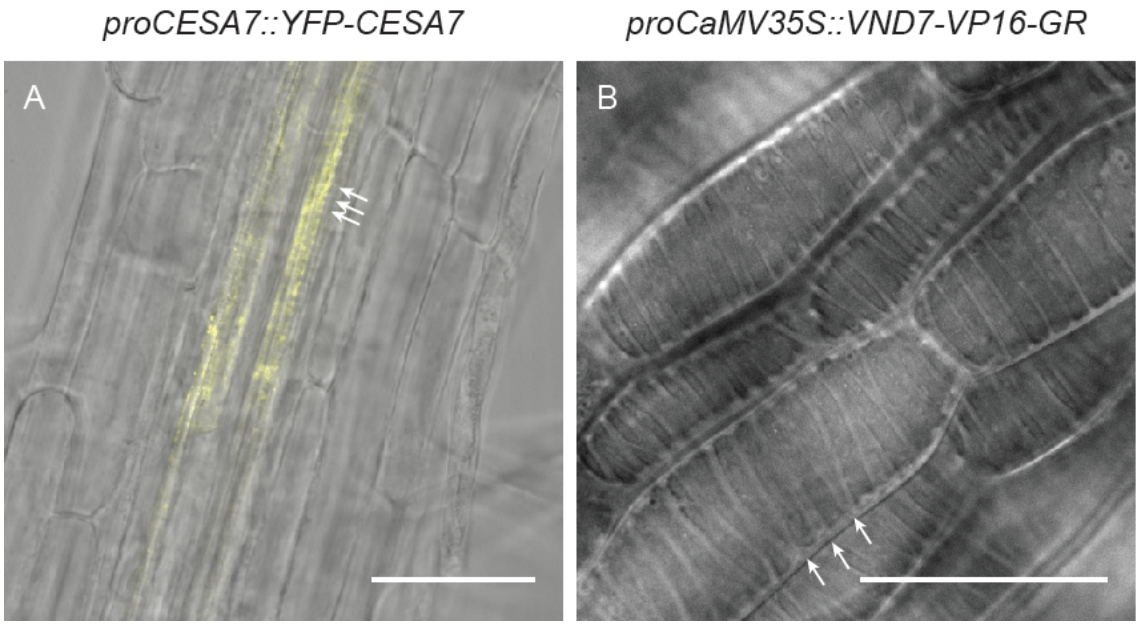

Figure 1-4: The VND7-GR induction system allows us to visualize secondary cell wall synthesis with high resolution

Due to the depth of cells that produce secondary cell walls (SCWs) in plant organs, it has been difficult to study SCW synthesis using live-cell imaging. (**A**) Imaging fluorescently tagged SCW-specific CESA7 in developing root tracheary elements reveals that the depth of these cells limits our abilities to identify any structures, including SCW bands (arrows). (**B**) Conversely, in epidermal cells induced by the VND7-GR system, banded SCWs are clearly seen (arrows) with high detail. Scale bars = 50 µm.

1.4 Research questions, objectives and significance of findings

The broad goal of this study is to directly visualize SCW cellulose deposition in developing tracheary xylem cells to determine the cellular dynamics of CESAs. The specific questions I seek to address are:

1) Do SCW CSCs move along the PM at a faster rate than PCW CSCs?

2) What happens to PCW CESAs during the transition from PCW to SCW synthesis?

3) What happens to SCW structure when one of the CESA is missing and how does loss of the other SCW CSC members (CESA4 and CESA8) influence CESA7 traffic and delivery to the PM?

In order to address these questions, the three main objectives of my research were to:

1) To develop an *in vivo* system in which fluorescently labeled, active SCW CSCs can be tracked individually with high resolution, thus determine the velocity and density of SCW CSCs at the PM during tracheary xylem vessel development.
2) Using the established system from objective 1, characterize both PCW and SCW CSC traffic and dynamics during the developmental transition when SCW synthesis is initiated in xylem tracheary cells.
3) Test the consequences of loss of function of CESA isoforms on the SCW structure and CSC trafficking in VND7:VP16:GR induced cells.

Chapter 2 address the first objective by generating lines of *Arabidopsis thaliana* containing the inducible *proCaMV35S::VND7-VP16-GR* construct and a fluorescently tagged CESA7 driven by its native promoter. Through the generation of these lines, individual SCW CSCs were tracked as they move along the PM. Measurements of SCW CSC velocities and densities were generated and compared to those of PCW CSCs in other lines imaged under the same conditions.

Chapter 3 examines the second objective of my research, namely determining if, when and how PCW CESAs are removed during the transition from PCW to SCW synthesis in developing tracheary xylem vessels. To address this, a natively driven fluorescently tagged PCW CESA, CESA6, was crossed into lines from objective 1, thus allowing for the visualization of both PCW and SCW CSCs during this distinct developmental phase.

Chapter 4 investigates the phenotypic effect of the SCW structure with the loss each of the SCW CESA isoforms. Lines of inducible *proCaMV35S::VND7-VP16-GR* were crossed with knock-out mutants of SCW CESAs and the cell wall architecture was observed with whole-mount immunofluorescence. Additionally, the localization of YFP-CESA7 in these lines was carried out to determine the effect the loss of a SCW CESA isoform had on the trafficking of its partners.

Through this work I have identified and characterized several key features of the cellular dynamics of CESAs during SCW synthesis and highlight several differences to the CESA machinery during PCW synthesis. While the regulatory processes that affect SCW cellulose production remains to be resolved, this work represents an important first step in understanding the cellular dynamics of cellulosic biomass.

Chapter 2: Characterization of Secondary Cell Wall Cellulose Synthesis Using Live Cell Imaging

2.1 Introduction

Cellulose, the most abundant biopolymer on earth, is a key biomechanical component of land plants and a valuable resource. Cellulose in the primary cell wall (PCW), which is laid down during plant growth, determines plant shape (Wasteneys 2004; Doblin *et al.* 2010). However, the bulk of terrestrial biomass is composed of the cellulose in secondary cell walls (SCWs), which are laid down after the cell has stopped growing to strengthen plant vasculature and structure (Joshi and Mansfield 2007). The strength of these walls is derived from the organization of cellulose microfibrils, which compared to PCWs possess cellulose with a higher degree of polymerization, increased microfibril crystallinity, and a higher degree of microfibril organization (Saxena and Brown 2005; Joshi and Mansfield 2007).

Cellulose is synthesized at the plasma membrane (PM) by cellulose synthase (CESA) enzymes that are organized in multiprotein Cellulose Synthase Complexes (CSCs). In *Arabidopsis thaliana*, ten CESAs isoforms exist, with CESA1, CESA3 and CESA6 (and the CESA6-likes) involved in PCW synthesis (Desprez *et al.* 2007; Persson *et al.* 2007), and CESA4, CESA7 and CESA8 required for SCW production (Taylor *et al.* 2003). At least 3 distinct isoforms are required for normal cellulose production (Gardiner *et al.* 2003; Desprez *et al.* 2007; Persson *et al.* 2007). The specialization of each group of CESAs to either primary or SCWs has been conserved through much of the evolutionary history of land plants (Carroll and Specht 2011) and very little redundancy between the isoforms exists (Carroll *et al.* 2012).

Live cell imaging of fluorescently-tagged PCW CESAs has revealed highly dynamic intracellular trafficking and movement of CSCs at the PM in linear trajectories that follow microtubules (MTs) (Paredez *et al.* 2006; Crowell *et al.* 2009; Gutierrez *et al.* 2009). The movement of CSCs along the PM is believed to be propelled by the catalytic activity of the enzyme and the aggregation of the growing cellulose chains into microfibrils (Diotallevi

and Mulder 2007; Debolt *et al.* 2007). As such CSC velocities are often used as a proxy for the rate of cellulose synthesis (Paredez *et al.* 2006; Fujita *et al.* 2011). Unfortunately, such measurements of velocities of SCW CSCs has not been previously possible due to the fact that cells that make SCWs, such as vascular tissue and fibers, are generally deep within plant tissues, limiting the resolution of live-cell imaging (Gardiner *et al.* 2003; Wightman and Turner 2008; Wightman *et al.* 2009). This remains an important question, as the time in which CESAs have to make the extensive layer of SCW cellulose, especially in tracheary elements is relatively limited. Wightman *et al.* (2009) used a fluorescence loss assay to try to measure the velocity, but their values of 7000 nm per second were more consistent with cytoplasmic streaming than CSC velocities. Although the exact timeframe for SCW synthesis in *Arabidopsis* tracheary elements has yet to be determined, the formation of the SCW has been calculated to take 6.4 hours in *Zea mays* and 3.2 hours in *Lepidium sativum* at 21°C (Schneider and Herth 1986). The same study calculated that given the densities of CSC rosettes in SCW regions, measured using freeze-fracture electron microscopy, and the cross sectional area of the SCW thickening of each species' tracheary elements, this process would require CSCs synthesize cellulose chains at a rate of approximately 1000 nm per minute (Schneider and Herth 1986). This is about three times faster than the reported velocities of PCW CSCs measured using confocal imaging at the same temperatures (Fujita *et al.* 2011).

Given, this discrepancy between estimated velocities of SCW CSCs and the measured velocities of PCW CSCs, I sought to develop a system in which SCW CSCs can be observed and tracked individually with live cell imaging. Here I visualize, in live cells, cellulose synthesis in SCWs using fluorescently-tagged CESA7 and, a unique system where epidermal cells are induced to form SCWs ectopically (Yamaguchi *et al.* 2010).

2.2 Results

2.2.1 The inducible VND7 system effectively up-regulates SCW CESAs

VASCULAR NAC-DOMAIN7 (VND7) was identified as master factor controlling tracheary xylem cell fate (Kubo *et al.* 2005). Yamaguchi *et al*. (2010) developed *Arabidopsis* plant lines that constitutively expressed a transcription factor controlling xylem tracheary element cell fate, VASCULAR NAC-DOMAIN7 (VND7), fused to a glucocorticoid receptor (GR). When these plants are exposed to a glucocorticoid hormone such as dexamethasone, all cells are induced to become protoxylem-like tracheary elements (Yamaguchi *et al.* 2010). This system was successfully used to generate a microarray data set of downstream targets of VND7 (Yamaguchi *et al.* 2011). Analysis of this data set shows that, following induction, the SCW cellulose synthase genes were transcriptionally up-regulated 1.5- to 3-fold, while PCW-related cellulose synthase genes' transcription was unaffected or potentially down regulated (Table 2-1). This implied that SCW specific CESAs were potentially being expressed in epidermal cells which have been shown to effectively trans-differentiate in this system (Yamaguchi *et al.* 2010).

Table 2-1: Secondary cell wall related genes and not primary cell wall related genes are upregulated during VND7-GR induction
Microarray data from Yamaguchi *et al*. (2011) for selected cell wall-related genes in either Arabidopsis seedlings constitutively expressing the *VND7-VP16-GR* or *VP16-GR* (vector control) with or without 10 µM dexamethasone induction for 4 h. Seedlings were also treated with 10 µM cycloheximide, a protein synthesis inhibitor, to prevent the production of secondary transcription factors. No significant differences were observed in the expression of cellulose synthesis components or SCW regulators after DEX treatment in the empty vector (control, VP16-GR) control line, as compared to control treatments. Reproduced with permission from Watanabe *et al.* 2015; Copyright American Association for the Advancement of Science © 2015 (DOI:10.1126/science.aac7446).

			proCaMV35S::VND7-VP16-GR						***proCaMV35S::VP16-GR***				
Gene Symbol	**AGI**	**Probe Set ID**	**p**	**FC (abs)**	**[+DEX], normalized**	**[-DEX], normalized**	**Gene Symbol**	**AGI**	**Probe Set ID**	**p**	**FC (abs)**	**[+DEX], normalized**	**[-DEX], normalized**
CESA1	AT4G32410	253428_at	0.86	-1.04	0.05	0.11	CESA1	AT4G32410	253428_at	0.77	1.07	0.15	0.05
CESA3	AT5G05170	250827_at	0.98	-1.01	0.07	0.08	CESA3	AT5G05170	250827_at	0.79	1.06	0.04	-0.05
CESA6	AT5G64740	247251_at	0.91	-1.03	0.12	0.16	CESA6	AT5G64740	247251_at	0.57	1.19	0.08	-0.17
CESA4	**AT5G44030**	**249070_at**	**0**	**2.74**	**0.86**	**-0.6**	CESA4	AT5G44030	249070_at	0.98	1	0.01	0
CESA7	**AT5G17420**	**246425_at**	**0.06**	**1.49**	**0.39**	**-0.18**	CESA7	AT5G17420	246425_at	0.83	-1.02	0.01	0.04
CESA8	**AT4G18780**	**254618_at**	**0.01**	**2.95**	**1.08**	**-0.48**	CESA8	AT4G18780	254618_at	0.27	-1.16	-0.1	0.11
KOR1	AT5G49720	248573_at	0.58	1.11	0.17	0.01	KOR1	AT5G49720	248573_at	0.86	1.03	-0.01	-0.05
KOR2	AT1G65610	264685_at	0.66	1.04	-0.05	-0.11	KOR2	AT1G65610	264685_at	0.61	-1.04	-0.04	0.03
COB	AT5G60920	247552_at	0.83	-1.07	-0.29	-0.18	COB	AT5G60920	247552_at	0.88	-1.05	-0.42	-0.35
COBL1	AT3G02210	259122_at	0.77	1.02	0.04	0.01	COBL1	AT3G02210	259122_at	0.66	-1.03	-0.02	0.03
COBL2	AT3G29810	245228_at	0.48	-1.1	-0.05	0.09	COBL2	AT3G29810	245228_at	0.45	-1.06	-0.04	0.04
COBL4	AT5G15630	246512_at	0	1.54	0.32	-0.3	COBL4	AT5G15630	246512_at	0.51	-1.03	-0.04	0.01
COBL5	AT5G60950	247604_at	0.44	-1.11	0	0.14	COBL5	AT5G60950	247604_at	0.77	-1.04	-0.01	0.05
COBL6	AT1G09790	264710_at	0.47	1.05	0.06	-0.01	COBL6	AT1G09790	264710_at	0.95	-1	-0.03	-0.02
COBL7	AT4G16120	245339_at	0.18	1.1	0.06	-0.08	COBL7	AT4G16120	245339_at	0.68	1.03	0.02	-0.03
COBL8	AT3G16860	256763_at	0.87	-1.03	-0.05	-0.01	COBL8	AT3G16860	256763_at	0.52	1.13	0.25	0.07
COBL9	AT5G49270	248652_at	0.57	1.04	0.05	-0.02	COBL9	AT5G49270	248652_at	0.97	1	0.07	0.06
COBL10	AT3G20580	257082_at	1	-1	-0.01	-0.01	COBL10	AT3G20580	257082_at	0.86	1.01	0.05	0.04
COBL11	AT4G27110	253924_at	0.69	1.03	0.05	0	COBL11	AT4G27110	253924_at	0.45	1.06	0.03	-0.05
KOB1	AT3G08550	258666_at	0.77	1.05	-0.11	-0.17	KOB1	AT3G08550	258666_at	0.93	-1.01	-0.1	-0.08
CSI	AT2G22125	263456_at	0.95	1.02	-0.06	-0.09	CSI	AT2G22125	263456_at	0.65	1.14	-0.07	-0.26

2.2.2 Visualization of individual CSC complexes requires advanced optics

To investigate cellulose deposition, I crossed plants carrying the VDN7-GR with *cesa7*$^{irx3\text{-}4}$ null mutants complemented with a functional fluorescently-tagged CESA7 (YFP-CESA7) driven by its native promoter (Figure 2-1). In induced seedlings, fluorescent signal from both Golgi localized YFP-CESA7 (arrows) and PM localized CSCs was detectable in epidermal cells (Figure 2-2A) representing a significant improvement in resolution over native tracheary elements. However, due to the densities of signal and curvature of the SCW, identification of individual PM-localized CSCs was not possible and could not be resolved even through kymograph analysis (Figure 2-2A). It was only through the use of an optimized spinning disk confocal imaging system, that individual CSC complexes could be resolved and tracked over several minutes (Figure 2-2B).

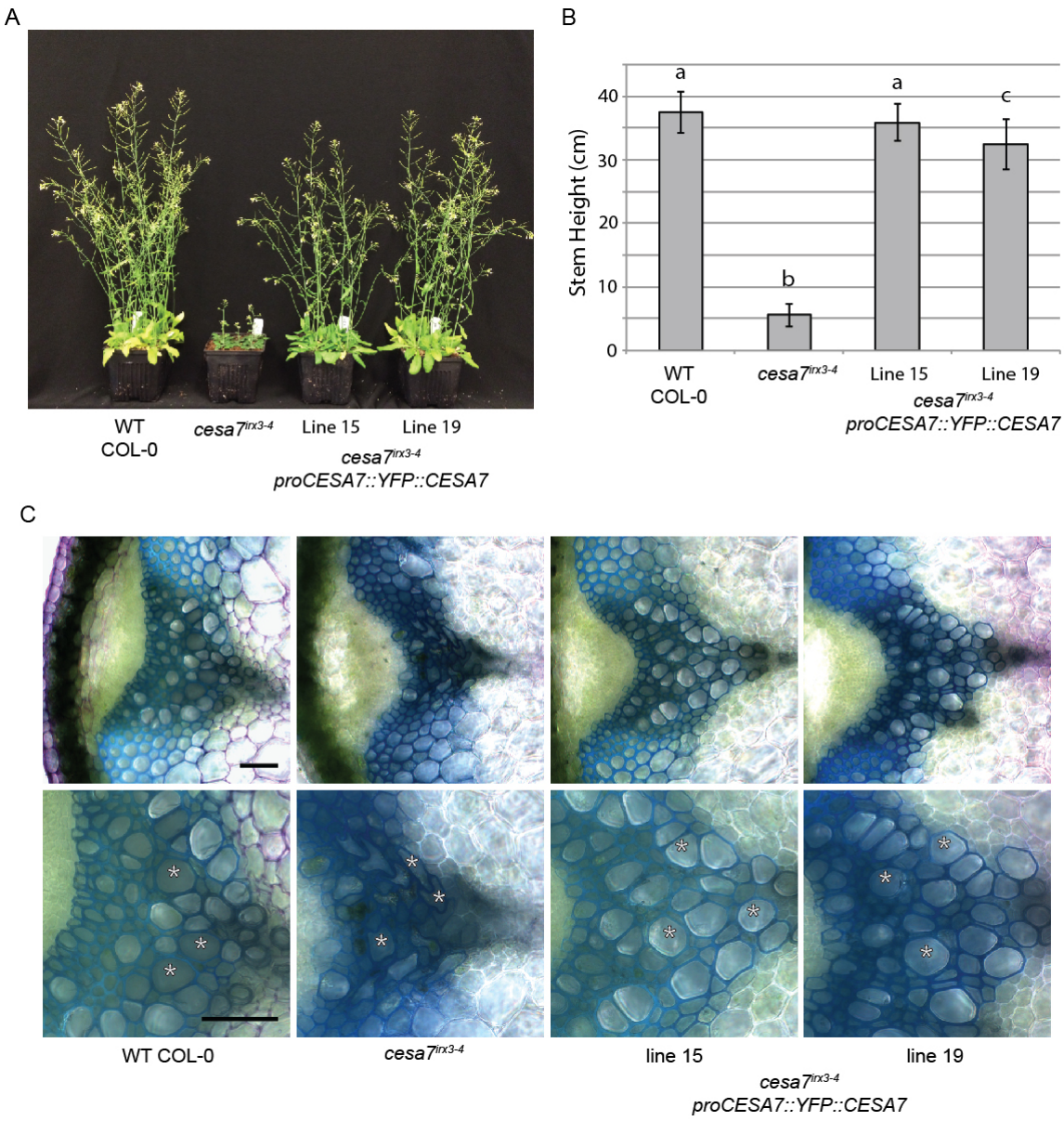

Figure 2-1: The *cesa7*$^{irx3-4}$ mutant phenotype is complemented with the *proCESA7::YFP-CESA7* construct

(**A**) Growth habit of four-week-old Arabidopsis plants contrasting wild-type with *cesa7* mutant allele *irx3-4*, and two independent transformants where CESA7 is expressed under its native promoter in the *cesa7*$^{irx3-4}$ background. (**B**) Stem height of four-week-old Arabidopsis plants of the same genotypes. Means with different letters represent statistically significant differences (Tukey's pairwise comparison, $p<0.01$) among 25 plants for each line, error bars = standard deviation. (**C**) Cross sections of stems from the bottom 1 cm of four-week-old plants stained with 0.01% toluidine blue for 5 min. Bottom panels show higher magnification of xylem tracheary elements (examples labeled with asterisks). Note the collapsed, irregular xylem (*irx*) phenotype of the *cesa7*$^{irx3-4}$ mutant. Scale bars = 50 µm (C). Reproduced with permission from Watanabe *et al.* 2015; Copyright American Association for the Advancement of Science © 2015 (DOI:10.1126/science.aac7446).

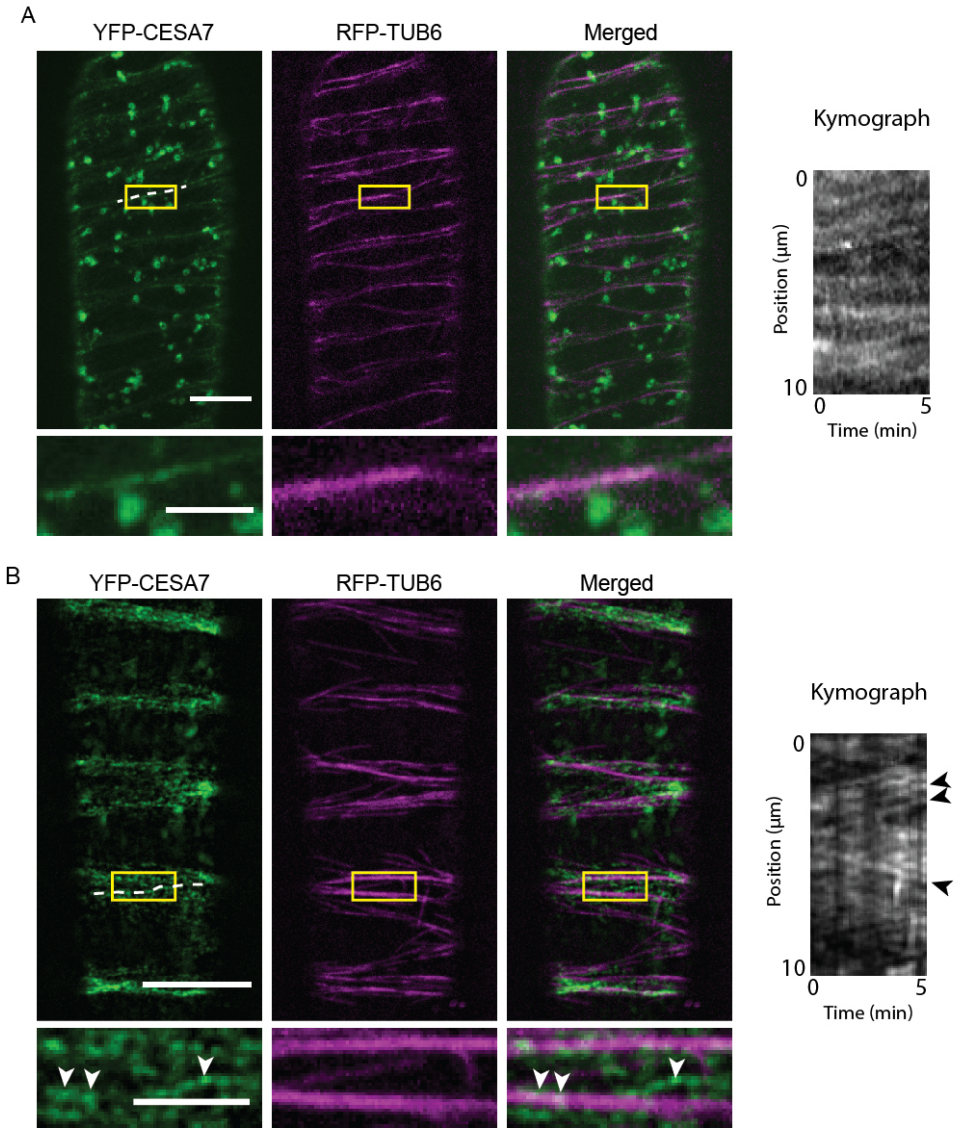

Figure 2-2: Due to the high density of signal and curvature of the developing secondary cell wall, use of an optimized imaging system is required to visualize distinct secondary cell wall CSCs

(**A**) Images of YFP-CESA7 and RFP-TUB6 in VND7-GR-induced cells taken on a non-optimized spinning disk confocal system ("standard spinning disk confocal" described in 2.4.5). Zoom in (inset) reveals that individual complexes are not distinguishable due to the curvature of the plasma membrane around the secondary cell wall and concentration of signal in these domains, as highlighted by kymograph analysis along the dotted line. (**B**) Images of the induced cells taken on an optimized spinning disk confocal system (as described in the materials and methods). Zoom in (inset) reveals that distinct complexes can be observed (arrowheads) and tracked through kymograph analysis (arrowheads point to the same 3 complexes as in inset). Note vertical lines in kymograph in (B) are due to Z-drift. Scale bars: 10 µm, and 3 µm in inset. Reproduced with permission from Watanabe *et al.* 2015; Copyright American Association for the Advancement of Science © 2015 (DOI:10.1126/science.aac7446).

2.2.2 CESA7 is restricted to domains of SCW synthesis

Employing the optimized system permitted the visualization of discrete YFP-CESA7 particles in the PM of induced protoxylem tracheary elements (Figure 2-3). Their linear movement at slow and steady velocities meets the criteria of actively synthesizing CSCs (Movie S1, available online at sciencemag.org) (Paredez *et al.* 2006; Crowell *et al.* 2009; Gutierrez *et al.* 2009; Sampathkumar *et al.* 2013). Individual particles moved in a bidirectional fashion along PM domains underlying SCW thickenings. Compared to labeled PCW CSCs (Paredez *et al.* 2006; Crowell *et al.* 2009; Gutierrez *et al.* 2009), SCW CSC show a higher density at the PM, in domains of SCW synthesis with signals from some individual particles visible, as well as regions where the signals were often overlapping and indistinguishable (Figure 2-4).

In order to determine if SCW CSCs localization followed the underlying cortical MTs, these plants were crossed with lines containing a *proUBQ1::mRFP-TUB6* construct (Ambrose *et al.* 2011) to visualize MT dynamics. Time course analysis of these lines showed that distribution of YFP-CESA7 changed over the course of SCW development and that these changes strongly followed the bundling of underlying cortical MTs (Figure 2-3). Early in development, CESA7 signal was observed across the plane of the PM (Figure 2-3A) on tracks defined by bands of MTs forming in the cell cortex (Figure 2-3A; Table 2-2). As SCW synthesis progressed (Figure 2-3B), CESA7 signal was enriched in regions of the PM associated with tight bundles of MTs (Figure 2-3B, Table 2-2). In late SCW development (Figure 2-3C), the YFP-CESA7 signal was apparent as U-shaped PM furrows, curving around the SCW thickenings. The majority of the CESA7 signal was evenly distributed and restricted to these curved domains (Figure 2-3C, inset). When VND7-GR-induced cells were cryofixed and examined with transmission electron microscopy (TEM), tangential sections along the cell surface revealed the curved domain of PM around SCWs, and their associated MTs in the cell cortex (Figure 2-3D).

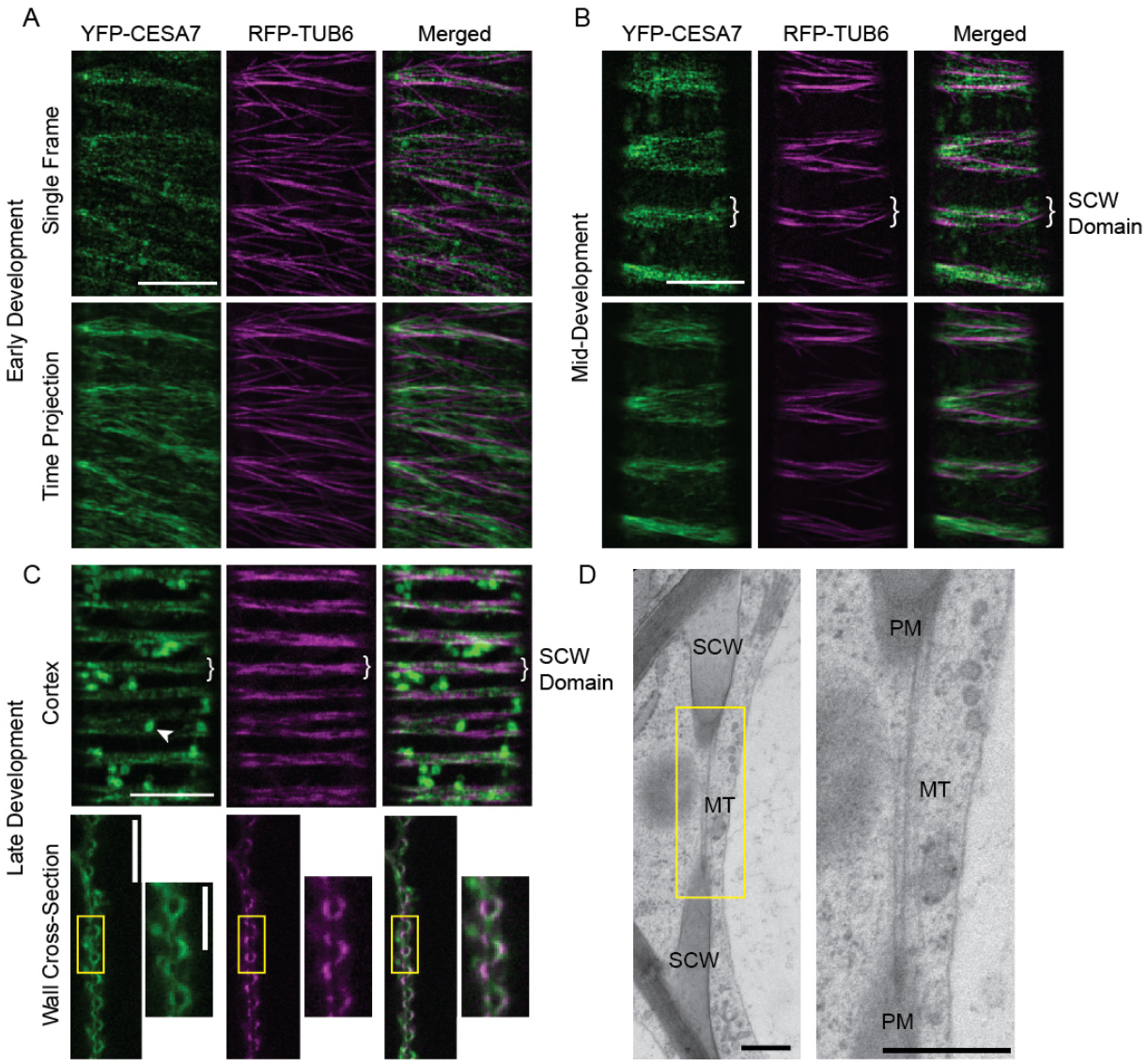

Figure 2-3: CESA7 and microtubules are constrained to secondary cell wall domains during protoxylem development

(**A**) Early development: YFP-CESA7-labeled CSCs and RFP-TUB6-labeled microtubules localize diffusely across the plasma membrane. (**B**) Mid-development: Narrow microtubule bundles lie underneath tight tracks of membrane-localized CSCs. (**C**) Late development: Apparent concentrations of YFP-CESA7 and RFP-TUB6 at the edges of forming secondary cell walls are revealed as uniform signal in subcortical optical sections. YFP-CESA7-labeled Golgi (arrowhead) are visible because of the increased depth of imaging through secondary cell wall thickenings. (**D**) TEM micrographs highlight plasma membrane (PM) curvature over secondary cell walls (SCW), lined by cortical microtubule (MT) bundles. Scale bars = 10 µm in (A to C), and 500nm in (D). Reproduced with permission from Watanabe *et al.* 2015; Copyright American Association for the Advancement of Science © 2015 (DOI:10.1126/science.aac7446).

Table 2-2: CSC area coincident with microtubule domains
Proportion of total area occupied by YFP-CESA7 particles at the plasma membrane coincident with RFP-TUB6 labelled cortical microtubules, and the proportion of microtubule domains coinciding with CESA particles. Values are expressed as means of Mander's colocalization coefficients (Manders *et al.* 1993). (*) indicates means with statistically significant difference (Tukey's pairwise comparison, $p<0.01$). Reproduced with permission from Watanabe *et al.* 2015; Copyright American Association for the Advancement of Science © 2015 (DOI:10.1126/science.aac7446).

Stage of Development	YFP-CESA7 area coincident with MT Domains	MT domains coincident with YFP-CESA7 Area
Early	0.57 ± 0.11*	0.62 ± 0.17*
Mid-	0.79 ± 0.11	0.89 ± 0.08
Late	0.83 ± 0.04	0.88 ± 0.09

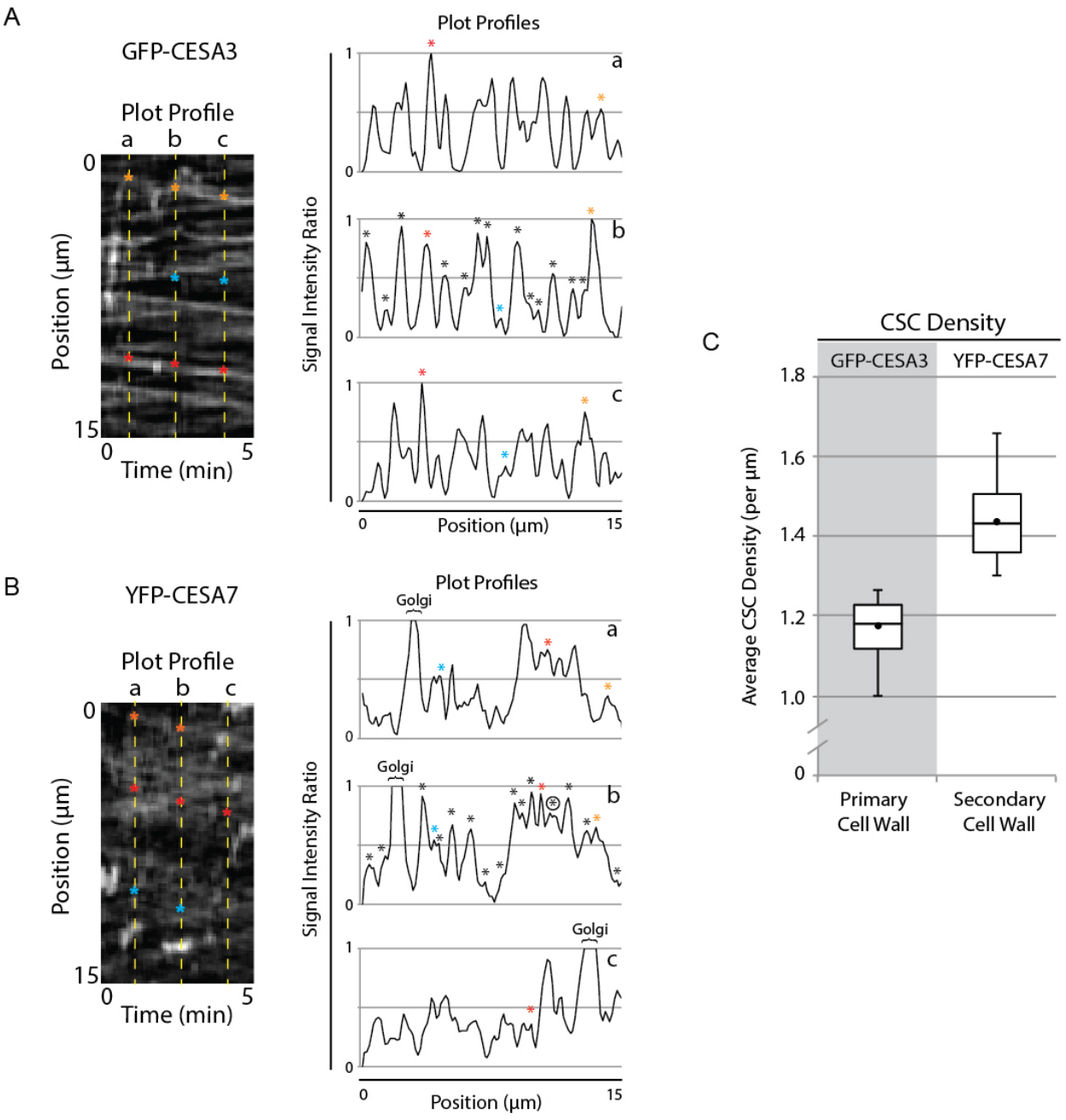

Figure 2-4: Secondary cell wall CSCs have a higher density than primary cell wall CSCs
Densities of plasma membrane localized CSCs were measured by plot profile analysis of kymographs from tracks generated from time lapse movies processed with a strict image processing for background subtraction to minimize intracellular signals. Only peaks associated with linear tracks in the kymograph were counted. This was done by generating 3 plot profiles at the 3 time points. If a peak was visible in at least 2 profiles, and could be followed on the kymograph, it was counted as one CSC (marked with an asterisk in plot profile b). Colored asterisks highlight example peaks as they move through the kymograph. (**A**) Densities of primary cell wall CSCs. (**B**) Densities of secondary cell wall

CSCs were measured as above. However, due to the higher density of signal, in some cases the point spread functions of the complexes overlapped, leading to wide peaks making it difficult to accurately count the CSCs present (circled asterisk). These peaks were only counted as a single CSC. Additionally, signal from intracellular Golgi and SmaCCs often obscured CSC lines, and were not counted in the analysis. (**C**). Box plot of average CSC densities per µm of track (10 tracks averaged per cell, 6 cells per stage). Primary cell wall density was 1.16 ± 0.1 CSCs per µm and SCW density was 1.45 ± 0.13 CSCs per µm. This quantification method is biased towards false negatives, thus this quantification of secondary cell wall CSC density is likely to underestimate true density. However, there is still a significant difference between primary and secondary cell wall CSC densities (*t*-test, $p<0.01$). Reproduced with permission from Watanabe *et al.* 2015; Copyright American Association for the Advancement of Science © 2015 (DOI:10.1126/science.aac7446).

2.2.3 Secondary cell wall CESA Complexes have a higher velocity than primary cell wall CESAs during peak cellulose production

Rate of cell wall deposition is the consequence of both the concentration of CSCs as well as how rapidly each CSC produces cellulose. The significance of the restriction of the CSCs to the curved membrane domains is that cellulose deposition is concentrated in a discrete area of intense production. Such concentration may help to explain why SCWs are synthesized at such a quick rate (Schneider and Herth 1986). With the ability to track individual SCW CSCs with live cell imaging, I sought to measure the CSC velocities of both PCW and SCW CSCs as they move through the PM as a proxy for their rates of glucan chain biosynthesis.

To facilitate this comparison I quantified the velocities of YFP-CESA7 labeled CSCs at the cell membrane and PCW CSCs (GFP:CESA3) (Crowell *et al.* 2009) under identical growth and imaging conditions, and alternating data collection between plant lines in an imaging session to control for possible environmental effects (Figure 2-5). Time projections over a 5-minute data collection period showed CSC tracks across the PM (Figure 2-5, A and B). These tracks defined lines for kymograph analysis of particle velocity (Figure 2-5, A and B). In PCW CSC kymographs, the tracks of each GFP-CESA3 were distinct (Figure 2-5A). The tracks of CESA7 were more difficult to discern due to their higher density (Figure 2-5B; Figure 2-3). The slope of the lines in the kymograph represents the CSC velocities, with steeper slopes indicative of faster CSC movement (more displacement on the spatial axis). The average velocity of CESA7-containing CSCs producing SCWs was 265±75 nm per min (mean ±SD, n = 36 cells [40 CSCs per cell] from 12 plants) (Figure 2-5D). Velocity changed over the protoxylem differentiation, which was divided into stages based on MT banding and SCW features. Average CESA7 velocity in early-development was 293±29 nm per min, while mid-development was 327±37 nm per min, and late development was 187±38 nm per min (Figure 2-5E). In contrast, PCW CESA3-containing CSCs displayed an average velocity of 231±34 nm per min, (n = 12 [4 cells from 4 plants]) (Figure 2-5C). Analysis of variance (ANOVA) identified significant variation among conditions ($F(3,44) = 38.7$, p = 2.133e-12). Post-hoc Tukey's pairwise comparison tests

indicated that PCW CSC velocity was significantly different from all stages of SCW development. SCW CSC velocity did not differ significantly between early- and mid-development, but both were significantly different from late-development ($p < 0.01$) (Figure 2-5E). This illustrates that SCW CSCs move more rapidly in the plane of the membrane during peak SCW synthesis, then slow as the cell nears maturity, prior to programmed cell death (Ohashi-Ito *et al.* 2010). Thus, both the high density and high velocity of synthesis by individual CSC's contribute to rapid cell wall synthesis during SCW formation.

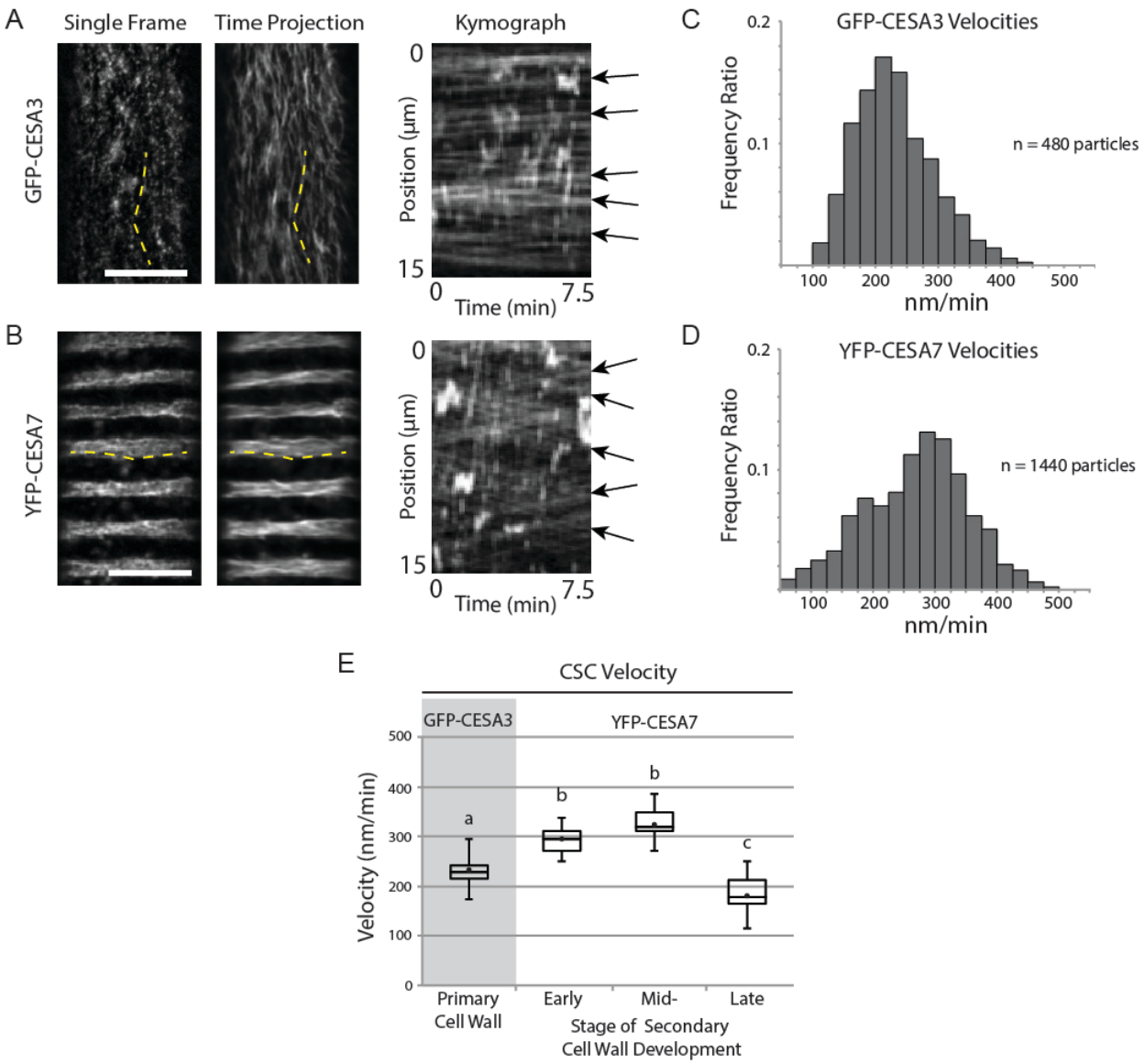

Figure 2-5: Secondary cell wall CSCs have a higher velocity than primary cell wall CSCs during peak cellulose deposition

(**A** and **B**) CSC tracks in single frames and time projections for primary cell wall (A) and secondary cell wall (B) visualized using GFP-CESA3 and YFP-CESA7, respectively. Kymographs sampled along the yellow lines show CSC trajectories over time, from which CSC velocity was calculated. (C and D) Histograms of GFP-CESA3 (**C**) and YFP-CESA7 (**D**) velocities calculated from kymograph analysis. (**E**) Box plot of CSC velocities across stages of xylem cell development. Means with different letters represent statistically significant differences (Tukey's pairwise comparison, $p<0.01$). For each developmental stage, 480 CSC velocities were measured from 12 cells in four plants. In (D), 1440 velocities were pooled from all developmental stages. In (E), velocities were averaged for each cell before analysis. Scale bars = 10 µm in (A and B). Reproduced with permission from Watanabe *et al.* 2015; Copyright American Association for the Advancement of Science © 2015 (DOI:10.1126/science.aac7446).

2.2.4 Secondary cell wall CSCs are trafficked via Golgi and SmaCCs

Previous studies examining fluorescently-tagged SCW CESAs, visualized through layers of tissue to the center of the root, could not resolve CSCs at the PM, although these authors made contributions to understanding the trafficking of CSCs in intracellular endomembranes (Gardiner *et al.* 2003; Wightman and Turner 2008, 2010a). The authors described "CESA7-containing organelles" actively streaming through the cytoplasm and pausing at domains of SCW deposition (Wightman and Turner 2008, 2010a). However, due to technical limitations, the nature of the organelles was not clear.

In the induced xylem tracheary element system of the VND7-GR lines, CESA7-containing organelles were revealed as both small CESA-containing compartments (SmaCCs) (Gutierrez *et al.* 2009) and Golgi (Figure 2-6; Movie S2, available online at sciencemag.org)(Crowell *et al.* 2009). While apparent in all cells observed, SmaCCs were most easily identified using Fluorescence Recovery After Photobleaching (FRAP) (Figure 2-6, A and B; Movie S3 and S4, available online at sciencemag.org). After bleaching the bright PM-localized CSC signal, both SmaCCs and Golgi repopulated the underlying cytoplasm (Figure 2-6A). Golgi and SmaCCs often moved in a coordinated fashion (Movie S3, 40 ± 15% of SmaCCs were associated with Golgi, n = 3 cells), and frequently Golgi and associated SmaCCs would pause (for between 15 sec to 3 min) at SCW domains, which is consistent with previous observations (Wightman and Turner 2008). When the Golgi moved on, a CSC signal would persist and split within 70 ± 20 sec (n = 8 events). (Figure 2-6B, Movie S4, available online at sciencemag.org). This appearance of stationary signal followed by slow steady movement (280 ± 30nm per min, n = 16 particles) fits the criteria for an insertion event of multiple CSCs into the PM as defined for PCW CSCs (Gutierrez *et al.* 2009). I was unable to quantify the number of insertion events at SCW domains due to curvature of the PM around SCWs which made ensuring that the same amount of surface area was being bleached between experiments difficult. However, it was apparent that CSC insertion events were restricted to thickenings (in 12 photobleached regions of 10 μm^2 in 6 cells no CSC inserted in PM regions between thickenings), illustrating the targeting of these events to SCW domains. TEM of induced developing protoxylem cells

revealed several vesicle populations associated with Golgi which may carry CSCs, including trans-Golgi networks, secretory vesicle clusters, and larger vesicles lacking internal content (Figure 2-6C). High-resolution live-cell imaging of CESA7-containing organelles demonstrates the dynamic exchange of CSCs among the Golgi, SmaCCs, and the PM associated with MT bands.

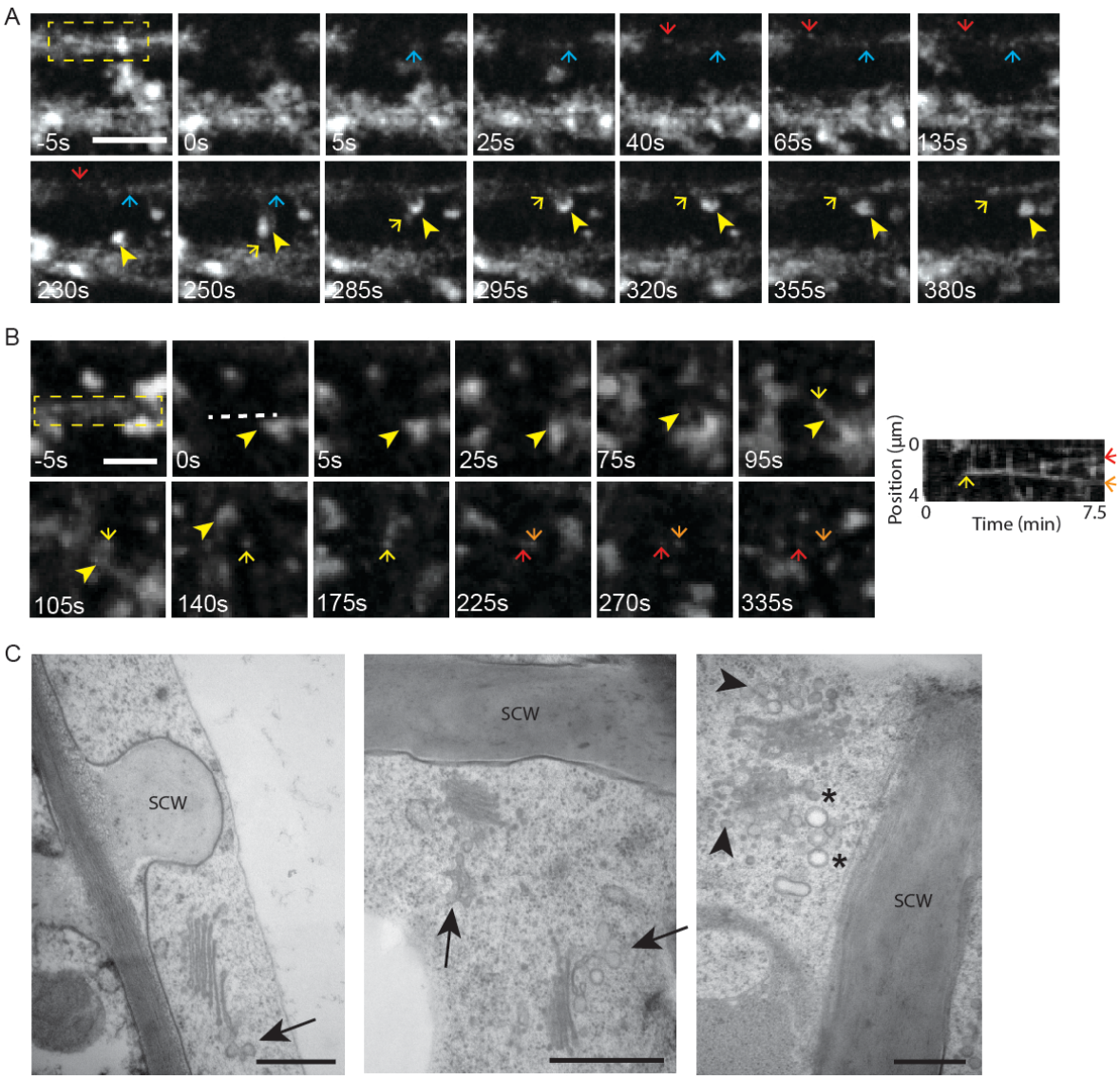

Figure 2-6: Golgi and SmaCCs densely populate and rapidly deliver CSCs to domains of secondary cell wall formation

(**A**) Fluorescence recovery after photobleaching (FRAP) of YFP-CESA7 in the boxed area, overlying a secondary cell wall thickening. Abundant Golgi-independent SmaCCs (red and blue arrows) rapidly repopulate bleached regions. Additionally, Golgi (arrowhead) and closely associated SmaCCs (yellow arrow) can be seen moving from one secondary cell wall band and pausing at another. (**B**) FRAP and kymograph analyses demonstrating insertion at the plasma membrane of at least two YFP-CESA7-labeled CSCs from a SmaCC (yellow arrow). After the Golgi (arrowhead) moves away, the signal from the SmaCC splits into two distinct puncta with steady velocities (red and orange arrows). (**C**) TEM micrographs of cytoplasm around secondary cell walls showing a diversity of closely associated vesicles. Trans-Golgi networks (arrows), secretory vesicle clusters (arrowheads), and electron- lucent vesicles (asterisks) are indicated. Scale bars = 5 µm (A), 2.5 µm (B), 500 nm (C). Reproduced with permission from Watanabe *et al.* 2015; Copyright AAAS © 2015 (DOI:10.1126/science.aac7446).

2.2.5 Loss of microtubules leads to the loss of CESA complex trajectory but not motility or delivery

Previous studies of PCW CSCs showed that disruption of cortical MTs did not affect insertion of CSCs into the PM, although CSC distribution over the membrane was transiently disorganized (Paredez *et al.* 2006; DeBolt *et al.* 2007; Gutierrez *et al.* 2009). To test the effect of loss of MT bundles on SCW CSC insertion events, I measured the velocities, and trajectories of CESA7-labelled CSCs in the VDN7:GR induction system. In contrast to the DMSO control (Figure 2-7A), where the tracks of CSCs were restricted to the SCW bands, the PM localized CSCs in oryzalin treated cells were disorganized (Figure 2-7A; Movie S5, available online at sciencemag.org). These CSC clusters were similar to the "swarms" of PCW CSCs described after treatment with an intermediate (Paredez *et al.* 2006) but not higher (DeBolt *et al.* 2007) concentration of oryzalin. In the absence of MT bands, the velocity of SCW CSCs at the PM was unaffected (313 ± 41 nm per min for control and 324 ± 33 nm per min for oryzalin treated, n = 12 cells from 4 plants for each; Figure 2-7B), while CSC insertion events continued (Figure 2-7C; Movie S6, available online at sciencemag.org). Oryzalin treatment also did not affect the total cellulose content produced by the differentiating cells (Figure 2-8). In contrast, inhibiting cellulose biosynthesis with 2,6-dichlorobenzonitrile (DCB) treatment, only affected deposition of cellulose while MT formation was unaffected (Figure 2-9). Therefore, while MTs are important for the overall SCW banding pattern, they are not necessary for CSC delivery from endomembranes to the PM nor for reaching peak CSC velocity.

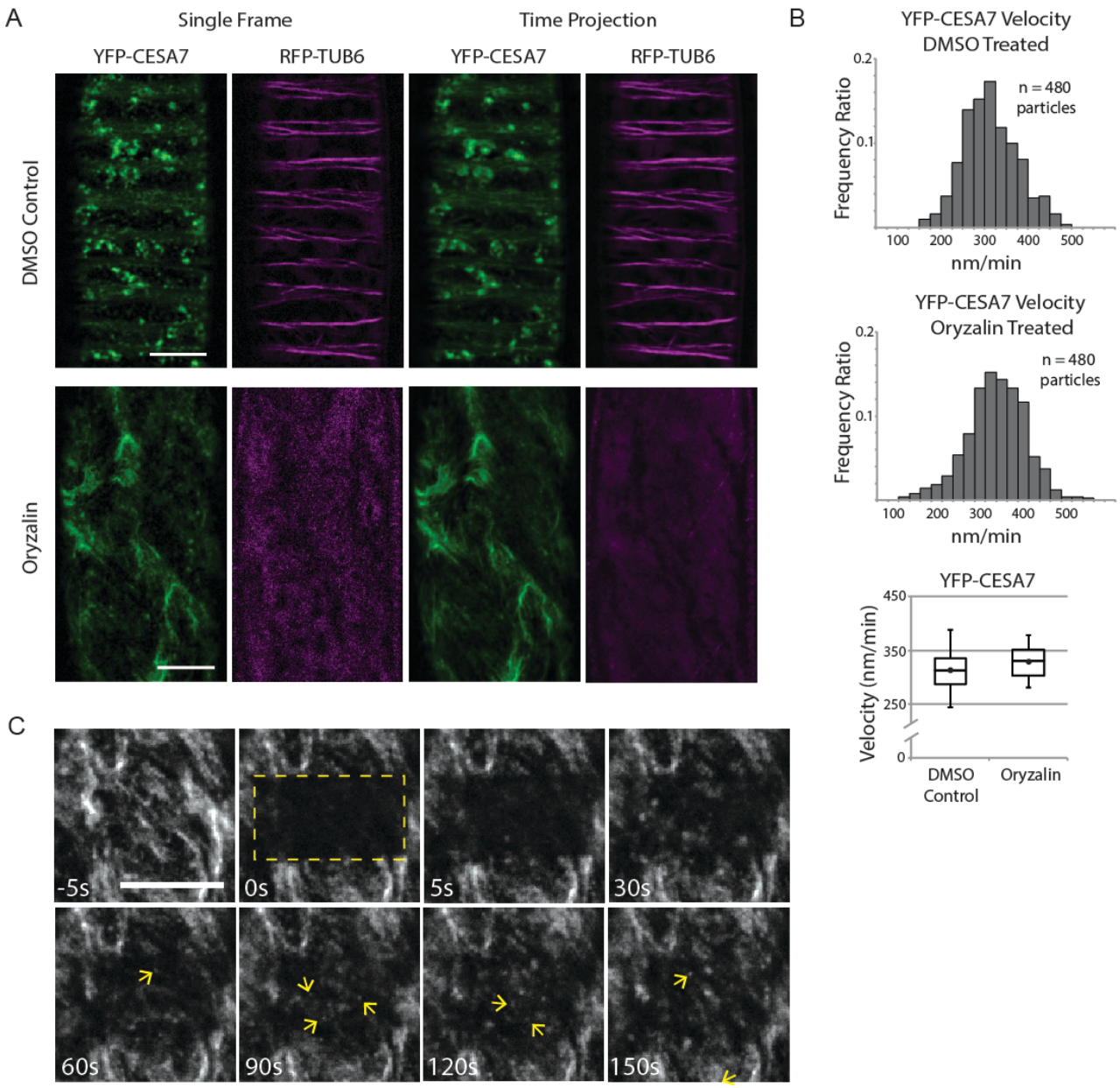

Figure 2-7: Secondary cell wall CSC distribution at the plasma membrane is disorganized by the loss of microtubules after oryzalin treatment while CSC delivery and motility are unaffected

(**A**) VND7-GR-induced cells expressing YFP-CESA7 and RFP-TUB6 after oryzalin treatment. Plasma membrane localized secondary cell wall CSCs follow aberrant tracks in the absence of microtubules. (**B**) CSC velocities were not significantly different between oryzalin- and DMSO-treated cells (Student's t-test, $P = 0.49$). For each condition, 40 CSC velocities were averaged for each of 12 cells in four plants. (**C**) Fluorescence recover after photobleaching (FRAP) of YFP-CESA7 signal revealed insertion of CSCs at the plasma membrane after microtubule loss (arrows). Scale bars = 10 µm (A) and (C). Reproduced with permission from Watanabe *et al.* 2015; Copyright American Association for the Advancement of Science © 2015 (DOI:10.1126/science.aac7446).

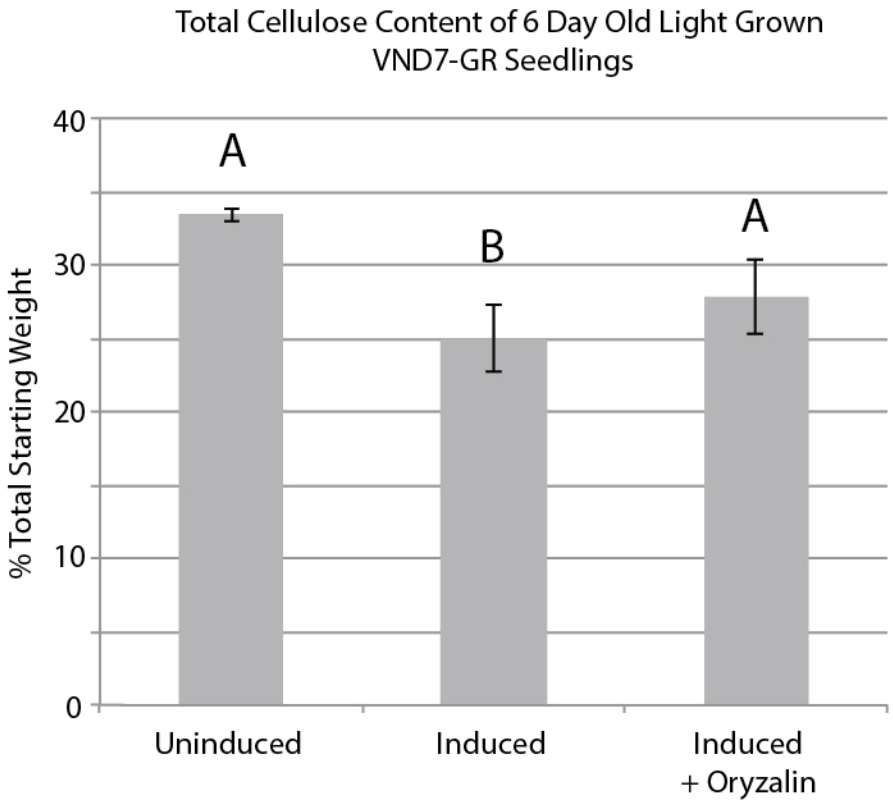

Figure 2-8: Total cellulose content is not affected by depolymerization of microtubules by oryzalin treatment

Average total cellulose content as a percentage of starting dry weight of aerial tissue of 5-day old seedlings (± SD). 5-day old light grown seedlings were treated for 24 h with either: 0.01% Ethanol and 0.2% DMSO (uninduced control) or 10 µM dexamethasone and 0.2% DMSO (induced control) or 10 µM dexamethasone and 20 µM oryzalin (induced oryzalin treated) prior to freeze-drying. Three technical replicates of the pooled samples were processed for each treatment. Means with different letters represent statistically significant differences (Tukey's pairwise comparison, $p<0.01$). Reproduced with permission from Watanabe *et al.* 2015; Copyright American Association for the Advancement of Science © 2015 (DOI:10.1126/science.aac7446).

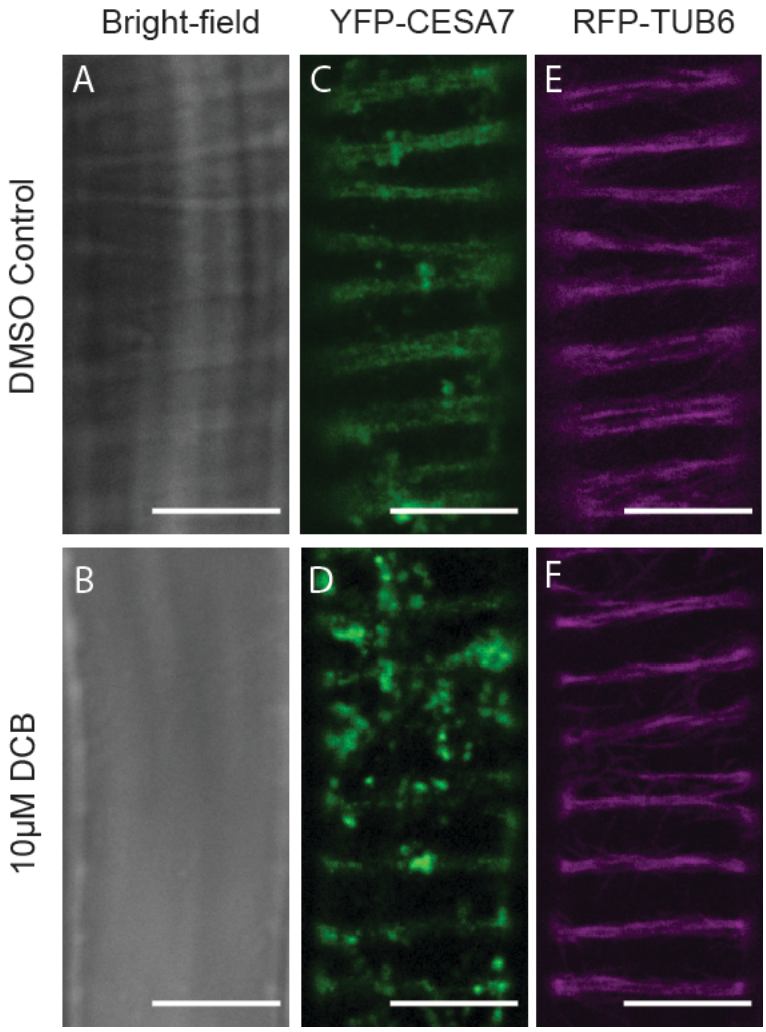

Figure 2-9: Inhibition of cellulose production by 2,6-dichlorobenzonitrile (DCB) does not prevent formation of microtubule bundles or reorganization of YFP-CESA7 signal
Bright-field and single optical sections of YFP-CESA7, RFP-TUB6 in VND7-GR seedlings treated with 10 µM DEX and 0.04%DMSO (DMSO Control) or 10 µM DEX and 10 µM DCB for 16 h. Distinct secondary cell wall thickenings do not form in the presence of the cellulose synthesis inhibitor DCB (**A** and **B**). However, YFP-CESA7 (**C** and **D**) and microtubules (**E** and **F**) still organize into distinct bands in the presence of DCB. Scale bars = 10 µm. Reproduced with permission from Watanabe *et al.* 2015; Copyright American Association for the Advancement of Science © 2015 (DOI:10.1126/science.aac7446).

2.3 Discussion

Though identical at the molecular level, cellulose in the PCWs and SCWs are markedly different in terms of their ultrastructure (Joshi and Mansfield 2007). Insight into the cellular and protein machinery that govern these differences between the two walls has been a challenge, in part to the difficulty of carrying out live-cell imaging of cells that develop SCWs. This study combined two technologies: the VND7-inducible protoxylem tracheary elements with optimized spinning disk confocal imaging to permit direct visualization of CSC in developing SCW, and this combination provides a platform to study the underlying cellular dynamics and regulatory systems that govern cellulose deposition in SCWs. Cellulose in SCW not only provides structural support and strengthens tracheary elements for water conducting functions necessary for plants' existence on land, they also represent the majority of the world biomass. These data provide important insights into how land plants produce SCWs different from PCWs with the ultrastructural features capable of significant upright growth.

2.3.1 Rapid deposition of secondary cell wall is dependent on CESA density and increased velocity

The goal of this chapter was to first develop a system in which individual SCW CSCs can be tracked and their intracellular trafficking be traced with high resolution. My data demonstrate that both increased concentration and velocity of CSCs at the PM may account for the rapid thickening of SCW during xylem cell development. Recently Li *et al.* (2016) validated the inducible VND7 by demonstrating that the cellulose produced is similar to native tracheary elements' cellulose. They also used photobleaching of the CESA7 moving in the bands, concluding that there was 'coherent' movement of the CSC rather than bidirectional movement. In my work, the kymographs reflect areas of the membrane where I could resolve individual CSC for measurement, which theirs did not. In both cases, the SCW CSC were highly concentrated. The density of CSC in these SCW domains, though difficult to quantify with live cell imaging, has been confirmed using freeze fracture electron microscopy (Schneider and Herth 1986). Still, although our

calculated velocities of SCW CSCs were found to be significantly higher than PCW CSCs, their velocities are nowhere close to the estimated values from previous work (Schneider and Herth 1986). Our observed velocities, as well as those of Li *et al.* (2016), fall within the velocities observed in PCW CSCs in other studies (Paredez *et al.* 2006; DeBolt *et al.* 2007; Debolt *et al.* 2007; Fujita *et al.* 2011). Given that SCW velocities are significantly faster, but still within the range of PCW CSC, it is likely that the density of CSCs, rather than their faster velocity, plays the larger role in allowing cellulose to be deposited so quickly in these cell types (Figure 2-10).

The localization of SCW CESAs to intracellular compartments including Golgi and SmaCCs are similar to those observed in PCW CESAs (Crowell *et al.* 2009; Gutierrez *et al.* 2009). However, a striking feature in the VND7-GR system is the pausing of Golgi and SmaCCs specifically at areas of SCW synthesis, that make the Golgi appear to jump from one SCW domain to the next. These pausing events have been observed and quantified in native tracheary elements (Wightman and Turner 2008) and are clearly important for the delivery of CSCs to those domains. This pausing and directed delivery of SmaCCs to the PM are likely caused by interactions with both the actin and MT bundles (Wightman and Turner 2008; Gutierrez *et al.* 2009; Sampathkumar *et al.* 2013). The lack of insertions in the PCW domain that I observed in the inducible system, is consistent with the observation, that CSC insertion events are significantly higher during SCW synthesis than during PCW synthesis (S Li *et al.* 2016). Together, this produces the dense concentration of CSCs to domains of SCW synthesis and depletion in the areas between them. What remains to be seen however, is the role of endocytosis and recycling of CSCs in setting up these concentrated zones. Are CSCs in the areas between SCWs endocytosed? Such events, even for PCW CSCs, are relatively difficult to observe even with the aid of a marker for clathrin mediated endocytosis (CME), such as μ2-YFP (Bashline *et al.* 2013). It remains to be seen though if CESAs only use a certain pathway of CME (Bashline *et al.* 2013) and/or CESAs use another endocytosis pathway (Crowell *et al.* 2009).

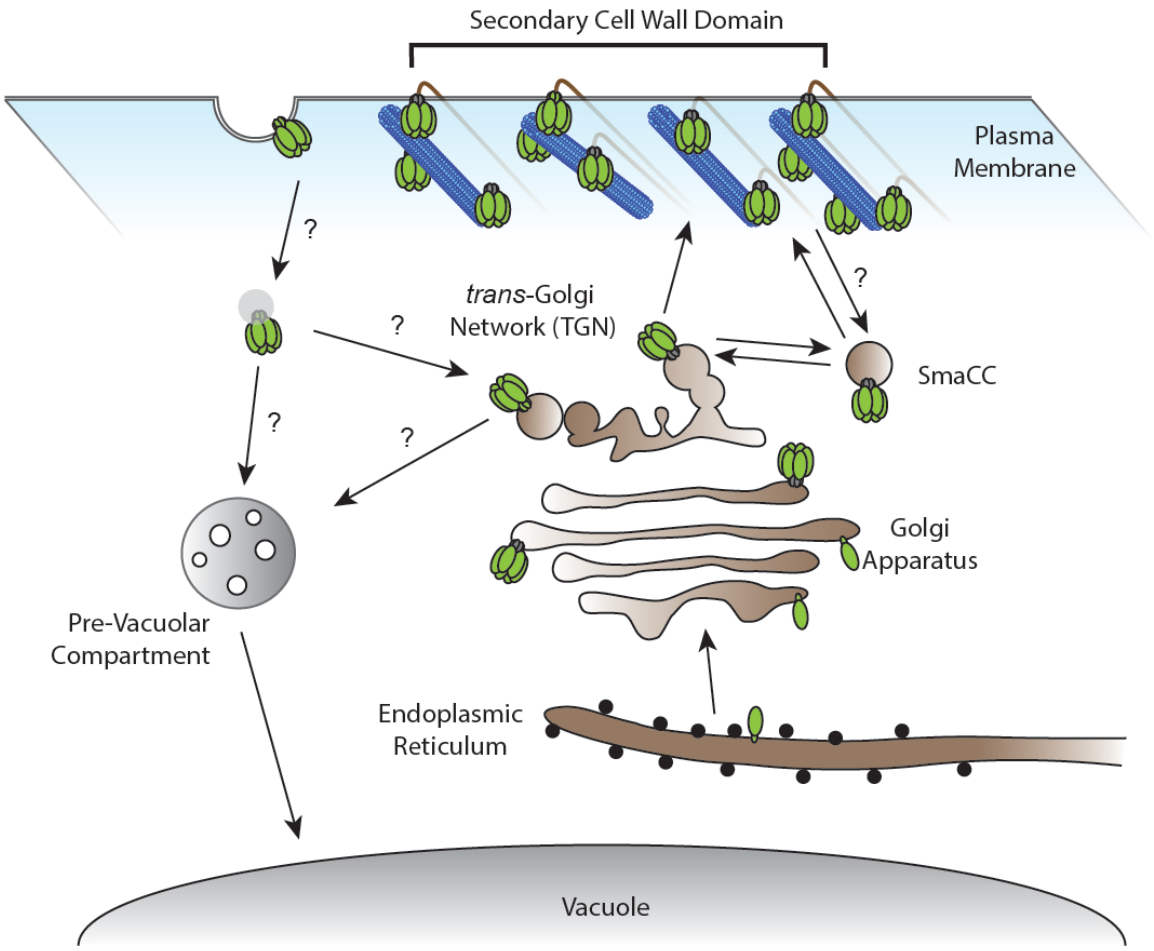

Figure 2-10: CESA complexes are concentrated into secondary cell wall domains
During secondary cell wall (SCW) synthesis, SCW-specific CESA complexes (green) are trafficked via Golgi and small CESA compartments (SmaCCs), to specific domains marked by microtubule bundles (blue tubes). These complexes closely follow tracks of cortical microtubules. This restriction of CESA complexes to these areas results in the concentration of cellulose synthesis to these domains, leading to the banded patterns of SCW seen in protoxylem tracheary elements. Arrows with question marks indicate cellular events that have not been observed in this study but are hypothesized to occur based on previous studies of CESAs.

2.3.2 Cytoskeleton plays an important role in proper CESA delivery and trajectories

The patterning of SCW synthesis is a critical step in the differentiation of xylem tracheary elements. The annular, and spiral structure of SCW in protoxylem tracheary elements allows these vessels to elongate with the surrounding tissue, while still having the necessary strength to resist the negative pressures associated with water transport. This pattern has been shown to be set by the underlying cortical MT bundles (Figure 2-10) (Hepler and Fosket 1971; Gardiner *et al.* 2003; Wightman and Turner 2010a). In analogous metaxylem cells with pits, the MT organization determining cellulose deposition patterns are organized, in part, by a set of Microtubule Associated Proteins (MAPs) that stabilize bundles and ROP-GTPases in the pit regions, initiating MT depolymerization in those regions (Oda and Fukuda 2012a). When I treated the induced cells with the MT depolymerizing drug, oryzalin, CSC delivery to and arrangement at the PM became more disperse and disorganized as expected given the drug's effects on PCW CSCs (Paredez *et al.* 2006; DeBolt *et al.* 2007; Crowell *et al.* 2009; Gutierrez *et al.* 2009). Additionally, similar to PCW CSCs, SCW CSC velocities did not change with the loss of MTs, however the amount of cellulose produce did not decrease. This indicates that delivery rates, and overall number of CSCs at PM are not dependent on MTs.

In summary, by using the inducible VND7-GR system and optimized optics, quantitative live-cell imaging of cellulose deposition in the SCW of living protoxylem tracheary cells was made possible. SCWs thickenings were preceded by a dramatic redistribution and concentration of CESA7-containing CSCs, trafficking compartments and Golgi into narrow membrane domains that were marked by bundling MTs. The velocities of SCW specific CSCs were faster than those of PCW CSCs during the peak of SCW synthesis. The combination of dynamic, intracellular trafficking leading to the concentration of CSCs to narrow domains, and rapid velocity of CSCs explain how the bulk of cellulose is synthesized in SCWs of tracheary xylem cells in a relatively short time.

2.4 Materials and Methods

2.4.1 Construction of the *proCESA7::YFP-CESA7* vector

CESA7 cDNA was amplified and cloned into a pENTR-D/TOPO vector (Life Technologies). Confirmed pENTR-CESA7 plasmids where then used for Gateway-Clonase insertion into *proUBQ10::YFP-DEST* (Grefen *et al.* 2010) to generate *proUBQ10::YFP-CESA7*. The *proUBQ10* of the *proUBQ10::YFP-CESA7* vector was then excised using PmeI and XhoI restriction enzymes. *CESA7* native promoter was then cloned with the addition of matching flanking restriction sites for PmeI and XhoI, and ligated into the PmeI and XhoI digested *proUBQ10::YFP-CESA7* vector to generate the *proCESA7::YFP-CESA7*.

2.4.2 Generation of plant lines

Seeds of *cesa7* (*irx3-4*, SALK_029940C) were obtained from the Arabidopsis Research Center and crossed with lines containing *proCaMV35S::VND7-VP16-GR* (Yamaguchi *et al.* 2010). F2's homozygous seeds for both lines were isolated and were then transformed with either *proCESA7::YFP-CESA7* using the floral dip method (Zhang *et al.* 2006) or crossed with *proUBQ1::mRFP-TUB6* (Ambrose *et al.* 2011). T2s/F2s of these lines were then crossed and F2's genotyped and screened to identify lines homozygous for *cesa7*$^{irx3-4}$ and containing *proCESA7::YFP-CESA7*, *proUBQ1::mRFP-TUB6* and *proCaMV35S::VND7-VP16-GR*. Seeds of *proCESA3::GFP-CESA3* in *cesa3*^{je5} mutant background were a gracious gift from Samantha Vernhettes (Crowell *et al.* 2009). All plants were grown in 18 h of light at 21°C, and 6 of dark at 18°C at 70% humidity.

2.4.3 Seedling growth and induction

Seeds were surface sterilized with 20% bleach and 0.1% Triton (Sigma) for 5 min, and then washed three times with sterilized distilled water. Seeds were sown on plates containing germination media (1× Murashige-Skoog (MS), 1% Sucrose, 1x Gamborg's Vitamin mix, 0.05% MES, 0.8% agar at pH 5.8). Plates were wrapped in aluminum foil and

placed at 4°C for 2 days, before being moved into a growth chamber at 21 °C in a vertical position and grown for 3 days. Plates were then removed from the chamber and under sterile conditions, 10 ml of 10 µM dexamethasone (Sigma) in sterilized distilled deionized water was added on the plates for VND7-GR induction and control treatments (for *proCESA3::GFP-CESA3* in *cesa3*^{je5} seedlings). Plates were then rewrapped in aluminum foil and grown in the dark in a chamber for an additional 12 h (earliest stages of SCW formation) before imaging began. Imaging was carried out between 12 - 24 hours following induction. The timing of induction varied slightly among cells in each seedling, so stage of development was defined based on MT banding and SCW features. At the earliest stages, MTs were dispersed, although bundled MT bands were observed; at mid-development, the MTs outlined the spiral wall thickenings; late in development, the plasma membrane was deformed around the SCW thickening.

2.4.4 Drug treatments

Oryzalin (Sigma) was dissolved in DMSO for a stock concentration of 10 mM and used at a working concentration of 20 µM in 0.2% DMSO. Prior to induction, plates of 3-day-old seedlings were treated with 10 ml of 0.2% DMSO or 20 µM oryzalin for 6 h. Seedlings were then induced by adding 10 µl of dexamethasone stock solution (10 mM) into the media and gently shaking to mix the solution. Seedlings were then returned to the growth chamber under conditions described above. Samples were mounted in 20 µM oryzalin during imaging to ensure the drug was not washed away. DCB treatment 2,6-dichlorobenzonitrile (DCB) (Sigma) was dissolved in DMSO for a stock concentration of 25 mM and used at a working concentration of 10 µM in 0.04% DMSO. Plates of 3-day- old seedlings were treated with 10 ml of 10 µM dexamethasone with either 0.04% DMSO (control) or 10 µM DCB (Sigma) in 0.04% DMSO. Seedlings were then returned to the growth chamber under conditions described above. Samples were mounted in 10 µM DCB during imaging to ensure the drug was not washed away.

2.4.5 Live-cell imaging

Seedlings were mounted between #1.5 45×40 and 24×24 mm coverslips with water and sealed with silicone vacuum grease. Prior to using an optimized spinning disk confocal system as described below, imaging was performed on a standard spinning disk confocal set up (Leica DMI6000 inverted microscope (Leica), Perkin-Elmer UltraView spinning-disk system and a Hamamatsu 9100-02 CCD Camera and a 63X 1.34NA oil lens). YFP was imaged using a 514-nm laser and 540/30 emission filter. RFP was detected with a 561-nm laser and 595/50-nm emission filter. All images were captured using the Volocity 6.3 software package (Perkin Elmer). However, as shown by Figure 2-2, this instrument set up did not provide the necessary detection and resolution to distinguish individual CSCs. The majority of imaging was performed on a Leica DMI6000B inverted microscope equipped with adaptive focus control (Leica), Yokogawa CSU-X1 spinning disc head, Photometrics Evolve 512 Camera, mSAC Spherical Aberration Correction (Intelligent Imaging Innovations) and a 100X 1.4NA oil lens. The combination of a sensitive camera, adaptive focus control, objective lens with a high numerical aperture and spherical aberration correction were essential to visualize CESA7-containing CSC in SCW thickenings. Both GFP and YFP were imaged using a 488 laser, 488/561 dichroic mirror (Semrock) and a 525/50 emission filter (Semrock). RFP was imaged using a 561 laser (Coherent), 488/561 dichroic mirror (Semrock) and a 605/64 emission filter (Semrock). Photobleaching was achieved using Vector FRAP/photo-activation system (Intelligent Imaging Innovations). All images were captured using SlideBook6 software (Intelligent Imaging Innovations).

2.4.6 Image analysis

Images were processed using Fiji software (Schindelin *et al.* 2012). Background correction was performed using the "subtract background" tool with a rolling ball radius of 30 pixels. For images with noticeable x/y drift, a post-acquisition, recursive alignment plugin, StackReg for Fiji (Thévenaz *et al.* 1998), was used to realign images. For images

tracking CSCs at the PM, a post-acquisition frame-averaging plugin (running z- projector plugin, http://valelab.ucsf.edu/~nico/IJplugins/Running_ZProjector.html date accessed: 1 Oct 2014) was employed to average 3 frames to highlight slow moving CSC complexes at the PM. Kymographs were generated using the Multiple Kymograph plugin with a line width of 3 pixels. Movies were generated using MtrackJ plugin for Fiji (Meijering *et al.* 2012).

2.4.7 Correlation analysis

Background correction was performed using the "subtract background" tool in ImageJ with a rolling ball radius of 30 pixels followed by a post-acquisition frame-averaging plugin (running z-projector plugin (http://valelab.ucsf.edu/~nico/IJplugins/Running_ZProjector.html date accessed: 1 Oct 2014). Areas where signal from intracellular compartments were not observable were selected and analyzed using the Coloc2 correlation analysis plugin for Fiji (Schindelin *et al.* 2012) and values calculated as means of Mander's co-localization coefficients as described in (Manders *et al.* 1993).

2.4.8 Image analysis for density measurements

Images were processed using ImageJ software as described above. A more extensive background correction was performed using the "subtract background" tool with a rolling ball radius of 5 pixels. Kymographs were then generated and the plot profile tool was then used to measure CSC density, as described in Figure 2-2.

2.4.9 Transmission electron microscopy

36-h induced seedlings were high-pressure frozen using a Leica HPM 100 in A and B type sample holders (Ted Pella) using 1-hexadecene (Sigma) as a cryo-protectant. Samples were freeze-substituted in 2% osmium tetroxide (Electron Microscope Sciences) and 8% 2,2-dimethoxypropane (Sigma) in acetone for 5 days at -78°C, then slowly warmed to room temperature over 2 days. Samples were then slowly infiltrated with increasing

concentrations of Spurr's resin over 4 days and embedded in polyethylene flat- bottom capsules. Samples were sectioned to approximately 70 nm thickness using a Leica UCT microtome and mounted on 75 mesh copper grids (Ted Pella) coated with 0.3% formvar (Electron Microscope Sciences) and then stained with 2% uranyl acetate in 70% methanol and Reynold's lead citrate. Samples were viewed using a Hitachi H7600 Transmission Electron Microscope equipped with an Advanced Microscopy Techniques CCD camera (Hamamatsu ORCA) at an accelerating voltage of 80kV.

2.4.10 Cellulose quantification

2 grams of surface sterilized seeds were sown on plates containing germination media and placed at 4°C for 2 days. Following, plates were transferred to growth chamber and grown under light for 5 days at 21°C. Seedlings were then treated with 10ml per plate of either: 0.01% Ethanol and 0.2% DMSO (uninduced control) or 10 µM dexamethasone and 0.2% DMSO (induced control) or 10 µM dexamethasone and 20 µM oryzalin (induced oryzalin treated) and placed back in the growth chamber for 24 h. Aerial tissue was then harvested using a razor blade and placed in a 50ml falcon tube and submerged in liquid nitrogen. The samples were freeze-dried and ground on a Mini Mill (Thomas Wiley) to pass through a #40 mesh (0.425 mm). Tissue was then dried for 24 h at 50°C and 15mg of tissue was weighed into each tube. First, the Alcohol Insoluble Residue (AIR) was prepared as described in (Pattathil *et al.* 2012). The AIR was then subjected to a series of extractions in a procedure modified from the AIR fractionation method previously described (Pattathil *et al.* 2012). Specifically, the modification was the removal of the 1M potassium hydroxide extraction, as well as the chlorite extraction and post-chlorite 4M potassium hydroxide extractions. The resulting cellulose residue was then pre-dried in a vacuum centrifuge and finished in a 50°C oven overnight before the final weights were measured.

Table 2-3: Primers employed in this study

Name	Primer Sequence (5' -> 3')	Purpose
irx3-4 At5G17420.P12	TGTTGTAGAAAATTCATATCTTTGTTAGC	Genotyping *cesa7*$^{irx3-4}$ mutants
irx3-4 At5G17420.P13	AGAAAAAGGGTCTGCTGATGA	Genotyping *cesa7*$^{irx3-4}$ mutants
pCESA7.PmeI.FW	GTTTAAACGGCTCCAACGTTTTCAGTTT	Cloning *proCESA7*
pCESA7.XhoI.RV	CTCGAGCGGTGATCAATGAGAGACGA	Cloning *proCESA7*
A7GWFW	CACCGAAGCTAGCGCCGGTCTTGTC	Cloning *CESA7 cDNA*
A7GWRV	TCAGCAGTTGATGCCACACTTGGA	Cloning *CESA7 cDNA*
VND7.At1G71930.P4	TCTTGGATGCTTCCCTGACT	Genotyping *VND7-GR*
GR.Rev	AGCAGGGTCATTTGGTCATC	Genotyping *VND7-GR*

Chapter 3: Cellulose Synthase Complexes Display Distinct Dynamic Behaviors During Xylem Trans-Differentiation

3.1: Introduction

The cellulose network provides protective and structural properties to the cell walls throughout the development of a xylem tracheary element cell. After cell division, the orientation of PCW cellulose microfibrils directs cell expansion by acting as the main load-bearing component that resists the turgor pressure that drives growth (Cosgrove 2005). Once cell expansion ceases, these cells produce thick patterned SCWs that provide the structural strength required by tracheary elements to resist the negative pressures associated with water transport (Schuetz *et al.* 2013). Though both the cellulose in the PCW and SCW are identical in their chemical composition, they differ in terms of ultrastructure including their degree of polymerization and crystallinity (Joshi and Mansfield 2007). However, the underlying processes responsible for these ultrastructural differences are not clear. At the regulatory level, the transition from PCW to SCW production in many species involves the switching of gene expression of PCW-specific *CESAs* to SCW-specific *CESAs*. For example, in *Arabidopsis thaliana*, mutant studies and co-expression data clearly indicate that the PCW production involves the presence of AtCESA1, AtCESA3 and one of the AtCESA6-like (AtCESA2, 5, 6 and 9) (Persson *et al.* 2007), while AtCESA4, AtCESA7, and AtCESA8 are strictly associated with the production of SCWs (Taylor *et al.* 2003). Thus, the transcriptional control of PCW and SCW *CESA* appears to be precisely controlled in plant development, with tight co-expression of primary *CESAs* and secondary *CESAs* (Persson et al., 2007).

Given the functional divergence and expression relationships of the CESAs, one might assume that PCW CSCs are replaced by SCW CSCs during the development of tracheary xylem cells. However, it was also suggested that PCW and SCW CESAs can co-occur in the same CSCs (Carroll *et al.* 2012). Ectopic expression of primary *CESAs* driven by secondary *CESA* promoters in SCW *cesa* mutants also showed that, in most cases, PCW CESAs cannot substitute for a SCW CESA and similarly, most SCW CESAs cannot substitute

for PCW CESAs (Carroll *et al.* 2012). One exception to this was that under the regulation of the *CESA3* promoter, CESA7 partially rescued the weak *cesa3* mutant, *je5*. In addition, CESA1, driven by the *CESA7* promoter, partially rescued the *cesa8* knock out, *irx1-5* (Carroll *et al.* 2012). While these data suggest that CESAs show a limited ability to compensate for each other in loss-of-function mutants, they also indirectly point to an interesting possibility that there may be some coordinated plasticity in the interactions of PCW and SCW CESA proteins. Nevertheless, the principles behind CSC re-modelling during the transition from PCW to SCW synthesis are unknown. Are both PCW and SCW CESAs present together at the PM during SCW synthesis? Or are PCW CSCs removed as SCW synthesis begins? If so, how are they removed? Such changes in the CESA machinery must occur in cells that go through rapid elongation followed by subsequent formation of SCWs, including tracheary elements and fibers.

SCWs are deposited around cells typically situated deep in plant tissues, therefore studies on SCW biosynthesis in general, and the transition from PCW to SCW synthesis specifically, have been limited. This inherent location limits the ability to carry out live-cell imaging with high enough resolution to distinguish individual CSCs and intracellular compartments in these cells (Wightman and Turner 2010). As shown in the previous chapter, this limit can be overcome with the use of the VND7-GR inducible system (Yamaguchi *et al.* 2010) which allows us to observe SCW biosynthesis as it occurs ectopically in epidermal cells. This system thus also provides an opportunity to observe the transition from PCW to SCW biosynthesis with high resolution. Previously, micro-array data of VND7-GR induced samples has shown that PCW *CESA* genes are downregulated following induction, while expression of SCW *CESA* genes increased (Yamaguchi *et al.* 2011; Z Li *et al.* 2016b). However, how the cell coordinates the PCW and SCW CESA proteins at the PM during the xylem vessel development remains to be resolved. Using the VND7-GR inducible system in combination with fluorescently tagged PCW and SCW *At*CESAs (CESA6 and CESA7 respectively), I tracked and characterized the shift in intracellular localization of PCW and SCWs CESAs at the developmental boundary between PCW and SCW production in developing protoxylem tracheary elements (TEs).

3.2 Results

3.2.1 Primary cell wall CESAs are internalized during xylem vessel development

To elucidate how plant cells transition from making primary to SCWs, we crossed VND7-inducible Arabidopsis plants with plants expressing fluorescently tagged PCW CESAs, *ProCESA6::tdTomato-CESA6* (Sampathkumar *et al.* 2013) and tubulin, YFP-TUA5 (Kirik *et al.* 2012). Four-day-old etiolated seedlings of the progeny were induced with dexamethasone in DMSO (Yamaguchi *et al.* 2010). In non-induced DMSO controls, the tdTomato-CESA6 migrated along linear trajectories that were evenly dispersed across the PM, and clearly visible in cytosolic compartments such as Golgi and SmaCCs (Figure 3-1A, 3-2A). Following induction, early transition from PCWs to SCWs was defined by the re-organization of cortical MTs into diffuse bands that mark areas where the onset of SCW synthesis will occur (Watanabe *et al.* 2015; Schneider *et al.* 2017). The tdTomato-CESA6 trajectories followed the MT re-organization and maintained a speed of approximately 199 ± 40 nm/min (*n* = 334 CSCs in 11 cells) during the transition (Figure 3-1B to D). Indeed, kymographs of the tdTomato-CESA6 signal showed smooth continuous lines characteristic of catalytically active PM-localized complexes in both pre-induction and early transition stages (Figure 3-1C). During the subsequent transition phase, referred here to as mid-transition (Figure 3-1B), kymograph analysis showed that the steadily moving PM-located tdTomato-CESA6 signal became less prevalent and the CESAs were instead increasingly observed to move erratically (Figure 3-1C) and were less well coordinated with the MT bands (Figure 3-1B to D). This movement was highly reminiscent of that reported for the SmaCCs/MASCs (Crowell *et al.* 2009; Gutierrez *et al.* 2009). The erratically moving tdTomato-CESA6 foci were also observed during the late transition stage but were more difficult to discern due to the high uniform background signal that most likely emanated from the vacuole (Figure 3-1B to D).

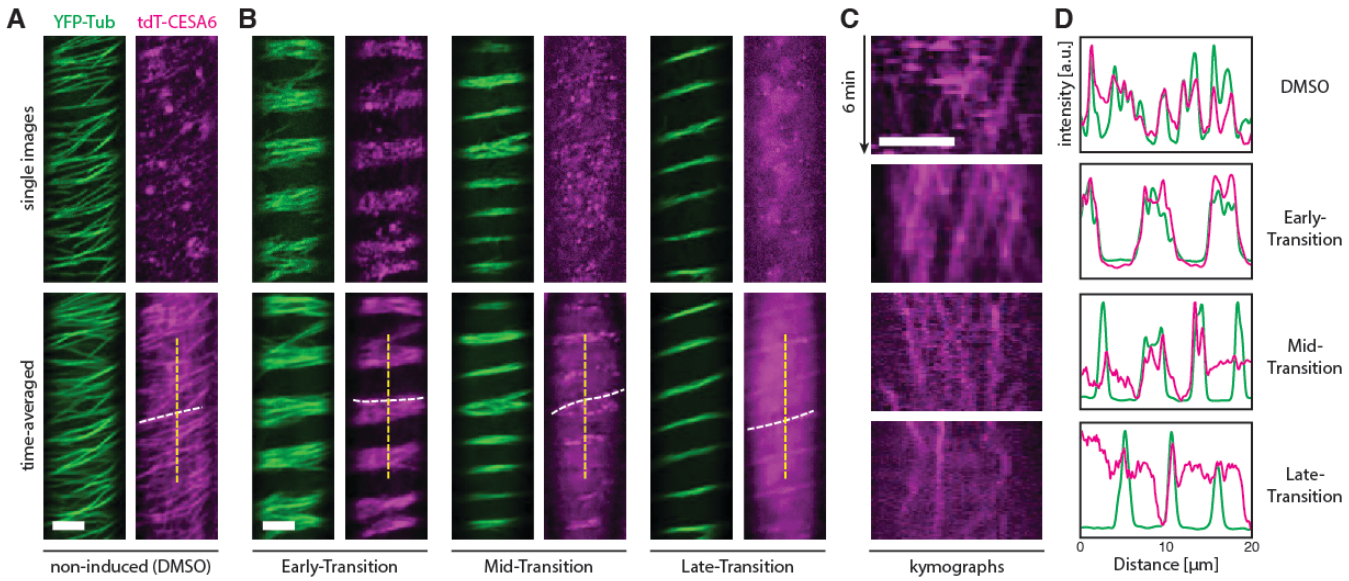

Figure 3-1: Plasma membrane-localized primary CESAs transiently co-occur with forming microtubule bands, and are subsequently depleted, during SCW formation

Five-day-old etiolated hypocotyl epidermal cells expressing YFP-TUA5 (YFP-TUB; green) and tdTomato-CESA6 (tdT-CESA6; magenta) in the VND7-inducible background. Single (top) and time-averaged (bottom) images of the fluorescent signals. (**A**) Non-induced seedlings show transverse MTs aligned with migrating tdT-CESA6 at the plasma membrane. (**B**) The MTs of induced seedlings undergo re-orientation into diffuse bands, which causes similar tdT-CESA6 re-organization. During mid-transition, some tdT-CESA6 signal is maintained in the plasma membrane, but bright round intracellular foci was also prominent. The late-transition stage revealed no tdT-CESA6 signal at the plasma membrane, but instead abundant and diffuse intracellular signal. (**C**) Kymographs along dotted lines in (A) and (B). In non-induced and early-transition (top two kymographs), arrowheads indicate stable movement of catalytically active tdT-CESA6 in the plasma membrane; in mid- and late-transition (bottom two kymographs), empty arrowheads erratically moving intracellular compartments. (**D**) Fluorescence intensity plots of tdT-CESA6 (pink) and YFP-Tub (green). Scale bar = 5 µm.

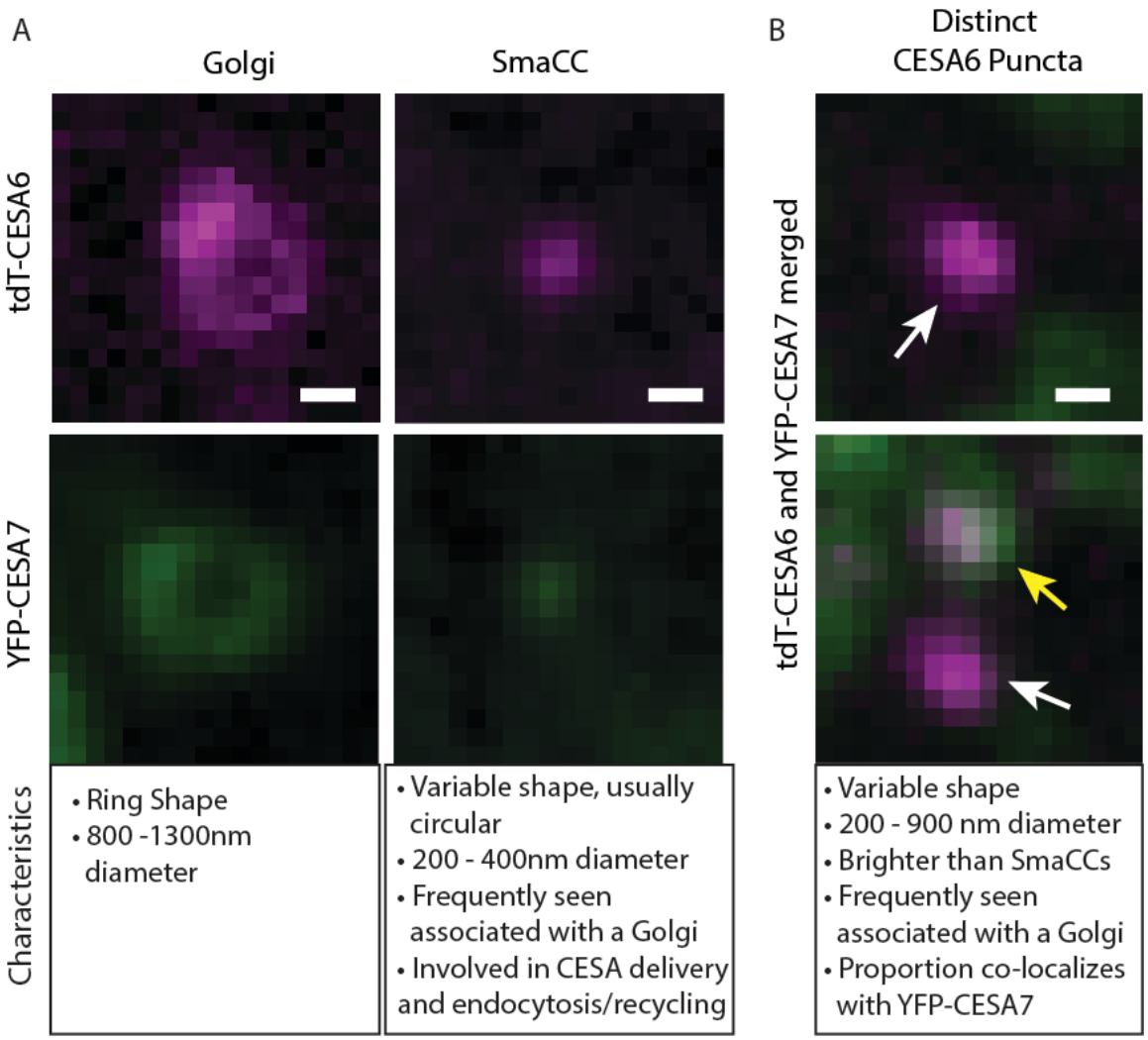

Figure 3-2: Characterization of different intracellular compartments containing CESA during PCW to SCW transition

(A) Both tdTomato-CESA6 and YFP-CESA7 are observed in Golgi and SmaCCs at early stages of transition. Golgi localized CESAs show a characteristic ring-like structure while SmaCCs, which might be involved in both the delivery to the plasma membrane and endocytosis/recycling of CESAs, are generally smaller than Golgi. (**B**) In early mid-late stages, tdT-CESA6 is only seen in puncta that are larger than the previously described SmaCCs. These tdT-CESA6 puncta can be separate from (white arrows) or co-localize with YFP-CESA7 SmaCCs (yellow arrows). Scale bar = 500 nm.

3.2.2 PCW and SCW CESAs briefly co-occur, but have different catalytic rates, at the plasma membrane during xylem vessel trans-differentiation

To simultaneously visualize PCW and SCW CESAs during the transition, I generated Arabidopsis plants expressing the *ProCESA6::tdTomato-CESA6* and a fluorescently-tagged AtCESA7 (*ProCESA7::YFP-CESA7*) in the VND7-GR inducible system. Before VND7 induction, we did not observe any YFP-CESA7 signal in the cells, whereas clear tdTomato-CESA6 signal was detected as described above (Figure 3-3; pre-transition). During the early phase of transition, clear YFP-CESA7 signal appeared in intracellular compartments in close proximity to the PM, in ring-shaped Golgi bodies, and in small CESA-containing compartments (SmaCCs) (Figure 3-3, arrowheads). As the transition progressed, motile YFP-CESA7 appeared at the PM and tracked along trajectories similar to those of tdTomato-CESA6 (Figure 3-3A, 3-4A). However, this developmental window, showing PM localization of both tdTomato-CESA6 and YFP-CESA7, was relatively short-lived and was maintained for a maximum of one hour, suggesting that the PCW CSCs stopped being delivered to the PM. We corroborated this hypothesis through photobleaching experiments in which we found that the recovery of the tdTomato-CESA6 fluorescence was substantially delayed compared to the recovery of the YFP-CESA7 fluorescence (Figure 3-3B to D, arrowheads). Kymograph analysis along these bands revealed the steady movement of YFP-CESA7 foci appearing in bleached areas, which indicates the delivery of active YFP-CESA7 containing CSCs to the PM (Figure 3-3C, arrows). The tdTomato-CESA6 signal was subsequently removed from the PM, and was only observed within bright intracellular puncta (Figure 3-3A, arrows). The transition phase was considered complete when only YFP-CESA7, but no tdTomato-CESA6, fluorescence was evident as distinct foci at, or in close proximity to, the PM (Figure 3-3A).

The co-occurrence of both PCW and SCW CESAs in the same cell permitted detailed analyses of their relative behaviors (Figure 3-4A). Kymograph analyses indicated that the tdTomato-CESA6 and YFP-CESA7 moved with different speeds (Figure 3-4B and C). Indeed, while the tdTomato-CESA6 moved with a speed of 251 ± 19 nm/min (*n* = 128 CSC in 4 cells from three seedlings) the YFP-CESA7 moved significantly faster (Figure 3D;

430 ± 62 nm/min; *n* = 682 CSCs in 10 cells from three seedlings). Combined, these data show that the PCW and SCW CESAs only co-occur at the PM for a few minutes and that the two CSCs move with different speeds. Hence, we conclude that the tdTomato-CESA6 move independently of the YFP-CESA7 (Fig 3-4C and D) despite that the two CESAs track along common paths.

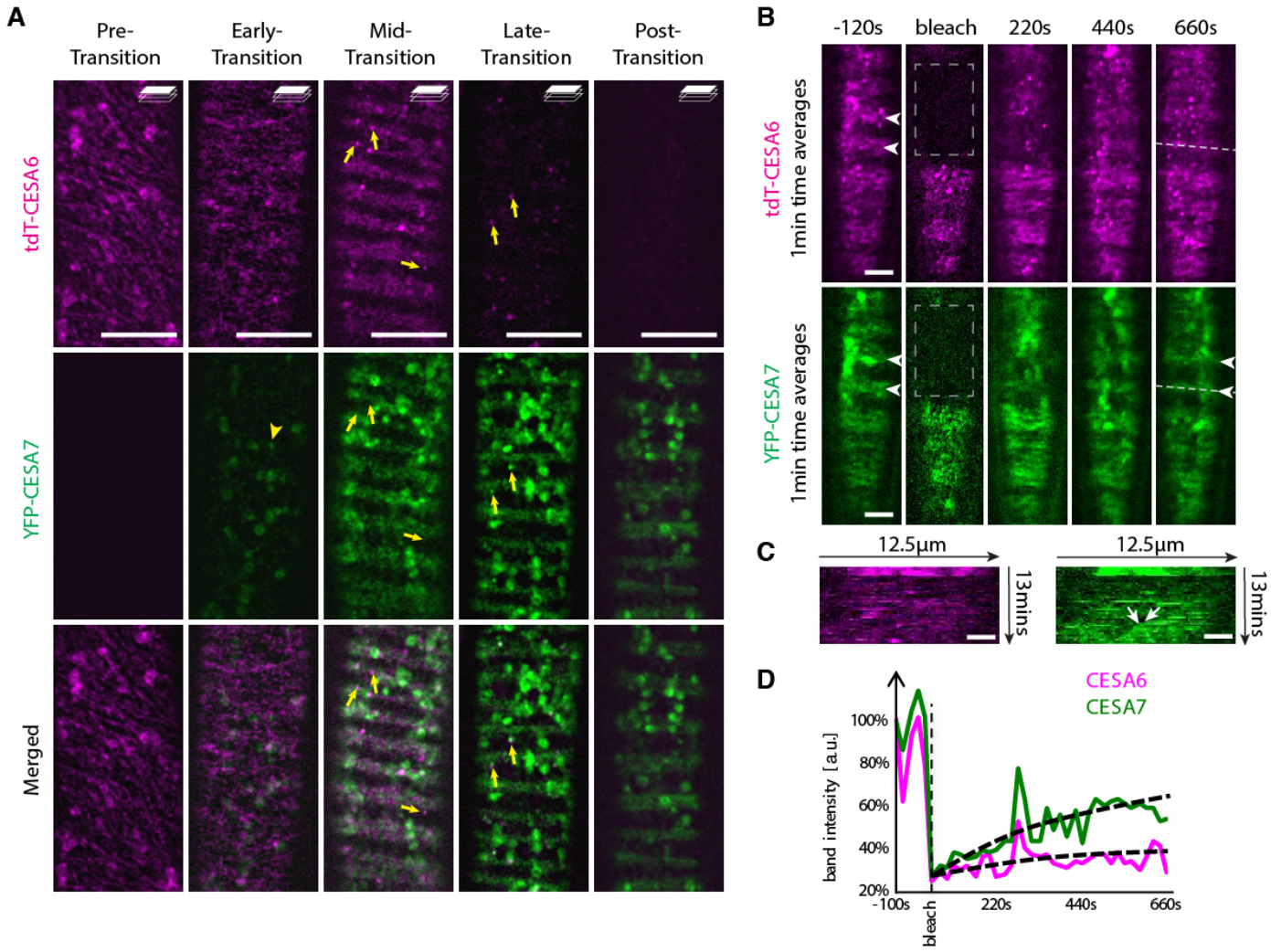

Figure 3-3: Primary cell wall cellulose synthase complexes briefly co-exist with, and are subsequently replaced by, secondary cell wall complexes

Five-day-old etiolated hypocotyl cells expressing YFP-CESA7 (green) and tdTomato-CESA6 (tdT-CESA6; magenta) in the VND7-inducible background. (**A**) Pre-transition: tdTomato-CESA6 (tdT-CESA6)-containing CSCs are visible at the plasma membrane as a diffuse pattern in which they migrate along linear trajectories. Early-transition: YFP-CESA7-containing CSCs begin to appear in intracellular compartments, while tdT-CESA6 remains at the plasma membrane. Mid-transition: both YFP-CESA7 and tdT-CESA6 appear at the plasma membrane, and steadily migrate along diffuse bands. Here, tdT-CESA6 begin to appear in distinct and bright intracellular compartments including SmaCCs (arrowhead) that typically coincide with cortical microtubule bands (see also Figure 3-1B and D). Late transition: Only YFP-CESA7 signal was observed at the plasma membrane, while tdT-CESA6 was seen only within cortical compartments (arrows). Post transition: tdT-CESA6 fluorescence is no longer seen associated with distinct cortical compartments, and only

YFP-CESA7 signal is observed as distinct foci at the plasma membrane or cortical compartments. (**B**) Time-average images of induced dual-labeled tdt-CESA6 and YFP-CESA7 before and after photobleaching. Primary and secondary CSCs coexist in bands before photobleaching (arrowheads). tdT-CESA6 fails to be recruited to the bleached region after 11 min whereas YFP-CesA7 reappears at the location of the band (arrowheads). (**C**) Kymographs along dashed lines in (B) reveal that recovery of tdT-CESA6 fluorescence is largely due to vesicles moving in the cytoplasm while YFP-CESA7 fluorescence reappears also in the form of migrating dots (arrows) moving along previously bleached bands indicating newly delivered YFP-CESA7 containing CSCs. (**D**) Fluorescence recovery curves reveals slow to little recovery of tdT-CESA6 while YFP-CESA7 fluorescence recovers substantially better. Scale bar = 10 μm in (A), 5 μm in (B), 2 μm (C).

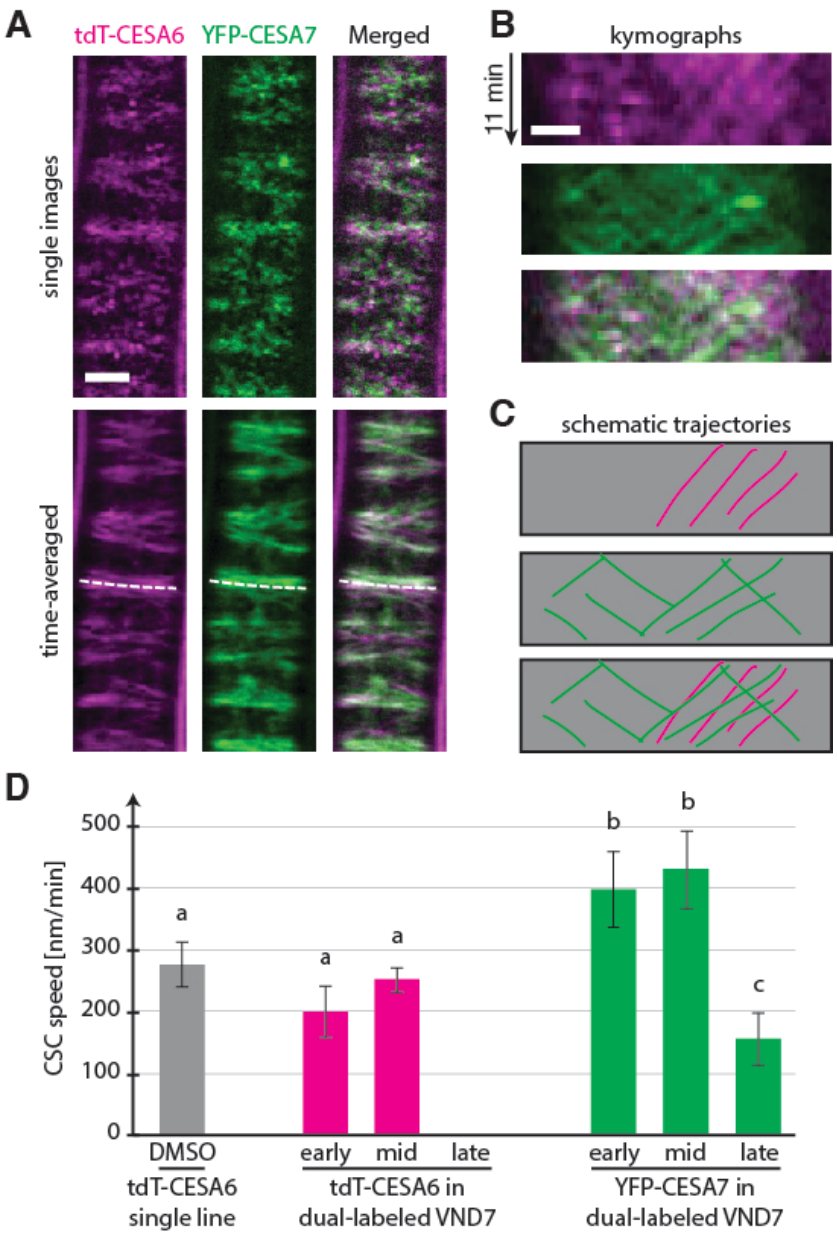

Figure 3-4: Primary cell wall CSCs move independently of secondary cell wall CSCs during xylem formation

Five-day-old etiolated hypocotyl cells expressing YFP-CESA7 (green) and tdTomato-CESA6 (tdT-CESA6; magenta) in the VND7-inducible background. (**A**) Single (top) and time-averaged (bottom) images of the fluorescent signals. For a short period during trans-differentiation, migratory primary and secondary cell wall CESAs co-occur along MT bands. (**B**) Kymograph plots along the dotted lines in (A) show clear differences in speed of tdT-CESA6 and YFP-CESA7 on the same MT bundle. (**C**) Schematic representation of tdT-CESA6 and YFP-CESA7 trajectories, respectively, present in (A). (**D**) CSC speed measurements in non-induced tdT-CesA6 and VND7-induced double-labelled tdT-CESA6 (magenta) and YFP-CESA7 (green) seedlings. Statistical test: Welch's unpaired *t*-test. Scale bars = 5 µm in (A) and 2 µm (B).

3.2.3 The cellulose synthesis inhibitor Isoxaben affects primary but not secondary cell wall CESA dynamics

The PCW CSC is highly sensitive to the cellulose synthesis inhibitor isoxaben in Arabidopsis (Scheible *et al.* 2001). Conversely, cellulose synthesis in grasses do not show the same type of sensitivity (Brabham *et al.* 2017). As there are populations of isoxaben-sensitive and insensitive CESAs, it is currently unclear to what degree Arabidopsis SCW CESAs are affected by the inhibitor. To assess how isoxaben affected the dynamic behavior of the tdTomato-CESA6 and YFP-CESA7, we first grew the VND7-inducible seedlings on normal MS media for three days in the dark and then transferred them to media containing 200 nM isoxaben for another day (Figure 3-5A). In non-induced seedlings, severe cell swellings were observed (Figure 3-5A). In contrast, the VND7-induced seedlings showed less swelling and were able to produce clear SCW bands (Figure 3-5A and B). Indeed, cell wall staining using the cellulose binding dye Scarlet S4B (Anderson *et al.* 2010) revealed clear cellulose bands in the VND7-induced seedlings; both in the absence and presence of isoxaben (Figure 3-5C). To assess how the isoxaben influenced CESA dynamics we first observed the tdTomato-CESA6 line and found, that the fluorescent foci disappeared from the PM and accumulated in internal SmaCCs/MASCs (Figure 3-5D). We next examined the behavior of the YFP-CESA7 in the VND7-induced seedlings. In contrast to tdTomato-CESA6, the YFP-CESA7 maintained steady movement at the PM and there were no differences in speed before and after isoxaben treatment (Figure 3-5E and F). We furthermore confirmed that the cellulose content was un-altered in the VND7 induced seedlings after isoxaben treatment, corroborating that SCW cellulose synthesis is not affected by isoxaben (Figure 3-5G). Hence, isoxaben might be used to perturb PCW cellulose synthesis while maintaining SCW cellulose synthesis intact.

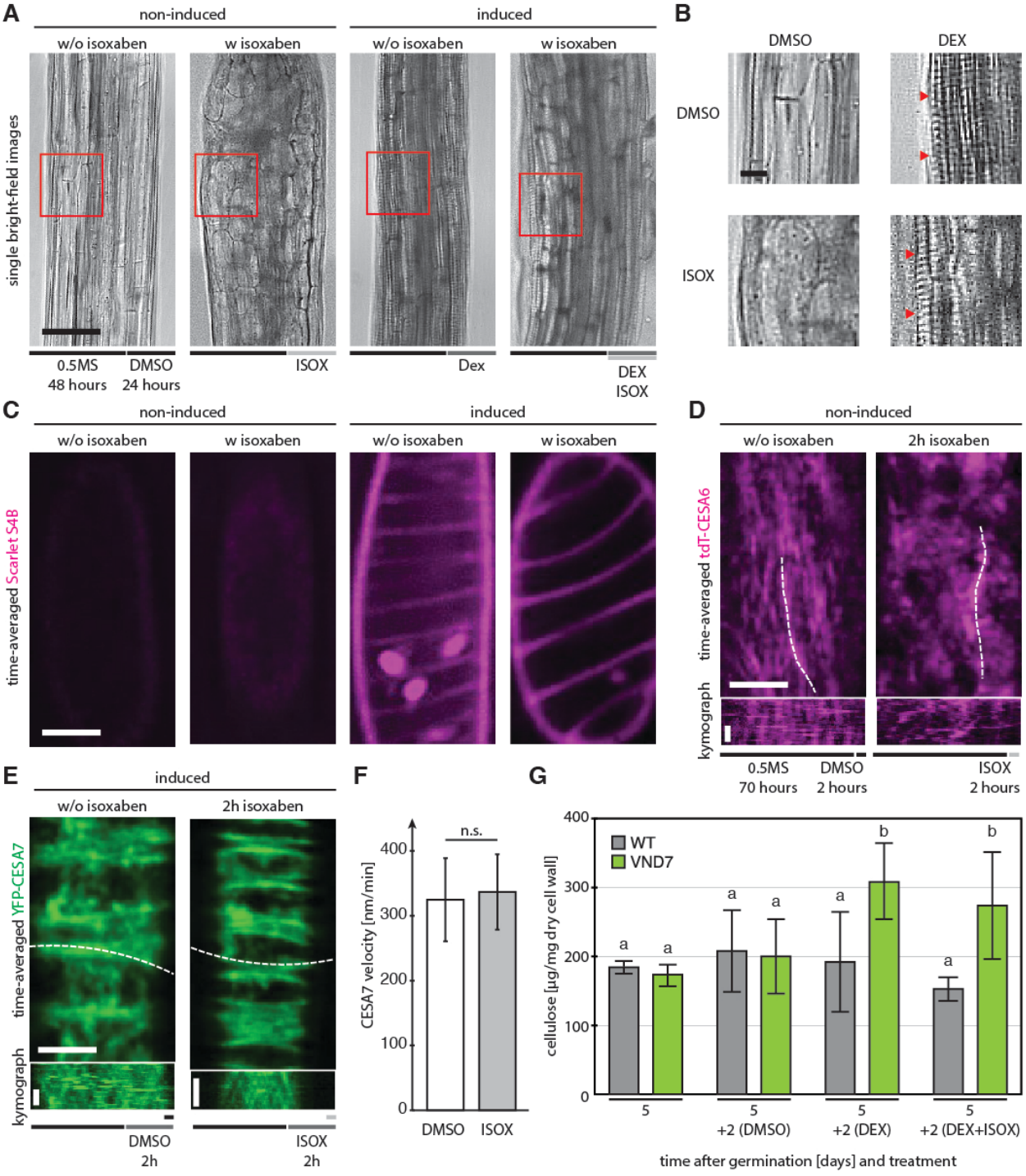

Figure 3-5: The potent cellulose-synthase inhibitor isoxaben affects primary cell wall CESAs, but not secondary cell wall CESAs, during patterned cell wall formation

(cont'd on next page)

(**A**) Three-day-old VND7 seedlings grown in the dark for two days and transferred to 200 nM isoxaben-containing plates for one day imaged using bright-field illumination. Isoxaben causes the cells of the upper hypocotyl to bulge (1st and 2nd image from left). After induction, hypocotyl cells trans-differentiate into proto-xylem cells and make SCWs as seen by the striated patterns (3rd from left and B). Adding isoxaben to induced seedlings leads to slight bulging of the upper hypocotyl cells while the trans-differentiation is not impaired (4th from left). (**B**) Zoomed-in images of red boxes in (A) showing clear xylem-like cell wall patterns (red arrow heads). (**C**) The cellulose stain Scarlet S4B allowed visualization of the secondary cell wall bands deposited after induction. Non-induced seedlings showed weak and non-specific labelling (1st and 2nd from left). Induced seedlings deposit large amounts of cellulose in band patterns in the absence and presence of isoxaben, respectively (3rd and 4th from left). (**D**) The effect of isoxaben was analyzed using five-day-old etiolated double-labelled tdT-CESA6 and YFP-CESA7 seedlings in the VND7-inducible background. Primary cell wall tdTomato-CESA6 (tdT-CESA6) foci move along linear tracks in the plasma membrane in non-treated and non-induced cells but are internalized within two hours after addition of 200 nM isoxaben (right image and kymograph below). (**E**) In contrast, secondary cell wall YFP-CESA7 foci remain at the plasma membrane and (**F)** move with similar speeds both in isoxaben and mock-treated cells. (**G**) Measurement of the cellulose content of induced and isoxaben-treated induced seedlings compared to non-treated controls of VND7 and Col-0 WT seedlings reveal that secondary cell wall production is unaffected by application of isoxaben. Scale bars = 100 µm in (A), 50 µm in (B), 10µm in (C to E) and 2 min in kymographs in (C to E).

3.2.4 Primary cell wall CESAs are internalized and trafficked to late endosomes/pre-vacuolar compartments during mid- to late xylem vessel development stages

The gradual loss of tdTomato-CESA6 signal at the PM indicated that it might be degraded. To assess this, we examined deeper optical sections within cells during the various stages of trans-differentiation to first elucidate the nature of the intracellular tdTomato-CESA6 localization (Figure 3-6A). Intracellular CESA compartments were defined as outlined in Figure 3-2. During the pre-transition stage, we observed cytosolic tdTomato-CESA6-labeled compartments including Golgi (arrowheads) and SmaCCs (yellow arrows; Figure 3-6A, pre-transition). Once the YFP-CESA7 became visible, the two fluorescently-labeled CESAs coincided in both Golgi and SmaCCs (Figure 3-6A to C, early-transition). As SmaCCs might be involved in both the delivery of CESAs to the PM as well as their endocytosis/recycling, we cannot determine if these dual-labelled SmaCCs are anterograde or retrograde in nature. However, as delivery of tdTomato-CESA6 stops once YFP-CESA7 is at the PM (Figure 3-3B), these SmaCCs are most likely compartments involved in CESA endocytosis and/or recycling. Interestingly, during mid-stages of the process, the Golgi-located tdTomato-CESA6 signal started to fade (arrowheads), and bright distinct puncta that did not coincide with YFP-CESA7 became apparent (white-arrows; Figure 3-6A, B). These compartments were distinct from YFP-CESA7 SmaCCs or tdTomato-CESA6 SmaCCs seen in earlier time points, as they were slightly larger and brighter than SmaCCs (Figure 3-2B). By late transition, no Golgi-localized tdTomato-CESA6 was detectable with a concurrent increase in diffuse tdTomato-CESA6 signal from the vacuole (Figure 3-6A and B). Once the transition was complete, only the diffuse vacuolar tdTomato-CESA6 signal remained (Figure 3-6A, post-transition). We quantified these shifts in localization using co-localization analysis of tdTomato-CESA6 and YFP-CESA7 (Figure 3-6C). Consistent with our observations, co-localization was highest during early-transition, when both proteins were present in the Golgi and SmaCCs, and steadily decreased at later time-points when the localization of tdTomato-CESA6 shifted to discrete puncta and to the vacuoles (Figure 3-6C).

The appearance of distinct tdTomato-CESA6 containing compartments, and the subsequent vacuolar signal, during the mid- and late transition phases prompted us to hypothesize that CESA6 was trafficked through pre-vacuolar compartments (PVCs)/multi-vesicular bodies (MVBs) to become degraded. If this is true, we expected that the number of puncta containing tdTomato-CESA6 exclusively would increase during the transition. Therefore, we measured the divergence of the tdTomato-CESA6 and YFP-CESA7 signals by quantifying loss of co-occurrence of tdTomato-CESA6 and YFP-CESA7 labeled compartments at different stages of transition (Fig 3-7A and B). At early-transition periods, $42 \pm 14\%$ of SmaCCs containing tdTomato-CESA6 did not co-occur with YFP-CESA7 fluorescence. This percentage remained the same at mid-transition with $44 \pm 6\%$ of tdTomato-CESA6 SmaCCs without YFP signal. However, by late transition phase, $55 \pm 9\%$ of the tdTomato-CESA6 labeled compartments contained only red fluorescence and hence not YFP-CESA7 (Fig 3-7C). To test if these tdTomato-CESA6-enriched compartments were PVC/MVB, we treated plants at early- to mid-transition stage with wortmannin (Fig 3-8), a pharmaceutical agent known to block CESA endocytosis (Fujimoto *et al.* 2015) and trafficking to the lytic vacuole by inhibiting phosphatidylinositol-phosphate-3 kinases (PIP3K) (Robinson *et al.* 2008). In cells treated with wortmannin, the tdTomato-CESA6-containing puncta still formed. However, in the treated cells, unlike DMSO-treated controls at the same time-point, we did not observe any tdTomato-CESA6 vacuolar signal (Figure 3-8), indicating that wortmannin treatment inhibited tdTomato-CESA6 trafficking to the vacuole.

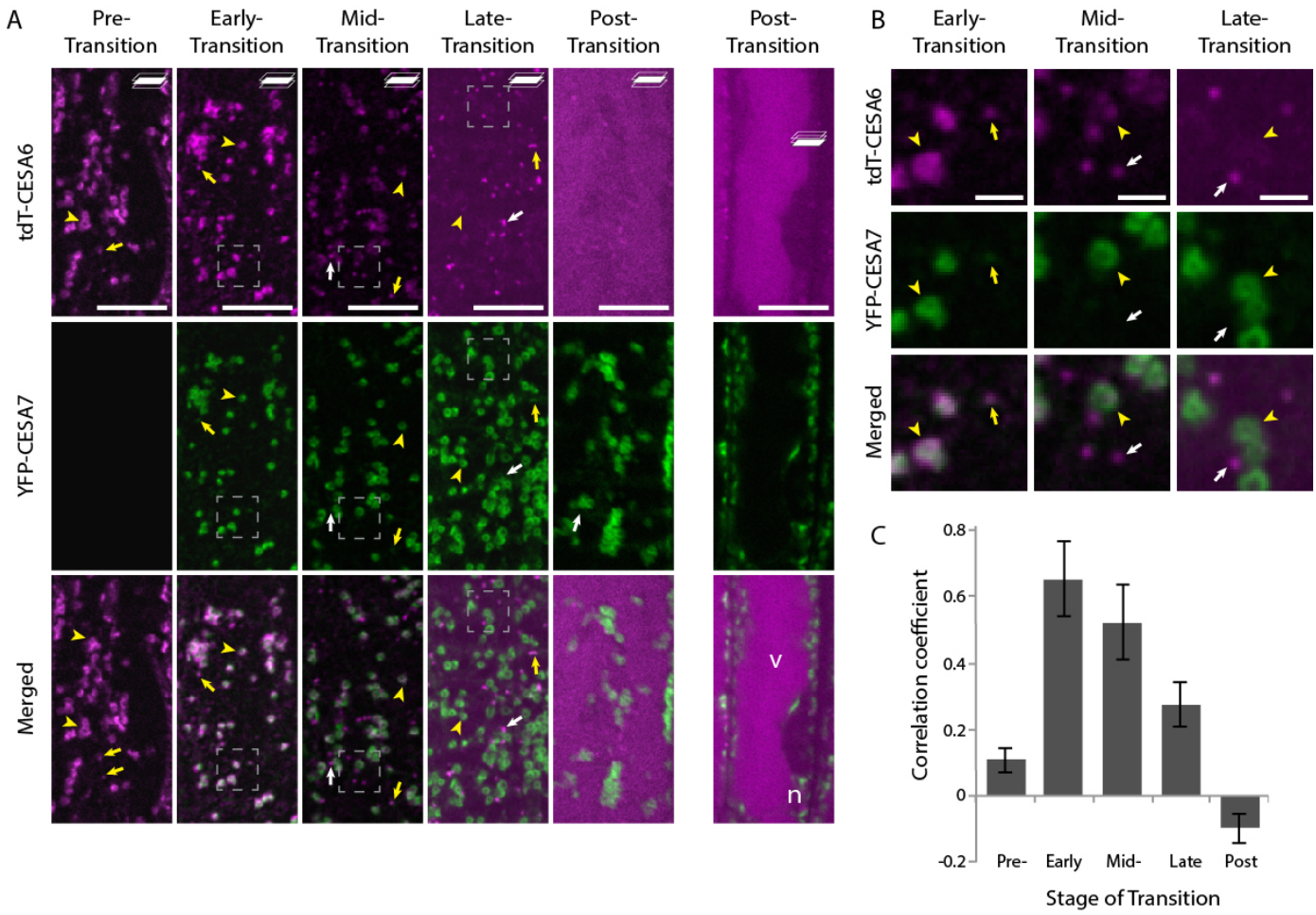

Figure 3-6: Primary cell wall CSCs are trafficked to distinct intracellular compartments and eventually to the vacuole where they are degraded

Five-day-old etiolated epidermal hypocotyl cells expressing YFP-CESA7 (green) and tdTomato-CESA6 (tdT-CESA6; magenta) in the VND7-inducible background. (**A**) Time course of intracellular signal for tdT-CESA6 and YFP-CESA7 during transition. Pre-transition: No YFP-CESA7 signal is observed. Early-transition: YFP-CESA7 fluorescence co-occurs with tdT-CESA6 in Golgi apparatus, but only tdT-CESA6 fluorescence is found associated with SmaCCs (arrowheads). Mid-transition: Both YFP-CESA7 and tdT-CESA6 signals are seen within Golgi and SmaCCs (arrowheads), while tdT-CESA6 fluorescence is also apparent within distinct cortical compartments (arrows). Late-transition: Only YFP-CESA7 signal is seen in Golgi and SmaCCs (arrowheads) while tdT-CESA6 fluorescence is seen as distinct cytosolic puncta (arrows). Post-transition: tdT-CESA6 is only seen as diffuse intracellular signal within the vacuole (v), evident at deeper optical planes where the void in fluorescence is caused by the nucleus (n). (**B**) Zoom-in insets from (A) show the differences in localization between tdT-CESA6 and YFP-CESA7 fluorescence within SmaCCs (arrowheads) and bright puncta (arrows) as transition progresses. (**C**) Correlation coefficient for co-localization of YFP-CESA7 and tdT-CESA6 at the different stages (A). For each stage 10 cells from three plants were used to quantify co-localization. Scale bars = 10 μm in (A), 2 μm in (B).

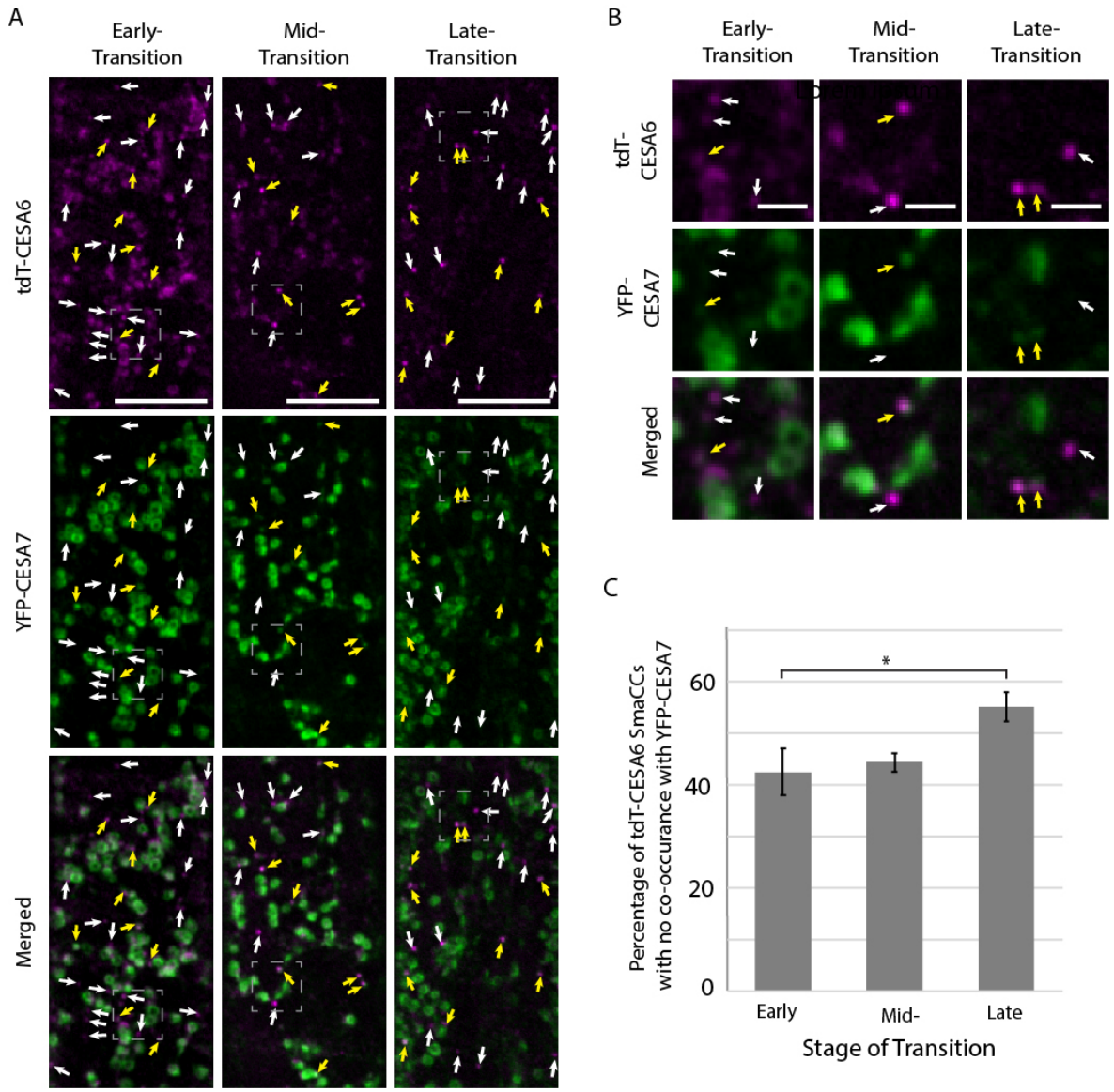

Figure 3-7: tdT-CESA6 puncta are a distinct population of SmaCCs that do not co-occur with YFP-CESA7

(A) Time course of intracellular signal for tdTomato-CESA6 (tdT-CESA6) and YFP-CESA7 during transition showing SmaCCs that contain both YFP-CESA7 and tdT-CESA6 (yellow-arrows) and SmaCCs that contain only tdT-CESA6 (white-arrows). (**B**) zoom-in insets from (A) showing the differences in localization between tdT-CESA6 and YFP-CESA7 as transition progresses. (**C**) Percentage of tdT-CESA6 containing SmaCCs that are independent of YFP-CESA7. N = 10 cells per time point, bars represent SE. * indicates statistically significant difference ($p < 0.05$) Statistical test: Tukey's pairwise analysis. Scale bars = 10 µm in (A), 2 µm (B).

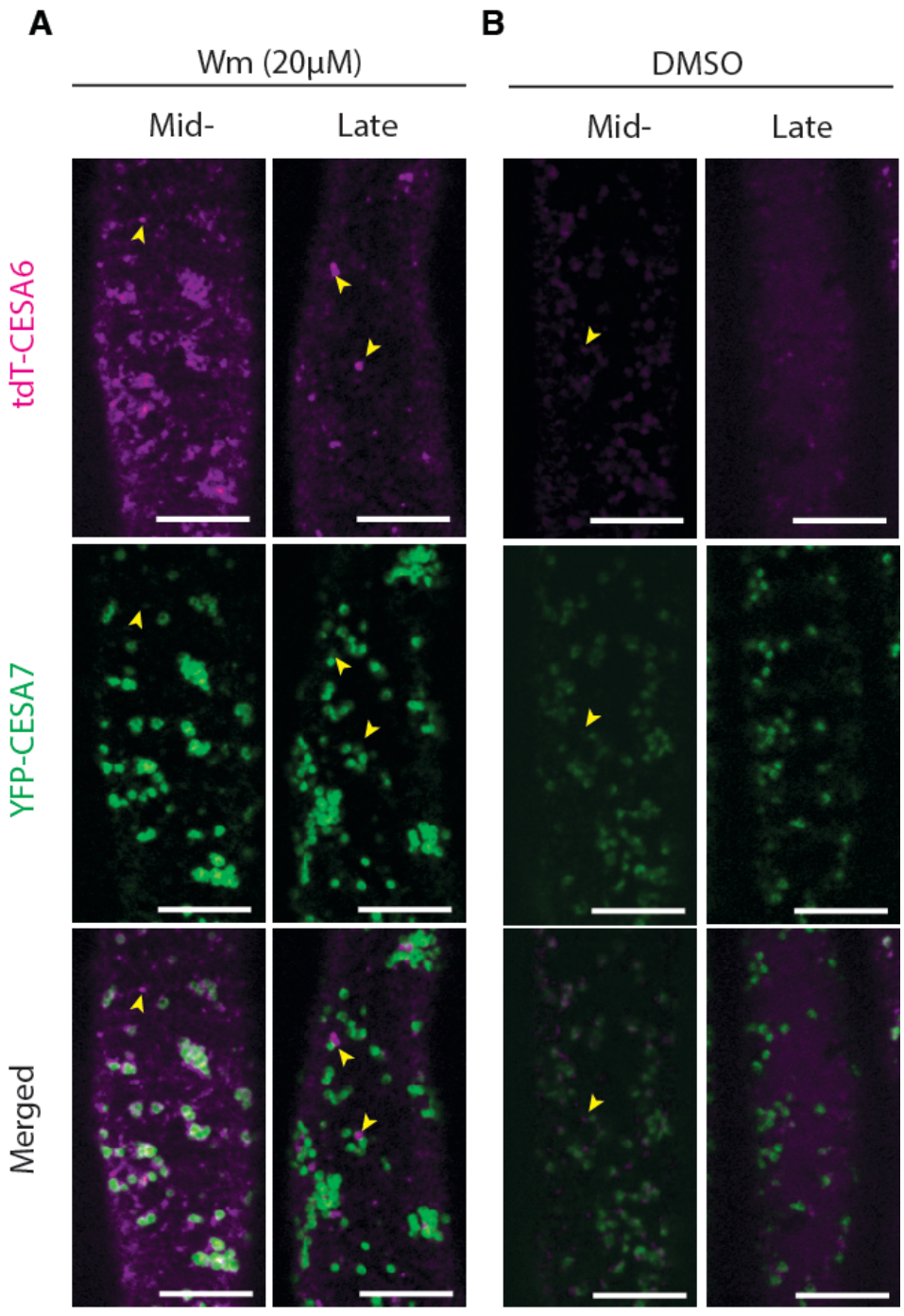

Figure 3-8: Wortmannin treatment prevents the appearance of tdT-CESA6 in the vacuole

(**A**) Time course of induced seedlings treated with 20 μM wortmannin at early stage of transition and imaged at mid- to late-transition stages (~10 hours post induction). Wortmannin does not prevent the formation of tdTomato-CESA6 (tdT-CESA6) puncta (arrows), but does prevent the appearance of tdT-CESA6 in the vacuole. (**B**) DMSO control treated samples did not show any inhibition of the removal of Golgi signal or the formation of distinct tdT-CESA6 puncta or vacuolar signal. Scale Bars = 10μm.

3.2.5 Primary cell wall CESAs are degraded as secondary cell wall CESAs accumulate during xylem tracheary element trans-differentiation

Although we show that tdTomato-CESA6 disappears from the PM and appears in the lytic vacuoles, while YFP-CESA7 is rapidly accumulating during the transition from primary to secondary cell wall synthesis, the question remains whether other CESAs behave similarly. To determine if the other PCW-specific CESAs (i.e. CESA1 and 3) are degraded while the SCW-specific (i.e. CESAs, CESA4 and 8) are accumulating we collected protein extracts during the trans-differentiation and performed Western blots using antibodies specific for the different CESA isoforms (Hill Jr. *et al.* 2014)(Figure 3-9). We used samples from wild-type *proCaMV35S::VND7-GR-VP16* that were non-induced, induced for 6h (early-transition), 12h (mid transition), 18h (late-transition) and 24h (post-transition). Consistent with our confocal data, the PCW CESA protein abundance steadily decreased in a concerted fashion, while the SCW-specific CESAs accumulated over time (Figure 3-9). These data support our hypothesis that the PCW CESAs are targeted to the vacuole for degradation during trans-differentiation.

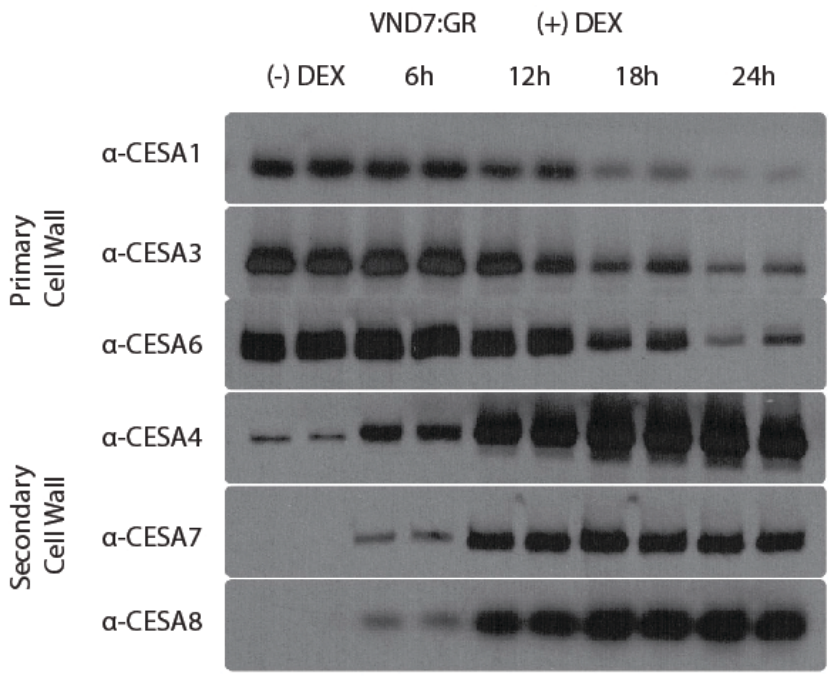

Figure 3-9: All primary cell wall CESAs are degraded upon VND7-GR induction as secondary cell wall CESAs accumulate

Western blots of an induction time-course of VND7-GR seedlings show that accumulation of secondary cell wall CESAs (CESA4, CESA7 and CESA8) and degradation of primary cell wall CESAs (CESA1, CESA3, and CESA6) are consistent among CESA isoforms.

3.3 Discussion

The transition from PCW to SCW synthesis represents a major shift in cellular developmental processes including transcription and post-translation modifications (Yamaguchi et al., 2011). A general shift from primary to SCW *CESA* expression has been well documented via transcriptome analysis (Persson *et al.* 2005; Yamaguchi *et al.* 2011). However, the brief and highly regulated nature of the distinct transitional phases of this major developmental modification has made it very difficult to visualize this process. By using live cell imaging and the inducible VND7-GR system, the sequence of events for CESA transition can be characterized and compared to the events during trans-differentiation, as described in chapter 2 (Fig 3-10). Here, we show in detail the dynamic change in PCW and SCW cellulose synthesis, and demonstrate how PCW and SCW CESAs are coordinated during the differentiation of protoxylem tracheary elements.

3.3.1 Primary cell wall CESAs are selectively targeted to the lytic vacuole for degradation

During transition, PCW CESAs are no longer delivered to the PM and instead, are selectively targeted into distinct compartments for transport to the lytic vacuole (Figure 3-11). This occurs all while SCW-specific CESAs are synthesized and accumulating within intracellular compartments and delivered to the PM where they appear in dense arrays along the MT-rich SCW domains. The selective targeting of PCW CESAs into a distinctive set of intracellular compartments from the SmaCCs, and finally to the lytic vacuole, hints at a mechanism involving protein-modification through phosphorylation or ubiquitination. Indeed, selective inactivation of PM protein by endocytosis and degradation via ubiquitination has been well characterized (Korbei and Luschnig 2013), and has been demonstrated for several PM proteins including the auxin-efflux protein PIN2 (Abas *et al.* 2006) and the boron carrier BOR1 (Kasai *et al.* 2011). Interestingly, CESAs have several conserved phosphorylation sites (Carroll and Specht 2011) which have been shown to not only affect their activity (Chen *et al.* 2010, 2016; Bischoff *et al.* 2011; Sánchez-Rodríguez *et al.* 2017), but also cause their selective degradation via a proteasome pathway (Taylor 2007).

The formation of pre-vacuolar CESA6 compartments during wortmannin treatment and the disappearance of Golgi signal imply that delivery of the PCW CESAs to the vacuole may come from intracellular compartments including Golgi and the TGN. However, this does not exclude the possibility that CESAs are targeted for degradation while still at the PM. Another PM protein, PIN2, that parallels CESAs in terms of trafficking (Abas *et al.* 2006; Bashline *et al.* 2014) has been shown to be mono-ubiquitinated at the PM before being poly-ubiquitinated at the TGN and targeted to the vacuole (Leitner *et al.* 2012). Previous work has shown that CESAs are delivered, in part, via a TGN-associated pathway as shown by the presence and accumulation of CESA3 within TGN (Crowell *et al.* 2009). Since the TGN acts as an important sorting hub for endocytosis, exocytosis, and recycling (Viotti *et al.* 2010), it is tempting to speculate that a pathway similar to PINs exists for CESAs. In such a case, PM localized CESAs are mono-ubiquitinated, marking them for endocytosis, and poly-ubiquitinated once in TGN, which would target them for degradation. Indeed, this may explain our observation of compartments containing both tdTomato-CESA6 and YFP-CESA7 even at late stages of transition, as these may be TGNs that are involved in targeting CESA6 for degradation while transporting/recycling CESA7 to the PM. However, further work is required to conclusively support this hypothesis.

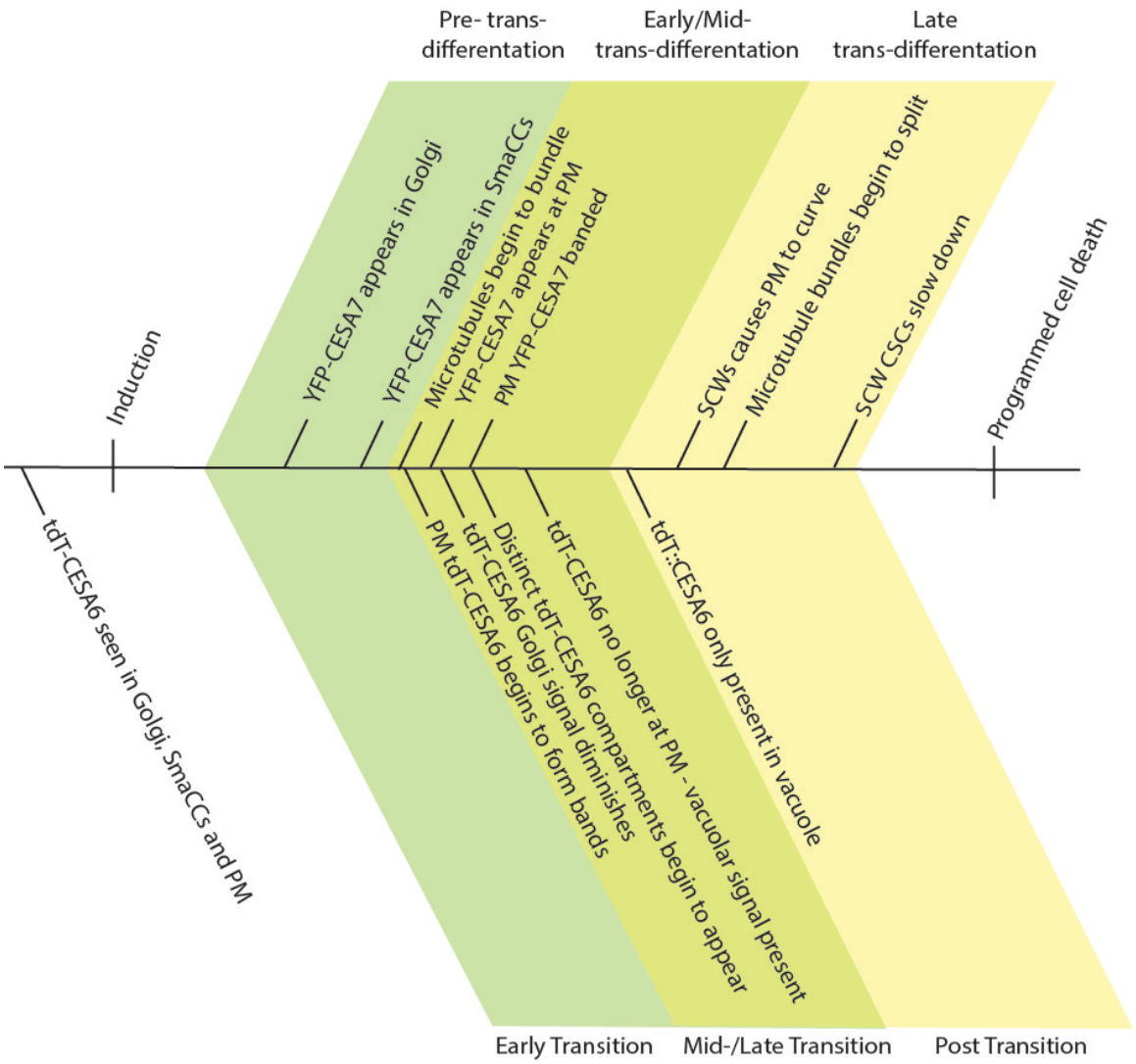

Figure 3-10: Timeline of PCW and SCW CESA localization during the transition from primary to secondary cell wall production

As CESA transition (lower-half) overlaps with the early stages of trans-differentiation (upper-half, chapter 2), the characteristics used to the describe each stage are summarized.

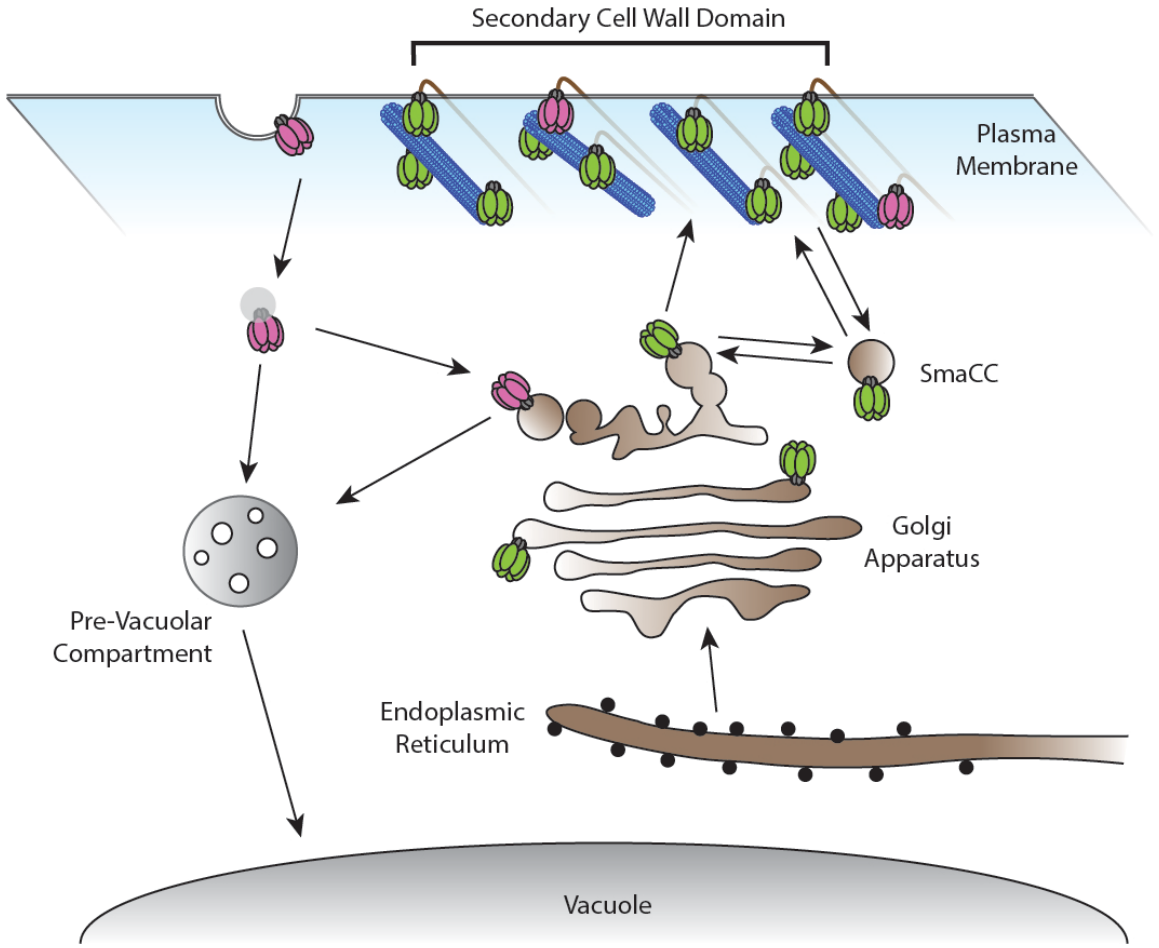

Figure 3-11: Trafficking of PCW and SCW CESAs are distinct during the transition from primary to secondary cell wall production

As secondary cell wall CESAs (Green) begin to be synthesized and trafficked to the plasma membrane at sites of secondary cell wall production marked by microtubules (Dark Blue), primary cell wall CESAs (Pink) briefly continue to contribute to cellulose production within those regions. Conversely, primary cell wall CESAs are no longer being synthesized and remaining proteins are targeted to pre-vacuolar compartments and ultimately to the lytic vacuole for degradation.

3.3.2 Complexes containing a mix of primary and secondary cell wall CESAs are unlikely to exist during the transition to secondary cell wall synthesis

It is well-established that two distinct sets of CESAs are required for the production of PCW and SCW cellulose (McFarlane *et al.* 2014). However, at least one study has suggested that there might be a degree of overlapping functionality, as *CESA1* driven by a *CESA7* promoter in a *cesa8* mutant partially complemented the *cesa8* phenotype (Carroll *et al.* 2012). While we cannot completely rule out the presence of mixed CSCs that contain both PCW and SCW CESAs, our data does not support that such mixed CSCs would contribute to cellulose production to any major extent during the transition between PCW and SCW synthesis. We base these conclusions on the different speeds of the two CSCs, the very brief overlap of the tdTomato-CESA6 and YFP-CESA7 and differences in isoxaben sensitivity. Indeed, screens for isoxaben resistant Arabidopsis mutants have been undertaken and the most prominent mutations affect amino acids in CESA3 and CESA6 that are referred to as *ixr1* (*ixr1-1* and *ixr1-2*) and *ixr2* (*ixr2-1*) mutants, respectively (Scheible *et al.* 2001; Desprez *et al.* 2002). This makes it unlikely that at least CESA3 and CESA6 would be part of any SCW CSCs as these CSCs are insensitive to the inhibitor.

Although, the presence of a fluorescent tag on some of the CESA proteins examined in this work may affect interactions between the two CSC-related CESAs (primary and secondary), previous work has shown that these interactions, if present, are generally weak and only occur when the "correct" CESA is missing (Carroll *et al.* 2012). Moreover, it maybe that CESA8 can be replaced by CESA1, and that the partial-complementation phenotype in these plants is due to the degradation of CESA1. However, recent work creating a comprehensive set of hybrid SCW-specific CESAs supports the hypothesis that isoform specificity is due to each CESA having a very specific location and fit within the complex (Kumar *et al.* 2017). Indeed, Kumar *et al.* (2017) showed that CESA8 is the most accepting of other CESA domains, implying that it may be located at the periphery of the complex and therefore explain why CESA1, which

according to our current findings could have a brief over-lapping transition period, can partially replace CESA8 in the Carroll *et al.* (2012) study.

The transition from PCW production to SCW production represents a critical step in plant development and biomass production, involving the complete turnover of the CESA machinery. Although both CSCs make largely the same fundamental product, cellulose, the end product quality is significantly different. Generally, cellulose in the SCWs have a higher degree of crystallinity and polymerization (Joshi and Mansfield 2007). While the enzymatic and cellular processes that contributes to, and control these, polymeric qualities are not fully understood, we outline a first comprehensive evaluation of the coordination of PCW and SCW cellulose synthesis during this important process.

3.4 Materials and Methods

3.4.1 Generation of plant lines

Seeds of cesa7^{irx3-4} plants containing *proCESA7::YFP-CESA7* and *proCaMV35S::VND7-VP16-GR* (Watanabe *et al*. 2015) were crossed with cesa6^{prc1-1} lines containing *proCESA6::tdTomato-CESA6* (Sampathkumar *et al*. 2013) and F_3 lines homozygous for all 3 constructs were isolated. Further, seeds of *proCaMV35S::YFP-TUA5* (Kirik *et al.* 2012) were crossed with *proCaMV35S::VND7-VP16-GR* and F3 lines positive for all 3 constructs were used for imaging.

3.4.2 Seedling growth and induction

Seeds were surface sterilized with 20% bleach and 0.1% Triton (Sigma) for 5 min, and then washed three times with sterilized distilled water. Seeds were sown on plates containing germination media (1× Murashige-Skoog (MS), 1% Sucrose, 1x Gamborg's Vitamin mix, 0.05% MES, 0.8% agar at pH 5.8). Plates were wrapped in aluminum foil and placed at 4°C for 2 days, before being moved into a growth chamber at 21 °C in a vertical position and grown for 3 days. Plates were then removed from the chamber and under sterile conditions, 10 ml of 10 µM dexamethasone (Sigma) in sterilized distilled deionized water was added on the plates for VND7-GR induction. Plates were then rewrapped in aluminum foil and grown in the dark in a chamber for an additional 8 h (earliest stages of SCW formation) before imaging began. Imaging was carried out between 8 - 18 h following induction. The timing of induction varied slightly among cells in each seedling, so stage of transition was either defined based on the status of the MT array or the presence of YFP-CESA7 signal and the localization of tdTomato-CESA6. Cells at the early stages of transition were defined as when YFP-CESA7 signal was detectable but only in Golgi, while tdTomato-CESA6 was present in both the Golgi and at PM. Mid-transition cells were defined when both YFP-CESA7 signal and tdTomato-CESA6 was present at the PM. Late-transition cell were defined when only YFP-ESA7 was present at the PM, and tdTomato-CESA6 was only seen in intracellular compartments, including puncta and the

vacuole. Post-transition was defined to when tdTomato-CESA6 was only seen within the vacuole.

3.4.3 Drug treatments

Seedlings grown in the dark for 2 days were transferred to plates containing 10 μM dexamethasone and/or 200 nM isoxaben and placed in the dark for another day. Seedlings were then incubated in 0.01 % Scarlet S4B (Direct Red 23) for 10-20 min and rinsed with water as described in (Liesche *et al.* 2013) and subsequently imaged.

For the cell wall content analysis, *proCaMV35S::VND7-VP16-GR* seedlings were dark-grown in liquid ½ MS cultures for 5 days and subsequently treated with DMSO (mock), 10 mM dexamethasone (final concentration = 10 μM), and/or 1 mM isoxaben (final concentration = 200 nM) for another two days. Samples were collected after 5 and 7 days.

Wortmannin (Wm, Alfa Aesar) was dissolved in DMSO at a stock concentration of 20mM and used as a working concentration of 20μM. 10 h induced seedlings were submerged in either 1ml of 20μM 0.1% DMSO in ½ MS liquid media or 0.1%DMSO in ½ MS liquid media, as a control, and placed under gentle vacuum for 5 minutes to aid in drug penetration. Samples were then washed with ½ MS liquid media twice and then mounted for imaging.

3.4.4 Live cell imaging

Seedlings were mounted between #1.5 45×40 and 24×24 mm coverslips with water and sealed with silicone vacuum grease.

Imaging for time course and wortmannin treated experiments was performed on two different spinning disk confocal instruments located in the partner labs in Vancouver and Melbourne. The former consisted of a Leica DMi8 inverted microscope equipped with a Perkin-Elmer UltraView Yokogawa CSU-X1 spinning-disk system and a Hamamatsu

9100-13-CSU-X1 EMCCD Camera and a 100X 1.4NA oil lens. The latter consisted of an inverted Nikon Ti-E microscope) equipped with a CSU-W1 spinning disk head (Yokogawa), a deep-cooled iXon Ultra 888 EM-CCD (Andor Technology, Northern Ireland) and an 100x oil-immersion objective (Apo TIRF, NA 1.49). In both cases, YFP was imaged using a 514-nm laser and 540/30 emission filter, while RFP was detected with a 561-nm laser and 595/50-nm emission filter. Images were captured using the Volocity 6.3 software package (Perkin Elmer) or MetaMorph (Molecular Devices, USA). The instrument in Melbourne additionally contained an Andor FRAPPA scanning instrument to allow for photobleaching experiments. FRAP was achieved by using a custom-made journal controlling the dual-color imaging (YFP and RFP) and two-color bleaching (100% 514- and 561-nm laser) with the MetaMorph software. Typical FRAP settings were 20 µs bleach time per pixel and up to 5 repetitions resulting in an approx. 2 to 5 second exposure to the bleach laser.

3.4.5 Image analysis

Images were processed using Fiji software (Schindelin *et al.* 2012). Background correction was performed using the "subtract background" tool with a rolling ball radius of 50 pixels. Occasionally the images had to be drift corrected which was done with the registration tools inbuilt into Fiji (Schindelin *et al.* 2012). The velocity of CSCs was measured using the open-source software FIESTA (Ruhnow *et al.* 2011), which allowed the velocity of moving CSCs to be determined by measuring their slopes in multiple kymograph projections within a short time.

3.4.6 Co-localization analysis

Co-localization analyses were performed in Volocity 6.3 (Perkin Elmer) using the co-localization analysis as described by Manders *et al*. (1993). Threshold was set to ROIs drawn in background areas. Individual cells were then selected as ROIs and correlation coefficients were calculated.

3.4.7 Cell wall analysis

Liquid cultures were harvested after 7 days in the dark. Seedlings were stored in 70% EtOH for one week. To extract cell wall material, seedlings were first air dried overnight in a 60°C oven. The dry material was then frozen in liquid nitrogen and homogenised to fine powder using metal balls and an oscillating mill (1 minute at 25 Hz) from Retsch (Haan, Germany). Cell wall powder was washed with pure ethanol and centrifuged at 13.000 rpm for 10 minutes. Subsequently, the pellet was resuspended in a 1:1 methanol:chloroform mixture and centrifuged again at 13.000 rpm for 10 minutes. Lastly, the pellet was re-suspended in pure acetone and centrifuged again at 13.000 rpm for 10 minutes. After that the cell wall pellet was air dried overnight. The dry, insoluble part of the cell wall material was weighed to approximately 700-800 µg per 2 mL screw-cap tube. Subsequently, 250 µL of 2 M trifluoracidic acid was added to the tubes and incubated for 1 h at 121 °C. Afterwards, the tubes were supplemented with 300 µL of 2-Propanol and left for evaporation under a steady air flow at 40 °C. This step was repeated two times before the tubes were supplemented with 300 µl distilled water, thoroughly vortexed and centrifuged at 13.000 rpm for 15 minutes. The pellet was further used to determine the amount of crystalline cellulose using the Updegraff method (Updegraph 1969).

3.4.8 Protein extraction and western analysis

Arabidopsis seedlings containing *proCaMV35S::VND7-VP16-GR* were grown for 4 days on plates before being induced as described above. 200mg of seedlings were harvested at each time point (6 h, 12 h, 18 h and 24 h) along with a DMSO control which was treated for 24 h as well and snap frozen with liquid nitrogen. Samples were then ground to a fine powder and resuspended in acetone containing 10% tricholoracetic acid to extract total protein was extracted (W Wang *et al.* 2006). Protein pellets were resuspended in dilute phosphate-buffered saline containing 1% SDS. Protein concentration was assayed using the Detergent compatible (DC) protein assay (Bio-Rad).

Samples were then diluted to 2mg/ml with SDS-loading buffer. 20µg of protein were then run on 8%SDS-PAGE gels with a 5% stacking gel and transferred to a 0.2µm pore nitrocellulose membrane (Bio-Rad) as described in (Hill Jr. *et al.* 2014). Primary antibodies were used at dilutions of 1:2000 for α-CESA1 and α-CESA4. 1:1500 for α-CESA6, 1:000 for α-CESA8, 1:700 for α-CESA3, and 1:500 for α-CESA7. Superclonal secondary antibody (Goat α-Rabbit IgG, Thermo Fisher) conjugated with the enhanced chemiluminescent (ECL) horseradish peroxidase (HRP) was used at concentrations of 1:30000 for α-CESA1, 1:20000 for α-CESA6, 1:15000 for α-CESA4, αCESA7 and α-CESA8, 1:10000 for α-CESA3. SuperSignal West Pico Chemiluminescent Substrate kit (Thermo Fisher) and CL-Xposure film (Thermo Fisher) was used to image westerns.

Chapter 4: Cellulose patterning defects in secondary cell wall *cesa* mutants

4.1 Introduction

Through expression analysis and mutant screens, it has become clear that proper cellulose synthesis in plants requires the presence of at least three different CESA classes. Of the three classes of CESAs involved in PCW production, null mutations in either *CESA1* or *CESA3* are gametophytic lethal (Persson *et al.* 2007). Loss of the third PCW CESA, *CESA6*, is not lethal due to its partial redundancy with the closely related *CESA2, CESA5 and CESA9* (Desprez *et al.* 2007; Persson *et al.* 2007). However, *cesa2/cesa6/cesa9* triple mutants are gametophytic lethal thus highlighting the need for three different CESA classes in PCW production (Persson *et al.* 2007). Despite the lethality of null mutations to PCW *CESAs,* leaky mutations of *AtCESA1* (such as *cesa1*^{rsw1}) or *AtCESA3* (such as *cesa3*^{eli1} and *cesa3*^{je5}) and some single null-mutants of the *AtCESA6*-class are viable and display growth defects associated with reduced cellulose production (Arioli *et al.* 1998; Fagard *et al.* 2000; Cano-Delgado *et al.* 2003; Desprez *et al.* 2007). These mutants also display reduced protein levels of their interacting CESA partners, suggesting that the CSC is unstable when one of the CESAs is lost or non-functional (Desprez *et al.* 2007).

The partial redundancy and/or lethality in PCW CESA mutants makes it difficult to determine how the loss of a CESA subunit affects CSC dynamics and cell wall architecture. Conversely, loss-of-function SCW *cesa* mutants are viable and have very limited redundancies with other CESAs (Turner and Somerville 1997; Taylor *et al.* 1999, 2000, 2003; Carroll *et al.* 2012). Null mutations to SCW *CESAs* exhibit weak fibers, collapsed xylem tracheary elements, and stunted growth stemming from reduced cellulose content in these tissues (Taylor *et al.* 1999, 2000, 2003; McDonnell 2010). Although all characterized null mutations of the secondary *CESAs* show a similar decrease in cellulose content (Taylor *et al.* 2003; Kumar *et al.* 2017), previous work by McDonnell (2010) showed that there are differences in the characteristics of the cellulose produced, including crystallinity, microfibril angle, and degree of polymerization, depending on which CESA is mutated and whether the mutation was a missense mutation that produced

a non-functional protein or a knock-out. For example, the knock-out mutants *cesa7*$^{irx3\text{-}1}$ and *cesa8*$^{irx1\text{-}1}$ have decreased cellulose crystallinity, while the knockout mutant *cesa4*$^{irx5\text{-}1}$ has near *wild-type* (WT) levels of cellulose crystallinity (McDonnell 2010). In contrast, the null mutants *cesa7*$^{irx3\text{-}1}$ *and cesa4*$^{irx5\text{-}1}$ show increases in cellulose microfibril angle, while the missense mutant *cesa8*$^{irx1\text{-}1}$ does not show a significant change (McDonnell 2010). For degree of polymerization, *cesa4*$^{irx5\text{-}1}$ and *cesa8*$^{irx1\text{-}1}$ had shorter cellulose chains, but *cesa7*$^{irx3\text{-}1}$ was similar to *wild-type*. This implies that each CESA may have a specific function in determining the quality of the cellulose being produced. However, the conclusions of McDonnell (2010), rely on the assumption that SCW CSCs are still functional even when one of the SCW CESAs is absent or nonfunctional.

It has been postulated that aberrant CSCs can form and be active despite the loss of one of the three CESAs within a complex (Arioli *et al.* 1998). However, previous work by Ha *et al.* (2002), using a combination of Fourier-Transform Infrared (FTIR) micro-spectroscopy and solid-state Nuclear Magnetic Resonance (NMR) to analyze the cell wall ultrastructure, showed that there are only low levels of crystalline cellulose in *cesa7*$^{irx3\text{-}1}$ fibers and xylem tracheary elements which they argue is coming from PCWs given the detection of pectin in their samples. This suggests that no cellulose is present within SCWs when one of the interacting CESAs is lost. Moreover, null mutations of SCW *CESAs* have been shown to lead to decreased protein levels of their interacting partners, further supporting the hypothesis that the CSCs are unstable when one of the CESAs are missing and that cellulose synthesis is prohibited (Atanassov *et al.* 2009; Hill Jr. *et al.* 2014).

Given the conflicting results of McDonnell (2010) and Ha *et al*. (2002), further examination of the cell wall phenotypes and cellular dynamics of SCW CESAs are needed. Previously, Gardiner *et al.* (2003) used immunofluorescence to localize CESA4, CESA7 and CESA8 proteins in developing xylem tracheary elements in roots of *cesa7*$^{irx3\text{-}1}$, *cesa4*$^{irx5\text{-}1}$ *and cesa8*$^{irx1\text{-}1}$ mutants. The knock-out mutations in *cesa7*$^{irx3\text{-}1}$ and *cesa4*$^{irx5\text{-}1}$ both caused a loss of proper banded localization of their respective partners, while the missense mutation in *cesa8*$^{irx1\text{-}1}$ did not (Gardiner *et al.* 2003). These observations support a model in which CESAs are unable to be properly trafficked to SCW domains of the PM when one

of their partners is missing. However, the limited resolution caused by the depth of these cell types in tissue, does not preclude that the incomplete CSCs could be trafficked to the PM and localize diffusely throughout it. Support for the latter hypothesis stems from the isolation of the *baculities-like1* (*bacl-1*) mutant from collaborators in Taku Demura's lab at the Nara Institute of Science and Technology (unpublished). The *bacl-1* mutant was identified through a forward mutagenesis screen of plants containing *proCaMV35S::VND7-VP16-GR* to detect mutants with defects in SCW patterning in induced cells. The *bacl-1* mutant showed a near complete lack of SCW patterning in induced seedlings (Figure 4-1) and was later determined to be a null mutant of *cesa7* (unpublished). The lack of banding of SCWs would support the idea that cellulose production is prohibited in this null mutant. However, cell wall monosaccharide analysis revealed that cellulose production in *bacl-1* upon induction was still upregulated as the mutant showed an increase in glucose content similar to WT VND7-GR plants (unpublished). In-line with this, staining with the cellulose-specific stain, Pontamine fast Scarlet 4B (S4B) revealed that cellulose was being deposited after VND7-GR induction, just not in bands, but diffusely throughout the wall, similar to cellulose production in primary cell walls (PCWs) (unpublished). Additionally, the secreted hemicellulose, xylan, was found to be deposited in normal SCW banding patterns (unpublished).

Given the surprising observations seen in the null mutant *cesa7*$^{bacl-1}$, in this work, I asked if these phenotypes were consistent with other knock-out alleles of *cesa7*, as well as knock-outs of *cesa4* and *cesa8* in the VND7-GR induction system. Furthermore, I sought to determine the sub-cellular localization of the functional WT CESAs when one of their interacting CESA partners are missing, such as in one of the knock-out mutant backgrounds.

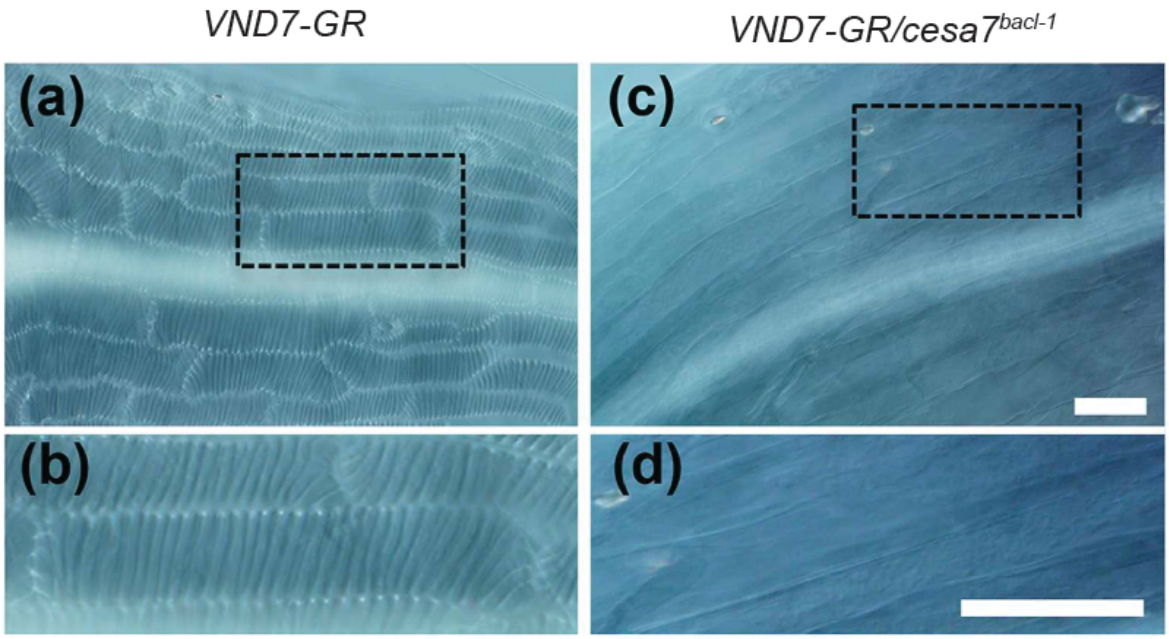

Figure 4-1: The *cesa7*$^{bacl-1}$ mutant displays a lack of secondary cell wall banding pattern (**A**) Differential interference contrast (DIC) images of epidermal hypocotyl cells of 6-day old seedlings after 48 hours of VND7-GR induction. (**B**) Zoom in of boxed area in (A) shows typical protoxylem-like banding pattern of secondary cell walls. (**C**) Epidermal hypocotyl cells of 6-day old seedlings after 48 hours of VND7-GR induction in the *cesa7*$^{bacl-1}$ mutant background. (**D**) Zoom in of boxed area in (C) reveals a complete lack of a banding pattern of secondary cell walls. Scale bars = 100 μm. Figure prepared by Yuto Takanaka (unpublished).

4.2 Results

4.2.1 *cesa7* knock-out mutants display patterned, but thinner secondary cell walls

In order to determine if the observed lack of SCW banding observed in *cesa7*$^{bacl-1}$ mutants was consistent with other *cesa7* knockout mutants, I crossed the *proCaMV35S::VND7-VP16-GR* construct into two *cesa7* knock-out mutants, the T-DNA mutant *ces7*$^{irx3-4}$, and the missense mutant *cesa7*$^{irx3-1}$, that contains a premature stop codon and produces no detectable protein (Taylor *et al.* 1999; Atanassov *et al.* 2009). Plants homozygous for both VND7-GR and the *cesa7* mutations were isolated and induced for 48-hours to permit complete induction to occur. On first inspection with bright-field light microscopy (Figure 4-2A), SCW bands seemed to be absent when compared to WT, which showed clear thick bands of SCW (arrowheads, Figure 4-2A). However, an uneven surface on the SCW bands was observed in *cesa7* mutants indicating the possible presence of SCW bands (arrows, Figure 4-2A). Samples were then stained with propidium iodide (PI), a fluorescent stain that labels cell walls red (Helariutta *et al.* 2000), and imaged using confocal microscopy (Figure 4-2A). In WT VND7-GR plants, the thick SCWs were intensely stained by PI (arrows, Figure 4-2A), and in both the *cesa7*$^{irx3-1}$ and *cesa7*$^{irx3-4}$ mutant backgrounds, banded patterns of SCWs were apparent (arrowheads, Figure,4-2A). The quantification of the SCW's thickness showed that the *ces7*$^{irx3-4}$ and *cesa7*$^{irx3-1}$ SCWs were significantly thinner than those observed in WT VND7-GR plants (Figure 4-2B, C). Thus, both *ces7*$^{irx3-4}$ and *cesa7*$^{irx3-1}$ in the VND7-GR induction system show normal patterns of SCW banding, but have SCW that are much thinner than WT.

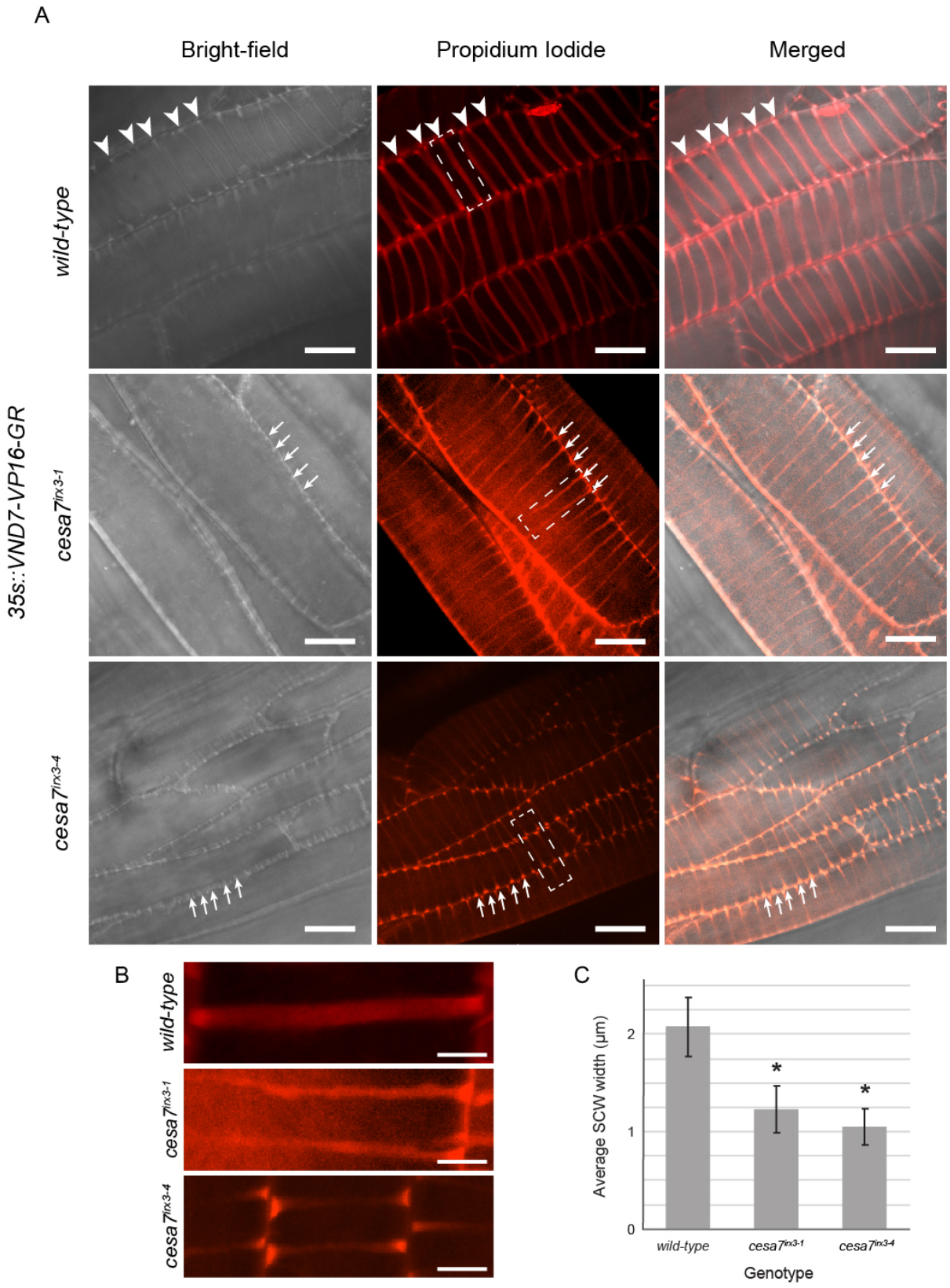

Figure 4-2: *cesa7* knockout mutants have banded, but thinner secondary cell walls
(cont'd on next page)

(**A**) Z-projection images of 48-hour VND7-GR induced epidermal cells of 5-day old light-grown hypocotyls in wild-type (WT) and *cesa7* knockout mutant backgrounds. In WT, clear thick secondary cell walls (SCWs) are visible both in bright-field and propidium iodide (PI) staining (arrowheads). In both *cesa7*$^{irx3\text{-}1}$ and *cesa7*$^{irx3\text{-}4}$ knockout mutants, SCWs are not clearly visible with bright-field, but are with propidium iodide staining (arrows). (**B**) Zoom-ins of boxed areas in (A) highlights the thin SCWs (arrows) present in *cesa7* mutants. (**C**) Average width of SCWs stained with PI. SCW widths were measured at the widest point for a SCW band. For each genotype 15 SCW bands were measured per cell in a total of 10 cells per genotype, from a total of 3 plants (n=10). (*) denotes significant difference from WT (Tukey's pairwise comparison, $p < 0.01$). Bars = SD. Scale bar = 20μm in (A), 5μm in (B).

4.2.2 *cesa4*$^{irx5-4}$ and *cesa8*$^{irx1-5}$ knock-out mutants have banded secondary cell walls that are different from *cesa7* mutants

Since cellulose synthesis requires three distinct CESAs, I next sought to determine whether the aberrant SCWs observed in *cesa7* knockout mutants in induced VND7-GR cells also occur when CESA7's interacting partners, CESA4 and CESA8, are missing instead. I thus crossed the *proCaMV35S::VND7-VP16-GR* construct into the T-DNA knockouts mutant alleles, *cesa4*$^{irx5-4}$ and *cesa8*$^{irx1-5}$ (Hill Jr. *et al.* 2014). Surprisingly, thick bands of SCWs similar to those common to WT were apparent with bright-field light microscopy in VND7-GR-induced cells in both *cesa4*$^{irx5-4}$ and *cesa8*$^{irx1-5}$ mutant backgrounds (arrowheads, Figure 4-3A). However, upon staining with PI, it became apparent that these SCWs were less uniform in terms of their structure, as an uneven, rugged surface on the SCW bands was observed (arrows, Figure 4-3A and B) and the SCW structure was more diffuse. SCW thickness quantification showed that the *cesa4*$^{irx5-4}$ and *cesa8*$^{irx1-5}$ SCW bands were thicker than the WT bands (Figure 4-3C). The contrasting phenotypes observed in *cesa7* and *cesa4/cesa8* knockout mutants hinted at a possible difference in cell wall composition or architecture among them.

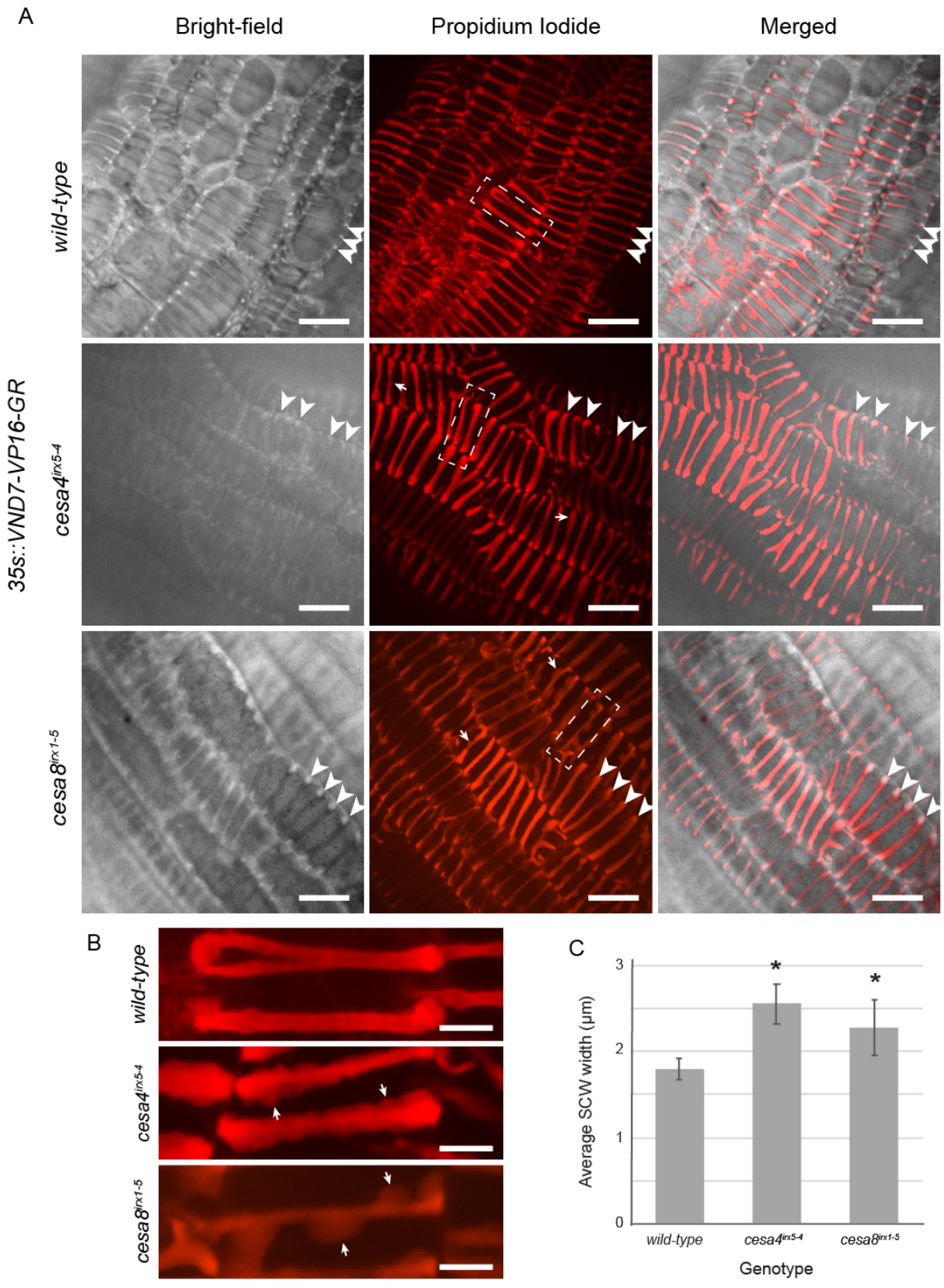

Figure 4-3: cesa4irx5-4 and cesa8irx1-5 mutants have thick aberrant secondary cell walls

(cont'd on next page)

(**A**) Z-projection images of 48-hour VND7-GR induced epidermal cells of 5-day old light-grown hypocotyls in *wild-type* (WT) and *cesa4*$^{irx5-4}$ and *cesa8*$^{irx1-5}$ knockout mutant backgrounds. SCWs are clearly visible with bright-field in all three genotypes (arrowheads). Propidium iodide staining reveals that in *cesa4*$^{irx5-4}$ and *cesa8*$^{irx1-5}$ mutants, SCWs have non-uniform SCWs commonly possessing bumps (arrows). (**B**) Zoom-ins of boxed areas in (A) highlights the bumps in SCW (arrows) seen in these mutants. (**C**) Average width of SCWs stained with PI. SCW widths were measured at the widest point for a SCW band. For each genotype 15 SCW bands were measured per cell in a total of 10 cells per genotype, from a total of 3 plants (n=10). (*) denotes significant difference from WT (Tukey's pairwise comparison, $P < 0.01$). Bars = SD. Scale bar = 20μm in (A), 5μm in (B).

4.2.3. All three *cesa* knockout mutants have normal patterned secondary cell wall deposition of xylan, but not cellulose

Given the differences in SCW structures between the SCW *cesas* knockout mutants, I next carried out more detailed phenotypic analyses of their cell wall components, specifically cellulose and the major SCW hemicellulose, xylan. The cellulose-specific stain, Pontamine fast Scarlet 4B (S4B) (Anderson *et al.* 2010; Liesche *et al.* 2013) and the anti-xylan antibody, LM10 (McCartney *et al.* 2005), were used in combination to visualize the patterning of these two SCW components (Schuetz *et al.* 2014). Both signals for cellulose and xylan were found in SCW domains in WT VND7-GR induced plants (Figure 4-4A). As this is a whole-mount immunostaining technique, xylan labelling is seen decorating the outer edges of SCWs, due to the inability of antibodies to penetrate deeper into the SCWs (arrows, Figure 4-4B). This decoration of the outer edges of SCWs with xylan signal is also apparent in *cesa4*$^{irx5-4}$ and *cesa8*$^{irx1-5}$ mutant backgrounds and to a lesser extent in *cesa7*$^{irx3-4}$ mutants (arrows, Figure 4-4B). Conversely, cellulose labelling is drastically altered in *cesa* mutants (Figure 4-4). Both *cesa4*$^{irx5-4}$ and *cesa8*$^{irx1-5}$, displayed banded cellulose signal but the sharp boundary between PCW and SCW seen in WT, was blurred because the two walls shared similar signal intensities (Figure 4-4B). Additionally, *cesa7*$^{irx3-4}$ mutants showed no banded patterns for cellulose deposition. Together, these data demonstrate that targeted secretion of xylan into SCW domains was normal in *cesa* mutants, but cellulose deposition was hindered in *cesa* mutants, and most severely in the *cesa7* mutant.

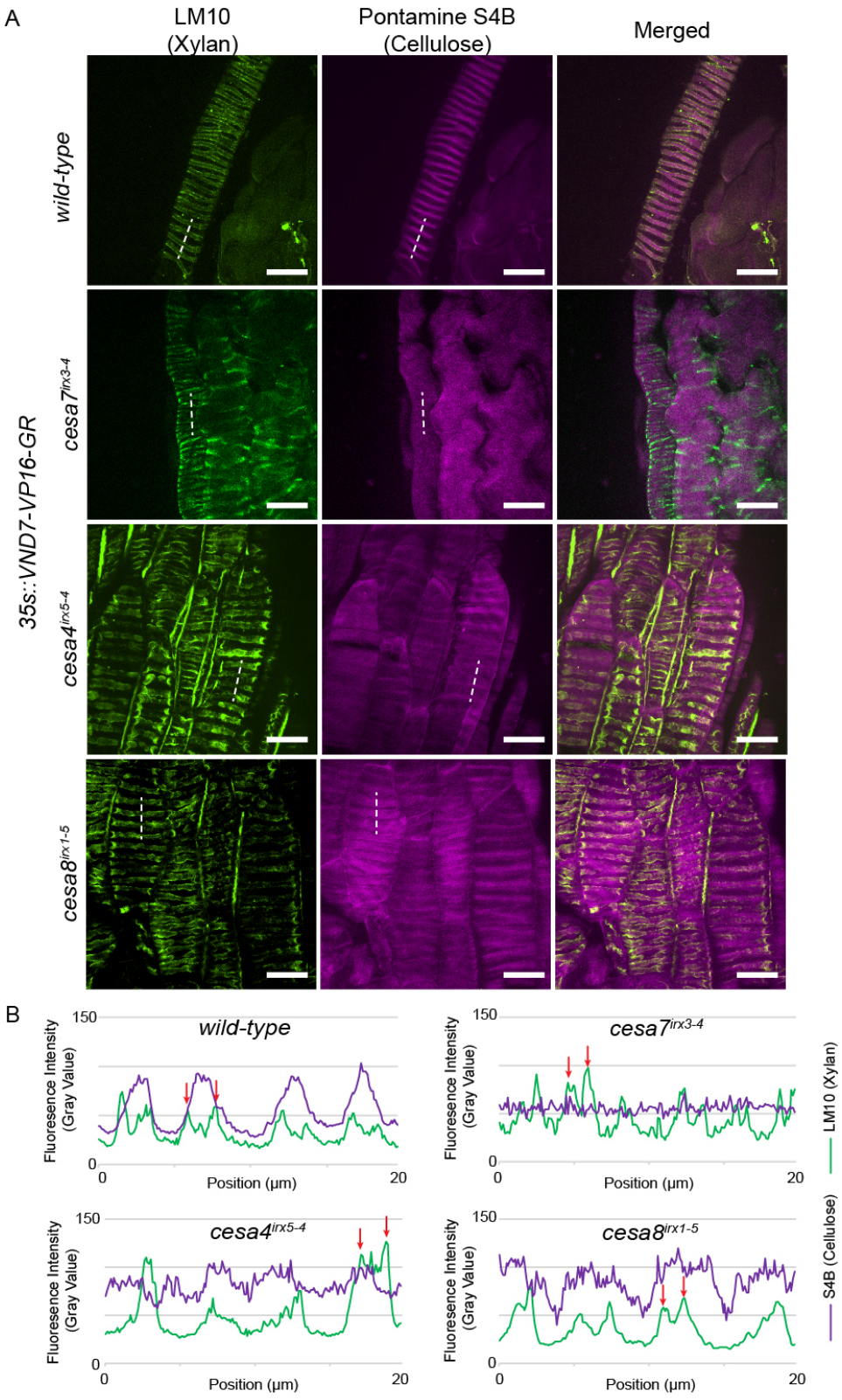

Figure 4-4: *cesa* mutants have banded patterns of xylan, but altered deposition of cellulose in secondary cell walls

(cont'd on next page)

(**A**) Z-projection images of 48-hour VND7-GR induced epidermal cells of 5-day old light-grown cotyledons, showing xylan and cellulose fluorescence in secondary cell walls in secondary cell wall *cesa* mutants. Xylan was labelled using whole-mount immunolocalization with LM10, while cellulose was stained using Pontamine fast Scarlet 4B (S4B). (**B**) Line scans of fluorescence intensities of areas marked by dashed-lines in (A). Double peaks of xylan signal surrounding a secondary cell wall are highlighted (arrows). Scale bar = 20μm.

4.2.4 Double mutants of *cesa* produce banded secondary cell wall patterns of cellulose and xylan

The observation of patterned SCW cellulose in *cesa4* and *cesa8* mutants, but not *cesa7* mutants, implies that SCW cellulose synthesis in the banded PM domains may still occur in the absence of CESA4 or CESA8 is missing, but not when CESA7 is missing. Conversely, it maybe that in *cesa7* mutants, cellulose synthesis maybe decoupled from MT guidance to SCWs. Support for this stems from our collaborators observations that in cell wall monosaccharide analysis of *cesa7*$^{bacl-1}$ knockout mutants, cellulose synthesis is still occurring after DEX induction despite the loss of CESA7. Given these possibilities, I next sought to determine what the phenotypic structure of SCWs would be when two of the SCW CESAs are missing. This analysis was performed in a *cesa7*$^{irx3-1}$*/cesa8*$^{irx1-1}$ double mutant line as several other mutant combinations did not successfully undergo VND7-GR induction. In *cesa7*$^{irx3-1}$*/cesa8*$^{irx1-1}$ double mutants, banded patterns of both xylan and cellulose were observed in VND7-GR induced cells (Figure 4-5A and B). These SCWs were also visible under bright-field (Figure 4-5C). These phenotypes are in contrast to the smooth SCWs observed in VND7-GR induced cells in the *cesa7*$^{irx3-1}$ and *cesa7*$^{irx3-4}$ single mutant backgrounds (Figure 4-2 and 4-4). This indicates that the non-banded cellulose deposition phenotype apparent in *cesa7* mutants is lost when another SCW CESA is perturbed.

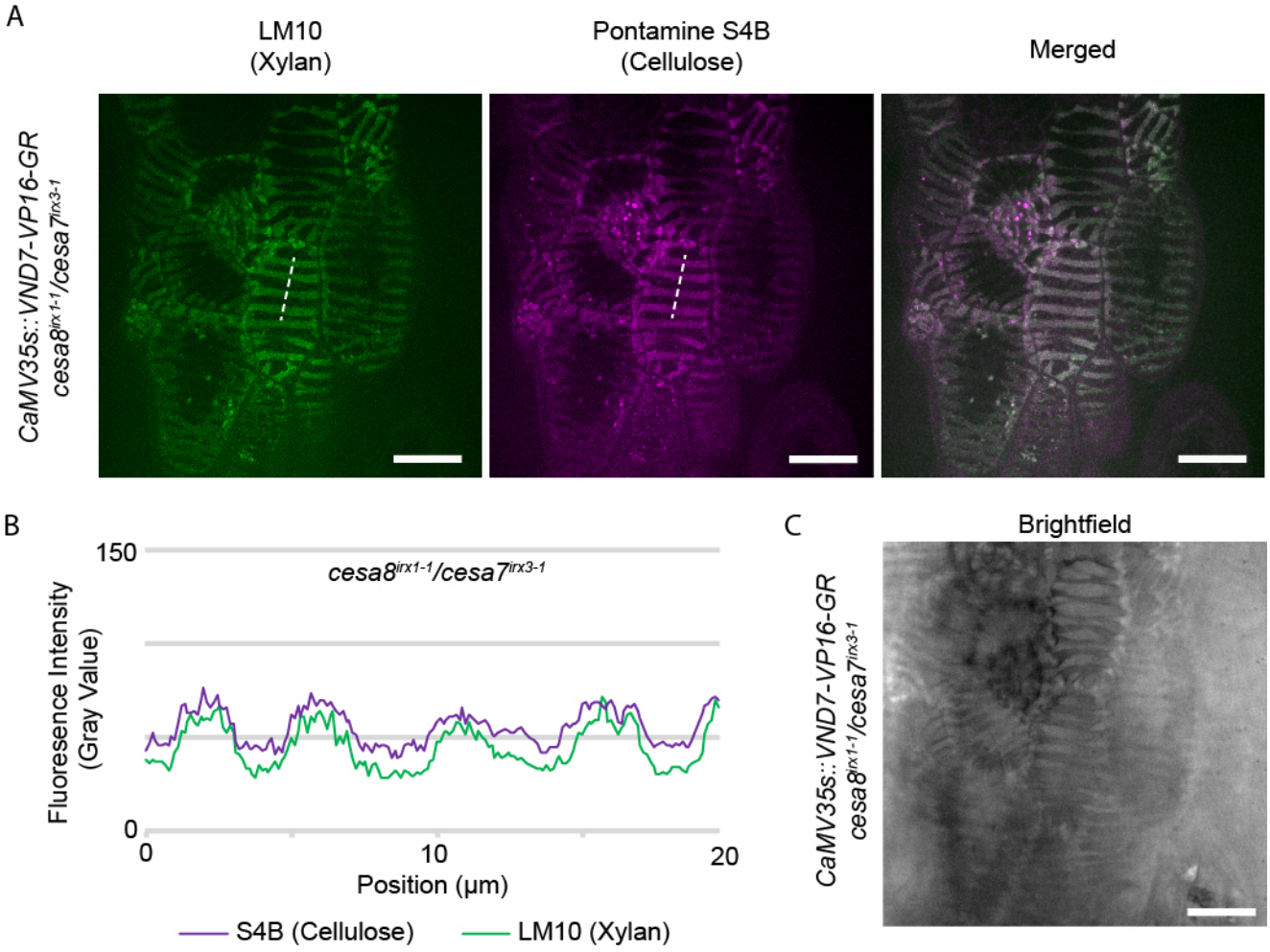

Figure 4-5: cesa7^{irx3-1}/cesa8^{irx1-1} double mutants have patterned xylan and cellulose in VND7-GR induced cells

(**A**) Z-projection images of 48-hour VND7-GR induced hypocotyl epidermal cells of 5-day old light-grown cotyledons, showing xylan and cellulose fluorescence in secondary cell walls of *cesa7^{irx3-1}/cesa8^{irx1-1}* double mutants. Xylan was labelled using whole-mount immunolocalization with LM10, while cellulose was stained using Pontamine fast Scarlet 4B (S4B). Scale bar = 20µm. (**B**) Line scans of fluorescence intensities of areas marked by dashed-lines in (A). (**C**) These secondary cell walls are visible even under bright-field. Scale bar = 20µm.

4.2.5 YFP-CESA7 is not delivered to the plasma membrane when CESA8 is missing

Given the presence of cellulose in bands in several SCW *cesa* mutants including *cesa7*$^{irx3\text{-}1}$*/cesa8*$^{irx1\text{-}1}$ double mutants, one can speculate that the remaining functional CESAs are localized at the PM and actively synthesizing cellulose. To test this, I next sought to determine the cellular localization of SCW CESAs when one of their partners is missing.

To do this, I transformed plants homozygous for *proCaMV35S::VND7-VP16-GR* and one of *cesa7*$^{irx3\text{-}4}$*, cesa8*$^{irx1\text{-}5}$ or *cesa4*$^{irx5\text{-}4}$ with fluorescently tagged versions of CESA4, CESA8, and CESA7 driven by their native promoter. Unfortunately, even after repeated attempts at generating transformants, it was difficult to recover plants with fluorescently tagged CESA, in homozygous mutant backgrounds, that would also reliably undergo VND7-GR induction. Only one set of plant lines was successfully isolated that meet the previously mentioned criteria: *YFP-CESA7/VND7-GR/cesa8*$^{irx1\text{-}5}$. These plants were imaged with spinning disk confocal and upon VND7-GR induction, YFP-CESA7 signal was present only within intracellular compartments, specifically Golgi (arrowheads) and SmaCCs (arrows), but not at the PM (Figure 4-6A) This localization did not change, even as the cells progressed close to program cell death.

One caveat to this finding was that in addition to the YFP-CESA7, these plants also contained a wild-type copy of CESA7, which may have been preferentially trafficked to the PM leaving the YFP-tagged CESA7 inside the cell. Ideally, this experiment would have been done in a double *cesa7*$^{irx3\text{-}4}$ *cesa8*$^{irx1\text{-}5}$ mutant to avoid this problem. However, crossing plants into the *cesa7* mutant background was challenging, because the mutant plants have impaired growth and development. In order to test if YFP-CESA7 still localized properly in a *wild-type CESA7* background, I transformed *wild-type* VND7-GR plants with the *proCESA7::YFP-CESA7* construct. Upon induction, YFP-CESA7 was seen in all the expected compartments including Golgi (arrowheads), SmaCCs (arrows) and PM with a SCW banded pattern (triangles) (Figure 4-6B).

This data thus implies that YFP-CESA7 cannot traffic properly to the PM when CESA8 is missing. Thus, it is likely that SCW CESAs cannot traffic properly to the PM when one of its interacting partners is missing.

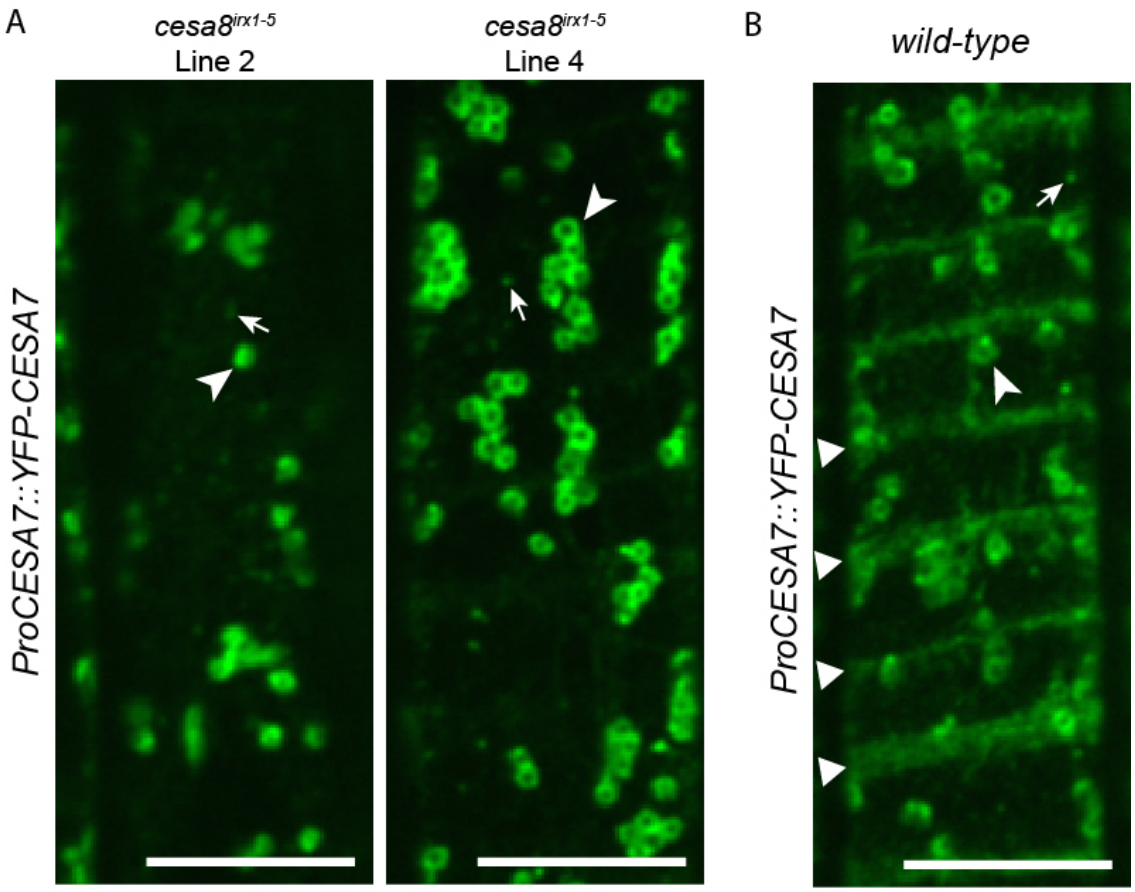

Figure 4-6: YFP-CESA7 in *cesa8*$^{irx1-5}$ background is stuck in the Golgi and SmaCCs
YFP-CESA7 localization in VND7-GR induced dark-grown hypocotyl cells in *cesa8*$^{irx1-5}$ (**A**) and *wild-type* (**B**) mutant backgrounds. (A) In multiple lines of *cesa8*$^{irx1-5}$, YFP-CESA7 is only seen in intracellular Golgi (arrowheads) and SmaCCs (arrows), and never at the plasma membrane indicating that the loss of CESA8 prevents proper trafficking of YFP-CESA7. (B) In *wild-type*, YFP-CESA7 localizes to Golgi (arrowheads), SmaCCs (arrows) and also the plasma membrane (triangles) indicating that YFP-CESA7 can function even in the presence of a *wild-type CESA7* allele. Scale bar = 20μm.

4.3 Discussion

The objective of this study was to characterize the phenotypic effects on the cell wall structure by the loss of an interacting CESA. The physiological effects of the loss of SCW CESAs has been well documented in several mutant screens (Taylor *et al.* 1999, 2000, 2003; Zhong *et al.* 2003). The alterations in the properties of the SCW in individual mutants have also been characterized (McDonnell et al., 2010). Additionally, the viability of null-mutant alleles of SCW *CESAs* has allowed for various analyses of CESA protein-protein interactions and the effects of the loss of a CESA to the stability of its partners (Taylor *et al.* 1999, 2003; Atanassov *et al.* 2009; Hill Jr. *et al.* 2014). However, due to the depth of these cells within tissue, it has been difficult to directly observe changes in SCW patterns or CESA dynamics within these mutants. With the VND7-GR system it is now possible to visualize changes in SCW patterning caused by the loss of CESA protein.

4.3.1 Patterned cellulose deposition still occurs within secondary cell wall *cesa* mutants

By crossing in the inducible VND7-GR induction system into the knock-out/null mutants of *cesa7*, *cesa4 and cesa8,* we show that all three mutants produced aberrant SCW structures, indicating that SCW formation was partially perturbed (Figure 4-2, Figure 4-3). Knock-out *cesa7* mutants do not form SCW cellulose bands in VND7-GR induced cells (Figure 4-4). Conversely, loss of either CESA8 or CESA4 resulted in normal patterning of cellulose, but this was accompanied by reduced cellulose staining compared to WT (Figure 4-4). The lack of banded SCW cellulose in *cesa7*$^{irx3\text{-}1}$ and *cesa7*$^{irx3\text{-}4}$ mutants is consistent with the observed phenotypes of *cesa7*$^{bacl\text{-}1}$ in which cellulose deposition still occurs but it is diffusely distributed across the cell instead of in bands. Given the patterned deposition of xylan (Figure 4-4), which follows the MT guided pathway of secreted polysaccharides (Zhu *et al.* 2015), it is most likely that MTs are bundled and banded in these mutants. As MTs target and guide CESAs to form SCW bands (Figure 2-7; Wightman and Turner 2008) partially through the CESA-microtubule linker, CSI1/POM2 (Schneider *et al.* 2017), it is possible that the loss of CESA7 results in the uncoupling of the CSCs from MT guidance. However, this is dependent on CESA4 and CESA8 forming a functional

complex, either by themselves or with the aid of a PCW CESA as a part of mixed complex (Carroll *et al.* 2012), to be able to carry out this MT-uncoupled deposition of cellulose.

Recent work has shown that the ectopic expression of only one *CESA* in a heterologous or recombinant system is sufficient for CESA complex formation and cellulose deposition *in vitro* (Cho *et al.* 2015; Purushotham *et al.* 2016). This supports a model in which aberrant complexes can still form when one of the CESAs is missing. Support for this is also shown here by the loss of SCW cellulose bands in *cesa7* single mutants but the presence of these bands in *cesa7*$^{irx3\text{-}1}$/*cesa8*$^{irx1\text{-}1}$ double mutants (Figure 4-5). This observation implies that the lack of banding seen in *cesa7* single mutants is dependent not only on the loss of *cesa7,* but on the presence of a functional CESA8. This could imply that CESA8, either by itself or with CESA4 or both CESA4 and a currently unidentified PCW CESA, can form a complex that is uncoupled from MTs. However, this is unlikely because CESAs are unstable without their interacting partners (Atanassov *et al.* 2009; Hill Jr. *et al.* 2014), and that CESAs do not appear to traffic properly without the presence of one of its interacting partner (Figure 4-6; Gardiner *et al.* 2003). Still, this hypothesis can be tested by introducing fluorescently tagged-SCW CESAs into the various *cesa* mutant backgrounds, which then could identify any mutants which still has CESAs being delivered to the PM and potentially part of an active complex.

4.3.2 Arrangement of xylan is perturbed in secondary cell wall *cesa* mutants

One of the most noticeable phenotypes was the rugged surface of the SCW bands seen in *cesa4* and *cesa8* mutants, and to a lesser extent *cesa7.* These "bumps" were clearly labelled with antibodies specific for xylan, indicating the presence of the secreted hemicellulose in these domains of the SCW. Additionally, although banded patterns of xylan deposition were observed, the label surrounding each SCW was unevenly distributed (Figure 4-4). These observations indicate that the xylan structure maybe disrupted when SCW cellulose deposition is severely affected. Models of xylan-cellulose interactions in SCWs point to portions of xylan chains aligning to the hydrophilic cellulose faces, with other xylan-containing domains unable interact with cellulose (Busse-Wicher

et al. 2014). Although the exact role for these interactions is currently not known, xylan plays a major role in SCW integrity, as evidenced by the *irregular xylem* (*irx*) phenotype of mutants lacking xylan (Zhong *et al.* 2005; Brown *et al.* 2009). Thus, it is likely that both xylan and cellulose depend on each other for proper organization within the SCW.

4.3.3 CESAs are localized in intracellular compartments when one of its partners are missing

Despite various mutant analyses being undertaken, studies on the cellular dynamics of CESAs when one of their interacting partners is missing have been limited. One study (Gardiner *et al.* 2003) used immunolocalization to show the loss of banding pattern of CESAs in native tracheary elements in SCW *cesa* mutant backgrounds. This is consistent with our observation of the loss of YFP-CESA7 at the PM underlying domains of SCW formation (Figure 4-6). Gardiner *et al.* (2003) also observed CESAs in what they interpreted as endoplasmic reticulum (ER) in mutant backgrounds. This lead the authors to conclude that complex formation must occur prior to ER exit (Gardiner *et al.* 2003). However, our data suggest complex formation occurs within the Golgi and not the ER, as we saw the accumulation of YFP-CESA7 in the Golgi (Figure 4-6). If complex formation did occur in the ER, and was a requirement for ER exit, one would then expect YFP-CESA7 to remain in the ER with the loss of CESA8. Support for complex assembly occurring in the Golgi is further supported by the identification of the STELLO proteins (Zhang *et al.* 2016). STELLO proteins are localized to the Golgi, and loss of STELLO results in fewer CESAs being incorporated into multimeric complexes, indicating that complex formation is hindered (Zhang *et al.* 2016). However, it may be possible that the earlier steps of CSC formation, specifically CESA dimerization, could occur in the ER, while higher ordered oligomerization occurs in Golgi (Atanassov *et al.* 2009). Such steps would not require the complete set of CESAs to be present and could therefore explain the discrepancy between the results.

The lack of PM localized YFP-CESA7 in *cesa8*$^{irx5\text{-}4}$ also implies that the cellulose seen in the various SCW *cesa* mutants is not produced from aberrant CSCs containing the remaining SCW CESAs. This is further supported by the observations that interactions

between PCW and SCW CESAs are generally weak (Carroll *et al.* 2012) and that CESAs appear to be unstable when one of their interacting partners is missing (Taylor *et al.* 2003; Atanassov *et al.* 2009; Hill Jr. *et al.* 2014). Thus, it is more likely that the cellulose seen in the SCWs of these mutants is generated by PCW CSCs that briefly synthesize cellulose in SCWs domains at the onset of trans-differentiation (Figure 4-7). Additionally, it may be possible that the PCW CSCs can contribute to SCW synthesis longer in SCW *cesa* mutants, given that plants have cell wall integrity feedback mechanisms that can change the composition and development of the cell wall in cellulose deficient mutants (Hématy and Höfte 2008). To test this, the constructs used in chapter 3, *proCESA6::tdT-CESA6/proCESA7::YFP-CESA7/VND7-GR* could be transformed into the lines generated in this chapter to examine how CESA dynamics of both PCW and SCW CESAs change together when a SCW CESA is missing.

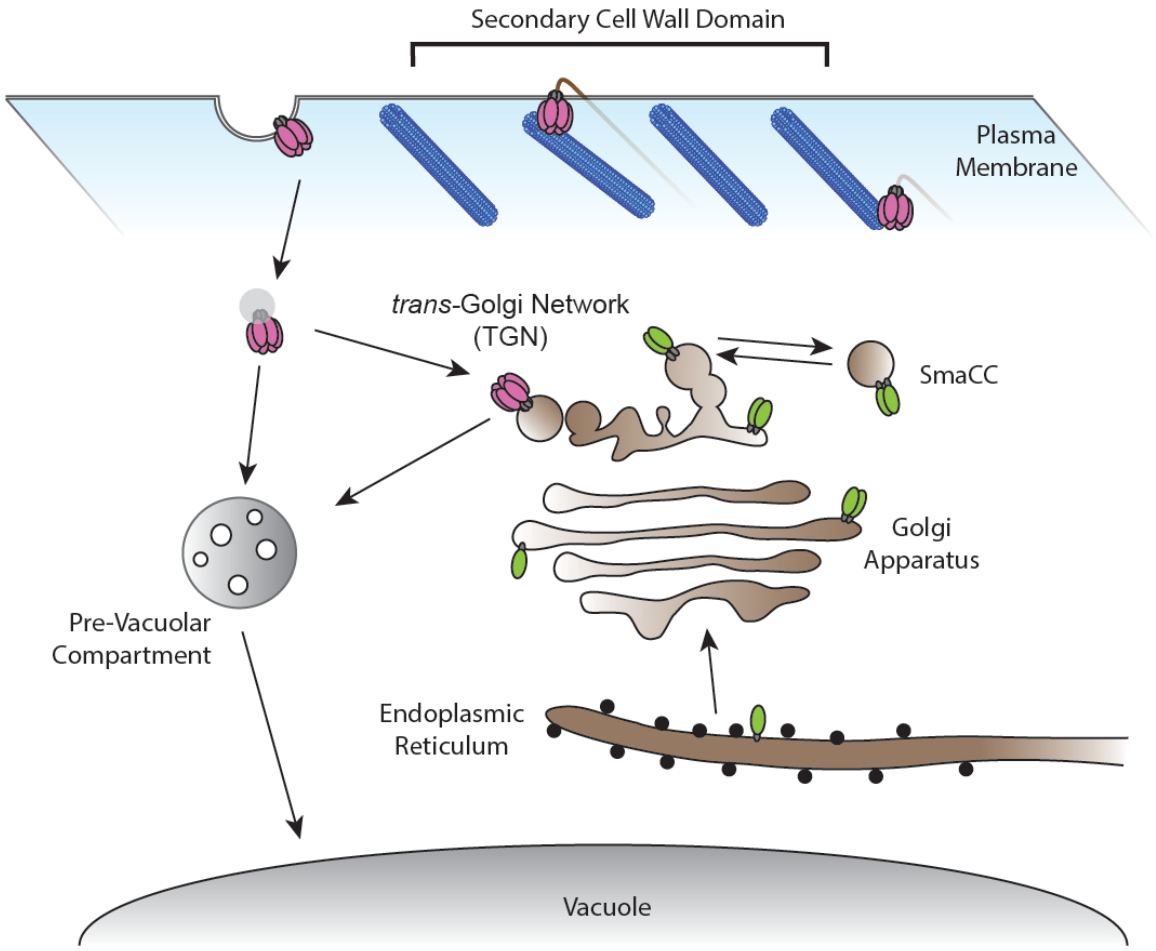

Figure 4-7: Secondary cell wall CSCs fail to be delivered to the plasma membrane when one of its CESAs is missing

When a secondary cell wall CESA (green) is missing, proper SCW CSC complexes fail to form. These incomplete and unstable CSCs fail to be delivered to the plasma membrane and remain within intracellular compartments such as Golgi and SmaCCs, and are possibly degraded. Primary cell wall CSCs (pink) briefly contribute to cellulose production in SCWs before being internalized and degraded in the lytic vacuole. This contribution may be larger in secondary cell wall *cesa* mutant backgrounds.

4.4 Materials and Methods

4.4.1 Generation of plant lines

To generate single *cesa* mutants containing VND7-GR, homozygous lines of *cesa7*$^{irx3-4}$, *cesa4*$^{irx5-4}$, and *cesa8*$^{irx1-5}$, single mutants were crossed with plant lines homozygous for *proCaMV35S::VND7-VP16-GR.* Homozygous F^{3}s lines were isolated and tested for induction. As F^{3}s and subsequent generations of lines containing *cesa7*$^{irx3-4}$/*VND7-GR*, were unreliable in their induction, *cesa7*$^{irx3-4}$ plants were instead transformed with a *proUBQ10::VND7-VP16:GR* construct that carried BASTA resistance (*cesa7*$^{irx3-4}$ is a SALK line that has Kanamycin resistance already, thus the original VND7-GR vector could not be used) a generous gift from Miranda Meents and T^{1}s and T^{2}s used for this analysis.

To generate double *cesa* mutants containing VND7-GR, homozygous lines of *cesa7*$^{irx3-1}$, *cesa4*$^{irx5-1}$, and *cesa8*$^{irx1-1}$ double mutants (in all three possible combinations) were generated by Sarah Barkwill, and were transformed with the VND7-GR induction construct. As *cesa4*$^{irx5-1}$ is a *Ds* transposable element mutant (Taylor *et al.* 2003) it already contains kanamycin resistance, thus the *proCaMV35S::VND7-VP16:GR* cannot be used due to it using a kanamycin selection marker in plants. Thus, for double mutants containing *cesa4*$^{irx5-1}$, a *proUBQ10::VND7-VP16:GR* construct made my co-worker, Miranda Meents, was used instead. For *cesa7*$^{irx3-1}$/ *cesa8*$^{irx1-1}$ double mutants the *proCaMV35S::VND7-VP16:GR* construct was used. Unfortunately, only lines of *cesa7*$^{irx3-1}$/ *cesa8*$^{irx1-1}$ were isolated that had good induction.

To generate lines containing fluorescently tagged CESAs, homozygous lines of *cesa4*$^{irx5-4}$*/VND7-GR* and *cesa8*$^{irx1-5}$*/VND7-GR* and *wild-type proCaMV35S::VND7-VP16:GR* were transformed with one of *proCESA7::YFP-CESA7* (from chapter 2), *proCESA4::GFP-CESA4,* and *proCESA8::mCherry-CESA8.* The latter two constructs were gracious gifts from our collaborator Joseph L Hill (unpublished). T^2 lines were isolated and screened for induction and fluorescent signal. Unfortunately, only lines of *cesa8*$^{irx1-5}$*/VND7-GR* and *wild-type proCaMV35S::VND7-VP16:GR* were isolated that had good induction and YFP-CESA7 present.

4.4.2 Growth and induction of samples

Seeds were surface sterilized with chlorine gas for 3 - 5 h. Seeds were sown on plates containing germination media (1× Murashige-Skoog [MS], 1% Sucrose, 1x Gamborg's Vitamin mix, 0.05% MES, 0.8% agar at pH 5.8) and placed at 4°C for 2 days. For samples where the SCW phenotype was to be observed, plates were moved into a growth chamber at 21°C in a flat position and grown under 24 h of light for 5 days. Plates were then removed from the chamber and under sterile conditions, 10 ml of 10 µM dexamethasone (Sigma) in sterilized 1/2 MS media was added to the plates for VND7-GR induction and left for 48 h to facilitate induction. For samples which were to be observed with live-cell imaging, plates were wrapped in aluminum foil and moved into a growth chamber at 21°C in a vertical position. Plates were then removed from the chamber and under sterile conditions, 10 ml of 10 µM dexamethasone (Sigma) in sterilized distilled deionized water was added to the plates for VND7-GR induction. Plates were then re-wrapped in aluminum foil and grown in the dark in a chamber for an additional 16 h (mid stages of SCW formation) before imaging.

4.4.3 Sample fixation and labelling

For samples where the secondary cell wall phenotype was to be observed, induced samples were fixed in 4% paraformaldehyde, 50 mM PIPES, 5 mM $MgSO_4$, and 5mM EGTA solution for 1 h. Seedlings were subsequently washed twice in TBST (10 mM Tris, pH 7, 0.25 M NaCl, 0.1% Tween 20) solution. Seedlings were subsequently washed and rehydrated in a graded ethanol series, and stored in TBST at 4°C until they were ready for use.

To stain cell walls, propidium iodide (PI) (Sigma) was used at a concentration of 10mg/mL of PI in water for 5 minutes. Samples were then washed twice with water and mounted.

For xylan and cellulose phenotyping, fixed seedlings were incubated in 5% bovine serum albumin (Sigma) in TBST for 1 - 2 h at room temperature, and subsequently

incubated with LM10 primary antibody (McCartney *et al.* 2005) at 1:50 dilution overnight at 4°C on a rotary shaker. Seedlings were rinsed three times in TBST solution for 5 min and were subsequently incubated in a 1:100 dilution of secondary anti-rat Alexa 488 antibody (Invitrogen) at room temperature for 1 h. After washing twice with TBST, samples were then stained using Pontamine fast Scarlet 4B (Sigma) by incubating seedlings in 10 mg per mL S4B solution in one-half-strength MS medium for 10 - 20 minutes and washing once in one-half-strength MS medium prior to imaging.

4.4.4 Imaging of fixed and live samples

Seedlings were mounted between glass slide and a #1.5 24×24 mm coverslips with water, and sealed with silicone vacuum grease. Imaging was performed on a spinning disk confocal set up (Leica DMi8 inverted microscope (Leica), Perkin-Elmer UltraView Yokogawa CSU-X1 spinning-disk system and a Hamamatsu 9100-13-CSU-X1 EMCCD Camera a 63X 1.34NA glycerol lens). Alexa Fluor 488 was imaged using a 488-nm laser and 510/30 emission filter, YFP was imaged using a 514-nm laser and 540/30 emission filter, while propidium iodide and Pontamine fast Scarlet 4B was detected with a 561-nm laser and 595/50-nm emission filter.

4.4.5 Image processing

Images were processed using the open-source Fiji software (Schindelin *et al.* 2012). Background correction was performed using the "subtract background" tool with a rolling ball radius of 50 pixels. For images of stained/labelled samples, Z-projections were made using Fiji using the "max-intensity values" for confocal images and "sum-slices" for bright-field images. Line scans were made of 20μm segments and the values exported into excel to generate the plot profiles.

Table 4-1: Primers employed in this study

Name	Primer Sequence (5' -> 3')	Purpose
irx 5-4.LP.AT5G44030	TCTTCCACCAAATCTTGTTGC	Genotyping *cesa4*$^{irx5-4}$ mutants
irx 5-4.RP.AT5G44030	GCTTCAAAGTCTTTCCCCAAC	Genotyping *cesa4*$^{irx5-4}$ mutants
irx3-4.LP.AT5G17420	AGAGAAGCTTAAGGAAACCGC	Genotyping *cesa7*$^{irx3-4}$ mutants
irx3-4.RP.AT5G17420	GAACAACACAAGAGCAGAGGG	Genotyping *cesa7*$^{irx3-4}$ mutants
irx1-5.LP.AT4G18780	AATCACAACCGAAAGCACATC	Genotyping *cesa8*$^{irx1-5}$ mutants
irx1-5.RP.AT4G18780	TTCCGATTTTTCACAATCCAC	Genotyping *cesa8*$^{irx1-5}$ mutants
VND7.At1G71930.P4	TCTTGGATGCTTCCCTGACT	Genotyping *VND7-GR*
GR.Rv	AGCAGGGTCATTTGGTCATC	Genotyping *VND7-GR*

Chapter 5: Conclusions

5.1 Major findings of this work

5.1.1 Perspective: why being second is a good thing

Over the past decade, a substantial amount of progress has been made in our understanding of the cellular dynamics of cellulose biosynthesis, and more specifically the CELLULOSE SYNTHASE (CESA) enzymes. This is largely due to advances in high-resolution live-cell imaging, which have been employed to track these enzymes, as they not only synthesize cellulose at the plasma membrane, but also undergo complex intracellular trafficking patterns that are almost unique when compared to other integral membrane proteins. For example, Paredez *et al.* (2006) is a seminal paper that demonstrated how CELLULOSE STYNTHASE complexes (CSCs) in the plasma membrane follow tracks of underlying cortical MTs, proving a 43-year-old hypothesis proposed by Ledbetter and Porter (1963). Since this landmark observation, the field has expanded immensely. It has become clear that CESA trafficking involves numerous continuous events of CESA delivery, endocytosis and recycling through various intracellular compartments. It is fair to state, that no other integral membrane protein has been shown to traffic so dynamically as CESAs. Why the need for such complexity in CESA trafficking is still a question that has yet to be addressed, but progress is being made. What is known however, is that this dynamic trafficking pattern somehow offers the cell a way to control the quality of cellulose produced. Thus, this area remains an intense topic of research.

One caveat to the wealth of knowledge generated on CESA trafficking, is that the majority of these studies have focused only on primary cell wall (PCW) synthesis. Moreover, the observations have been limited to one cell face of one cell type; specifically, the outer periclinal wall of epidermal cells of dark-grown hypocotyls. This of course, is due to the ease of imaging primary cell wall synthesis at this location. Since the majority of plant cells having thick cell walls and large vacuoles, the attenuation of signal in other cells is quite high when imaging even through a few cell layers. Thus, it has been

difficult to carry out live-cell imaging of CESAs in other cell types, especially those producing secondary cell wall (SCW), as SCW-rich cells occur deep within plant organs. Given that the majority of the world's cellulose is derived from secondary cell walls of woody tissues, and that the quality of cellulose within SCWs differ significantly from PCWs, it has become clear that similar studies using high-resolution of live-cell imaging are needed for SCWs. Only with this ability can certain questions about SCW formation can be addressed. These questions include: How similar are the cellular dynamics of PCW and SCW CESAs? What happens to PCW CESAs during the onset of SCW formation? Are the same sets of mechanisms controlling CSC localization in PCW and SCWs?

The development of an experimental system consisting of plants expressing a master transcription factor controlling xylem tracheary element cell fate, *VASCULAR-RELATED NAC DOMAIN7* (*VND7*) fused to an ectopic-inducible system (Yamaguchi *et al.* 2010), facilitated a means to bridge the gap between what is known about PCW and SCW CESAs. Since this system causes epidermal cells to undergo protoxylem tracheary element differentiation, including SCW synthesis, the dynamics of SCW CESAs can be observed with high-resolution live-cell imaging. In fact, this system has already been used successfully to study some of the underlying mechanisms controlling SCW formation, including localized deposition of the enzymes responsible for lignin polymerization (Schuetz *et al.* 2014), the role of tethering complexes involved in directing vesicles to SCW domains (Vukašinović *et al.* 2017), and the arrangement of MTs into specific patterns to control where SCW synthesis occurs (Oda and Fukuda 2012b). In this thesis, I have characterized the use of this system to study SCW CESA dynamics during the formation of xylem tracheary elements and used it to address some of the pressing questions about SCW CESAs, which have come as logical progression from the knowledge we have gained from studying PCW CESAs.

5.1.2 Summary of major findings of this thesis

Velocities of fluorescently-tagged CSCs at the plasma membrane have often been used as a proxy for the rate of cellulose synthesis in PCWs (Debolt *et al.* 2007; Fujita *et al.*

2011). Previous studies have attempted to measure these velocities in SCWs through indirect methods and have generated estimates well above any speeds observed in PCWs (Schneider and Herth 1986; Wightman *et al.* 2009). In Chapter 2, I directly measured velocities of SCW CSCs using the VND7-GR induction system in combination with high-resolution confocal microscopy. I showed that velocities of these SCW CSCs, though significantly faster than PCW CSCs under the same conditions, are within the ranges that have been reported for PCW CSCs. In the same study, density analysis revealed that SCW domains have a significantly higher density of CSCs than those observed during PCWs, thus it is likely a combination of both CSC velocity and density that results in the rapid formation of SCWs seen in xylem tracheary elements. I also confirmed that constriction of SCW CSCs to SCW domains of the PM is caused by the presence of underlying cortical MT bundles, as previously described (Wightman and Turner 2008), and showed that CSC velocity is unaffected by the loss of these MTs.

All cells that produce SCWs must first produce a PCW during cell expansion. As PCW and SCW synthesis requires two completely different sets of CESAs (Taylor *et al.* 2003; Persson *et al.* 2005, 2007; Desprez *et al.* 2007), what happens to the PCW CESAs during the transition to SCW synthesis is unknown. In Chapter 3, using the same VND7-GR induction system, I show that as SCW CESAs accumulate within intracellular compartments and are being delivered to the plasma membrane, PCW CESAs are removed from both the Golgi and plasma membrane and are trafficked to pre-vacuolar compartments. There is a brief period when both active PCW and SCW CESAs are found at the plasma membrane. However, upon further analysis, the two were found not to be within the same complex and the complexes labeled with either PCW and SCW CESA moved at distinct velocities. As development progresses, PCW CESAs are no longer present within any organelle expect for the lytic vacuole. This corresponds with a decrease in PCW CESA protein levels measured on Western blots, indicating that they are actively being degraded, and demonstrates that cells go through a complete change in cellulose synthesis machinery during the onset of SCW formation.

One of the advantages of working with SCW over PCW CESAs is that null mutants of SCW CESAs are viable (Taylor *et al.* 2003), unlike PCW CESAs (Persson *et al.* 2007). Viability of loss-of-function mutants, allows us to study the effects of the loss of one or more CESAs on cellulose production and cell wall structure. In chapter 4, using the VND7-GR system, I show the presence of phenotypic defects in SCW structure and patterning in SCW *cesa* mutants. In all single *cesa* knockout mutants, cellulose deposition was perturbed. The loss of wild-type cellulose within the SCW domains, appears to also cause perturbations in the patterning of the hemicellulose xylan, indicating that xylan and cellulose may depend on each other for proper organization in the SCW. Furthermore, *cesa7* mutants also lacked the observed SCW cellulose banding patterning. Although this is consistent with the phenotype of the newly isolated *cesa7*$^{bacl-1}$ mutant, this phenotype was lost in *cesa7*/*cesa8* double mutants. These observations support the possibility that when CESA7 is missing, CESA4 and CESA8 may be able to form aberrant CSCs that synthesize cellulose decoupled from MT guidance. However, given that CESAs are unstable when one of its interacting partners is lost (Taylor *et al.* 2003; Atanassov *et al.* 2009; Hill Jr. *et al.* 2014), and that I observed YFP-CESA7 being retained within intracellular compartments in a *cesa8* mutant background, the presence of aberrant and functional CSCs is unlikely, but cannot be ruled out.

5.2 Outstanding questions and future directions

I investigated the cellular dynamics of CESAs in developing xylem tracheary elements in an attempt to better understand how plants coordinate the cellulose synthesis machinery during SCW production and how this differs from the observations made in PCWs. Though several key observations were made, a large number of questions remain. In Chapter 2, the presence of a large number of SmaCCs during SCW formation emphasizes the need to further characterize the mechanisms of CSC delivery and recycling. In Chapter 3, the selective degradation of PCW CESAs during transition implies the involvement of a yet uncharacterized regulatory post-translation modification of CESAs. Finally, in Chapter 4, the surprising observation of multiple aberrant SCW

phenotypes in various SCW *cesa* mutants implies that the hypothesis that incomplete CSCs are non-functional may be not as strict as once thought. In this final section of this thesis, I propose several experiments that could address these questions and propose future areas of research focusing on SCW CESA dynamics.

5.2.1 Trafficking of CESAs and secreted cell wall polysaccharides

The presence of a large number of CESA containing vesicles called SmaCCs during SCW synthesis highlights the complexity and dynamic nature of CESA trafficking. These vesicles have been shown to be involved in the delivery of CESAs to the plasma membrane but it is not known whether these vesicles also contain secreted cell wall polysaccharides, such as xylan, which are made in the Golgi. This is primarily due to the inability to do live-cell imaging of secreted polysaccharides within a living cell and our inability to identify SmaCCs in transmission electron microscopy (TEM). To address this, one could introduce the VND7-inducible system into the secretory pathway deficient mutant such as *echidna (ech)*. Loss of the ECH protein results in perturbed secretion of cell wall polysaccharides and plasma membrane bound proteins (Gendre *et al.* 2013; McFarlane *et al.* 2013). More interestingly however, is the fact that protein and polysaccharide cargo appear to be mis-localized to distinct compartments, implying two independent pathways for protein and polysaccharide secretion. Mis-localization of CESAs in *ech* has not been tested, and it is reasonable to hypothesize that CESAs and cell polysaccharides would likely be trafficked together. If this is the case, one would expect to see both CESAs and xylan, an abundant secondary cell wall polysaccharide, to be mis-localized to same compartment in *ech* mutants. Additionally, using antibodies specific to xylan and SCW CESAs, immuno-transmission electron microscopy techniques can be used to identify the sub-cellular localization of these components in both WT and *ech* mutants. Such an experiment could therefore provide insight into how CESAs are trafficked from the Golgi to the plasma membrane.

5.2.2 Membrane environment surrounding CESAs

As CSCs represent a large complex that not only includes multiple copies of CESAs, but also other CESA interacting proteins, it has been hypothesized that CSCs must exist within membrane micro-domains to ensure complex stability (Guerriero *et al.* 2010; Lei *et al.* 2014b). Although there is limited direct evidence for distinct micro-environments in plants, detergent-resistant membranes isolated from both hybrid poplar and tobacco cell cultures did show some activity for cellulose synthesis (Bessueille *et al.* 2009; Cifuentes *et al.* 2010). In line with this, SCW CESAs have been shown to be acylated, which could affect the membrane environment around the complex (Kumar *et al.* 2016) These micro-domains surrounding CSCs may further be established by the CESA-MT linker CSI1/POM2 which contains a putative lipid binding domain (Lei *et al.* 2014b). Given these observations, is tempting to speculate that such membrane micro-domains could exist, especially in the plasma membrane underlying areas of SCW synthesis. To test this, membrane order could be measured *in vivo* using the fluorescent probe di-4-ANEPPDHQ (Frescatada-Rosa *et al.* 2014; Zhao *et al.* 2015). Additionally, sterols, which have been shown to be important for proper cellulose synthesis (Schrick *et al.* 2004) and are hypothesized to be enriched in lipid micro-domains, can be visualized using the sterol-binding probe filipin (Boutté *et al.* 2011). If these micro-domains do exist, one would expect that, given the high densities of CSCs, the lipid order in SCW domains would be significantly different from the domains between SCWs where no CSCs are found. Such micro-domains, may help explain the increased CSC velocities apparent in SCW synthesis, and at the same time open up questions about the role of membrane organization in CSC formation, activity and trafficking.

An important class of membrane lipids involved in trafficking are phosphatidyl inositol phosphates (PIPs). These lipids are involved in a large number of cellular processes, including establishing membrane identity of organelles and vesicles (Thole and Nielsen 2008). Thus, it is very likely PIPs, play an important role in CESA trafficking. Indeed, one of the *fragile fiber* mutants, *fra7*, was identified to be an allele of a PIP phosphatase, indicating a role for PIP during SCW synthesis (Zhong *et al.* 2005). As well, the inhibition

of certain PIP kinases via drug treatments has been shown to inhibit both the delivery and endocytosis of PCW CESAs (Fujimoto *et al.* 2015). However, it remains unclear whether these phenotypes are caused by a general block in the trafficking pathways that include CESAs. To address this knowledge gap, the VND7-GR system could be used in combination with biosensors that detect locations of specific forms of phosphorylated PIs (Vermeer *et al.* 2006, 2009; Simon *et al.* 2014). As CESA delivery, and endocytosis, only occurs within discrete domains during SCW formation, it is possible that this patterning would cause the enrichment of certain PIs to SCWs domains. Additionally, if these biosensors were used in tandem with a fluorescently tagged CESA, it would be possible to determine what PIPs mark SmaCCs, and potentially begin to elucidate the different populations of SmaCCs (*i.e.* the secretory and endocytic populations).

5.2.3 Selective targeting of primary cell wall CESAs for degradation

One of the key observations of this thesis is the selective targeting of PCW CESAs for degradation to the vacuole at the onset SCW formation. Previous work has shown CESA7 to be degraded via a proteasome pathway (Taylor 2007). Thus, it is tempting to speculate that PCW CESAs are degraded by the ubiquitin protease pathway during transition to SCW formation. Indeed, CESA6 was identified in a screen for ubiquitinated proteins (Manzano *et al.* 2008). Further, proteins involved in the ubiquitin proteasome pathway have been shown to be highly upregulated, including several E3 ubiquitin ligases (Yamaguchi et al., 2011). Given these observations, it is obvious that the transition stage in the VND7-GR system provides the perfect platform to study how CESAs go through the ubiquitin protease pathway. A simple but likely effective experiment would be to treat VND7-GR induced seedlings with a proteasome inhibitor such as MG132. If PCW CESAs are degraded via the ubiquitin protease pathway, treatment with MG132 would result in the vacuolar signal not appearing and retention of PCW CESAs in other intracellular compartments. Taking this further, one could use site directed mutagenesis on one of the fluorescently-tagged CESA constructs to generate CESAs that are ubiquitination deficient or mimic constitutive ubiquitination. These could then be tracked during transition to not

only test if ubiquitination is important for CESA degradation, but also how it affects CESA trafficking. Such a method has already been successfully employed to test how ubiquitination states affects PIN localization in cells (Leitner *et al.* 2012).

In addition to ubiquitination, CESAs have several predicted and highly conserved phosphorylation sites that may be the key signals to target certain CESAs. Phosphorylation of the PCW CESAs, CESA1 and CESA5, have already been shown to affect their catalytic activity (Chen *et al.* 2010; Bischoff *et al.* 2011; Sánchez-Rodríguez *et al.* 2017). As well, CESA7 has been shown to be phosphorylated *in vivo* (Taylor 2007). Interestingly, phosphorylated forms of CESA7 have also been shown to be the preferred substrates for proteasome degradation (Taylor 2007). Given these observations, it is tempting to hypothesize that phosphorylation may also be involved in marking CESAs for degradation. To test this, one could also use site-directed mutagenesis to generate constitutively phosphorylated or phosphorylation deficient versions of fluorescently-tagged CESAs and track the change in their localization under different conditions. Such a system has also been used to study the role of phosphorylation on the localization of PIN proteins (Michniewicz *et al.* 2007). However, it should be pointed out that PIN protein phosphorylation is believed to be more involved in recycling, while ubiquitination is involved in its degradation (Löfke *et al.* 2013). Given this and the results of Taylor (2007), there may be some form of interplay between phosphorylation and ubiquitination that has yet to be characterized.

Future work could also be carried out by identifying the kinases and/or E3 ligases that are responsible for causing PCW CESA degradation. Candidates can easily be identified using co-expression analysis of the available transcriptome data sets for VND7-GR induced samples. By identifying these candidates, the mechanisms of CESA internalization, trafficking and degradation could be further explored, which are all areas of great research interest but have been difficult to study due the complexity and dynamic nature of CESA trafficking.

5.2.4 Production of cellulose in secondary cell wall *cesa* mutants

The presence of different defects in cellulose ultrastructure and deposition patterning in the different SCW *cesa* mutants, indicates that CSCs may still function when one of its associated CESA is missing. Although unsuccessfully attempted in this thesis (except for YFP-CESA7 in the *cesa8* mutant), *cesa* knockout mutants could be transformed with fluorescently-tagged versions of their interacting partners and the localization of the CESAs determined. Plasma membrane signal in the form of slow-but steadily moving foci in these transformed mutants would strongly suggest the presence of active CSCs. As there is still a possibility for complexes containing both PCW and SCW CESAs (Carroll *et al.* 2012), fluorescently tagged PCW CESAs could be used to determine the extent of the SCW cellulose production that comes from PCW CSCs in SCW *cesa* mutant backgrounds.

Additionally, it would be interesting if one of the mutated forms of CESAs that either lacked or mimicked constitutive ubiquitination/phosphorylation (described in the previous section), produced a PCW CSC that not only avoided degradation, but also continued to be active through SCW synthesis. If possible, the ultrastructural properties of the produced cellulose may be different. A thorough characterization of the cellulose ultrastructure might answer this question and offer insights into the long-standing questions about the mechanisms controlling cellulose quality. Is there something inherit about each CESA class that leads to the differences in the ultrastructure of cellulose? Or are the differences dependent on the environment of the CESA and cellulose macromolecule (*i.e.* does the make-up of associated proteins, membranes and cell wall cause the differences in cellulose common to PCW and SCW)? Such information could provide paramount insight into the mechanisms controlling cellulose synthesis in plants.

References

Abas L, Benjamins R, Malenica N, *et al.* 2006. Intracellular trafficking and proteolysis of the Arabidopsis auxin-efflux facilitator PIN2 are involved in root gravitropism. *Nature Cell Biology* **8**: 249–256.

Abe H, Funada R. **2005**. The orientation of cellulose microfibrils in the cell walls of tracheids in conifers. *IAWA Journal* **26**: 161–174.

Ambrose C, Allard JF, Cytrynbaum EN, Wasteneys GO. **2011**. A CLASP-modulated cell edge barrier mechanism drives cell-wide cortical microtubule organization in Arabidopsis. *Nature Communications* **2**: 430.

Amor Y, Haigler CH, Johnson S, Wainscott M, Delmer DP. **1995**. A membrane-associated form of sucrose synthase and its potential role in synthesis of cellulose and callose in plants. *Proceedings of the National Academy of Sciences* **92**: 9353–9357.

Anderson CT, Carroll A, Akhmetova L, Somerville CR. **2010**. Real-Time Imaging of Cellulose Reorientation during Cell Wall Expansion in Arabidopsis Roots. *Plant Physiology* **152**: 787–796.

Aoyama T, Chua N-H. **1997**. A glucocorticoid-mediated transcriptional induction system in transgenic plants. *The Plant Journal* **11**: 605–612.

Arioli T, Peng L, Betzner AS, *et al.* 1998. Molecular Analysis of Cellulose Biosynthesis in Arabidopsis. *Science* **279**: 717–720.

Atanassov II, Pittman JK, Turner SR. **2009**. Elucidating the Mechanisms of Assembly and Subunit Interaction of the Cellulose Synthase Complex of Arabidopsis Secondary Cell Walls. *Journal of Biological Chemistry* **284**: 3833–3841.

Barnett JR, Bonham VA. **2004**. Cellulose microfibril angle in the cell wall of wood fibres. *Biological Reviews of the Cambridge Philosophical Society* **79**: 461–472.

Baroja-Fernandez E, Munoz FJ, Li J, *et al.* 2012. Sucrose synthase activity in the sus1/sus2/sus3/sus4 Arabidopsis mutant is sufficient to support normal cellulose and starch production. *Proceedings of the National Academy of Sciences* **109**: 321–326.

Barratt DHP, Derbyshire P, Findlay K, *et al.* 2009. Normal growth of Arabidopsis requires cytosolic invertase but not sucrose synthase. *Proceedings of the National Academy of Sciences* **106**: 13124–13129.

Bashline L, Li S, Anderson CT, Lei L, Gu Y. **2013**. The Endocytosis of Cellulose Synthase in Arabidopsis Is Dependent on 2, a Clathrin-Mediated Endocytosis Adaptin. *Plant Physiology* **163**: 150–160.

Bashline L, Li S, Gu Y. **2014**. The trafficking of the cellulose synthase complex in higher plants. *Annals of Botany* **114**: 1059–1067.

Bashline L, Li S, Zhu X, Gu Y. **2015**. The TWD40-2 protein and the AP2 complex cooperate in the clathrin-mediated endocytosis of cellulose synthase to regulate cellulose biosynthesis. *Proceedings of the National Academy of Sciences* **112**: 12870–12875.

Bessueille L, Sindt N, Guichardant M, Djerbi S, Teeri TT, Bulone V. **2009**. Plasma membrane microdomains from hybrid aspen cells are involved in cell wall polysaccharide biosynthesis. *The Biochemical Journal* **420**: 93–103.

Bischoff V, Desprez T, Mouille G, Vernhettes S, Gonneau M, Höfte H. **2011**. Phytochrome regulation of cellulose synthesis in Arabidopsis. *Current Biology* **21**: 1822–1827.

Boerjan W, Ralph J, Baucher M. **2003**. Lignin Biosynthesis. *Annual Review of Plant Biology* **54**: 519–546.

Bosca S, Barton CJ, Taylor NG, *et al.* 2006. Interactions between MUR10/CesA7-dependent secondary cellulose biosynthesis and primary cell wall structure. *Plant Physiology* **142**: 1353–1363.

Boutté Y, Men S, Grebe M. **2011**. Fluorescent in situ visualization of sterols in Arabidopsis roots. *Nature protocols* **6**: 446–456.

Brabham C, Stork J, Barrett M, DeBolt S. **2017**. Grass cell walls have a role in the inherent tolerance of grasses to the cellulose biosynthesis inhibitor isoxaben. *Pest Management Science* **12**: doi:10.1002/ps.4779.

Bringmann M, Li E, Sampathkumar A, Kocabek T, Hauser M-TM-T, Persson S. **2012**. POM-POM2/CELLULOSE SYNTHASE INTERACTING1 Is Essential for the Functional Association of Cellulose Synthase and Microtubules in Arabidopsis. *The Plant Cell* **24**: 163–177.

Browling AJ, Brown RM, Bowling AJ, Brown RM. **2008**. The cytoplasmic domain of the cellulose-synthesizing complex in vascular plants. *Protoplasma* **233**: 115–127.

Brown RM, Saxena IM. **2007**. *Cellulose: Molecular and Structural Biology* (RM Brown and IM Saxena, Eds.). Dordrecht: Springer Netherlands.

Brown RM, Saxena IM, Kudlicka K. **1996**. Cellulose biosynthesis in higher plants. *Trends in Plant Science* **1**: 149–156.

Brown DM, Zhang Z, Stephens E, Dupree P, Turner SR. **2009**. Characterization of IRX10 and IRX10-like reveals an essential role in glucuronoxylan biosynthesis in Arabidopsis.

The Plant Journal **57**: 732–746.

Busse-Wicher M, Gomes TCF, Tryfona T, *et al.* 2014. The pattern of xylan acetylation suggests xylan may interact with cellulose microfibrils as a twofold helical screw in the secondary plant cell wall of Arabidopsis thaliana. *The Plant Journal* **79**: 492–506.

Cano-Delgado A, Penfield S, Smith C, Catley M, Bevan M. **2003**. Reduced cellulose synthesis invokes lignification and defense responses in Arabidopsis thaliana. *The Plant Journal* **34**: 351–362.

Carroll A, Mansoori N, Li S, *et al.* 2012. Complexes with mixed primary and secondary cellulose synthases are functional in Arabidopsis plants. *Plant Physiology* **160**: 726–737.

Carroll A, Specht CDD. **2011**. Understanding Plant Cellulose Synthases through a Comprehensive Investigation of the Cellulose Synthase Family Sequences. *Frontiers in Plant Science* **2**: 1–11.

Cave ID. **1968**. The anisotropic elasticity of the plant cell wall. *Wood Science and Technology* **2**: 268–278.

Chen S, Ehrhardt DW, Somerville CR. **2010**. Mutations of cellulose synthase (CESA1) phosphorylation sites modulate anisotropic cell expansion and bidirectional mobility of cellulose synthase. *Proceedings of the National Academy of Sciences of the United States of America* **107**: 17188–17193.

Chen S, Jia H, Zhao H, *et al.* 2016. Anisotropic Cell Expansion Is Affected through the Bidirectional Mobility of Cellulose Synthase Complexes and Phosphorylation at Two Critical Residues on CESA3. *Plant Physiology* **171**: 242–250.

Cho SH, Du J, Sines I, *et al.* 2015. In vitro synthesis of cellulose microfibrils by a membrane protein from protoplasts of the non-vascular plant Physcomitrella patens. *Biochemical Journal* **470**: 195–205.

Cifuentes C, Bulone V, Emons AMC. **2010**. Biosynthesis of Callose and Cellulose by Detergent Extracts of Tobacco Cell Membranes and Quantification of the Polymers Synthesized in vitro. *Journal of Integrative Plant Biology* **52**: 221–233.

Coleman HD, Ellis DD, Gilbert M, Mansfield SD. **2006**. Up-regulation of sucrose synthase and UDP-glucose pyrophosphorylase impacts plant growth and metabolism. *Plant Biotechnology Journal* **4**: 87–101.

Coleman HD, Yan J, Mansfield SD. **2009**. Sucrose synthase affects carbon partitioning to increase cellulose production and altered cell wall ultrastructure. *Proceedings of the National Academy of Sciences* **106**: 13118–13123.

Cosgrove DJ. **2005**. Growth of the plant cell wall. *Nature Reviews Molecular Cell Biology*

6: 850–861.

Crowell EF, Bischoff V, Desprez T, *et al.* 2009. Pausing of Golgi Bodies on Microtubules Regulates Secretion of Cellulose Synthase Complexes in Arabidopsis. *The Plant Cell* **21**: 1141–1154.

DeBolt S, Gutierrez R, Ehrhardt DW, *et al.* 2007. Morlin, an inhibitor of cortical microtubule dynamics and cellulose synthase movement. *Proceedings of the National Academy of Sciences* **104**: 5854–5859.

Debolt S, Gutierrez R, Ehrhardt DW, Somerville CR. **2007**. Nonmotile Cellulose Synthase Subunits Repeatedly Accumulate within Localized Regions at the Plasma Membrane in Arabidopsis Hypocotyl Cells following 2,6-Dichlorobenzonitrile Treatment. *Plant Physiology* **145**: 334–338.

Delmer DP. **1999**. Cellulose Biosynthesis: Exciting Times for A Difficult Field of Study. *Annual Review of Plant Physiology and Plant Molecular Biology* **50**: 245–276.

Derbyshire P, Ménard D, Green P, *et al.* 2015. Proteomic Analysis of Microtubule Interacting Proteins over the Course of Xylem Tracheary Element Formation in Arabidopsis. *The Plant Cell* **27**: 2709–2726.

Desprez T, Juraniec M, Crowell EFEF, *et al.* 2007. Organization of cellulose synthase complexes involved in primary cell wall synthesis in Arabidopsis thaliana. *Proceedings of the National Academy of Sciences* **104**: 15572–15577.

Desprez T, Vernhettes S, Fagard M, *et al.* 2002. Resistance against Herbicide Isoxaben and Cellulose Deficiency Caused by Distinct Mutations in Same Cellulose Synthase Isoform CESA6. *Plant Physiology* **128**: 482–490.

Diotallevi F, Mulder B. **2007**. The Cellulose Synthase Complex: A Polymerization Driven Supramolecular Motor. *Biophysical Journal* **92**: 2666–2673.

Doblin MS, Kurek I, Jacob-Wilk D, Delmer DP. **2002**. Cellulose Biosynthesis in Plants: from Genes to Rosettes. *Plant and Cell Physiology* **43**: 1407–1420.

Doblin MS, Pettolino F, Bacic A. **2010**. Plant cell walls: the skeleton of the plant world. *Functional Plant Biology* **37**: 357–381.

Endler A, Kesten C, Schneider R, *et al.* 2015. A Mechanism for Sustained Cellulose Synthesis during Salt Stress. *Cell* **162**: 1353–1364.

Endo S, Pesquet E, Yamaguchi M, *et al.* 2009. Identifying new components participating in the secondary cell wall formation of vessel elements in zinnia and Arabidopsis. *The Plant Cell* **21**: 1155–1165.

Esau K. **1977**. *Anatomy of Seed Plants*. New York: Wiley.

Fagard M, Desnos T, Desprez T, *et al.* 2000. PROCUSTE1 Encodes a Cellulose Synthase Required for Normal Cell Elongation Specifically in Roots and Dark-Grown Hypocotyls of Arabidopsis. *The Plant Cell* **12**: 2409–2424.

Fernandes AN, Thomas LH, Altaner CM, *et al.* 2011. Nanostructure of cellulose microfibrils in spruce wood. *Proceedings of the National Academy of Sciences* **108**: E1195–E1203.

Fisher DD, Cyr RJ. **1998**. Extending the Microtubule/Microfibril Paradigm. *Plant Physiology* **116**: 1043–1051.

Frescatada-Rosa M, Stanislas T, Backues SK, *et al.* 2014. High lipid order of Arabidopsis cell-plate membranes mediated by sterol and DYNAMIN-RELATED PROTEIN1A function. *The Plant Journal* **80**: 745–757.

Fujimoto M, Suda Y, Vernhettes S, Nakano A, Ueda T. **2015**. Phosphatidylinositol 3-Kinase and 4-Kinase Have Distinct Roles in Intracellular Trafficking of Cellulose Synthase Complexes in Arabidopsis thaliana. *Plant and Cell Physiology* **56**: 287–298.

Fujita M, Himmelspach R, Hocart CH, Williamson RE, Mansfield SD, Wasteneys GO. **2011**. Cortical microtubules optimize cell-wall crystallinity to drive unidirectional growth in Arabidopsis. *The Plant Journal* **66**: 915–928.

Gardiner JC, Taylor NG, Turner SR. **2003**. Control of cellulose synthase complex localization in developing xylem. *The Plant Cell* **15**: 1740–1748.

Gendre D, McFarlane HE, Johnson E, *et al.* 2013. Trans-Golgi network localized ECHIDNA/Ypt interacting protein complex is required for the secretion of cell wall polysaccharides in Arabidopsis. *The Plant Cell* **25**: 2633–2646.

Giddings TH, Brower DL, Staehelin LA. **1980**. Visualization of particle complexes in the plasma membrane of Micrasterias denticulata associated with the formation of cellulose fibrils in primary and secondary cell walls. *The Journal of Cell Biology* **84**: 327–339.

Gonneau M, Desprez T, Guillot A, Vernhettes S, Hofte H. **2014**. Catalytic Subunit Stoichiometry within the Cellulose Synthase Complex. *Plant Physiology* **166**: 1709–1712.

Grefen C, Donald N, Hashimoto K, Kudla J, Schumacher K, Blatt MR. **2010**. A ubiquitin-10 promoter-based vector set for fluorescent protein tagging facilitates temporal stability and native protein distribution in transient and stable expression studies. *The Plant Journal* **64**: 355–365.

Gu Y, Kaplinsky N, Bringmann M, *et al.* 2010. Identification of a cellulose synthase-associated protein required for cellulose biosynthesis. *Proceedings of the National*

Academy of Sciences **107**: 12866–12871.

Guerriero G, Fugelstad J, Bulone V. **2010**. What Do We Really Know about Cellulose Biosynthesis in Higher Plants? *Journal of Integrative Plant Biology* **52**: 161–175.

Gutierrez R, Lindeboom JJ, Paredez AR, Emons AMC, Ehrhardt DW. **2009**. Arabidopsis cortical microtubules position cellulose synthase delivery to the plasma membrane and interact with cellulose synthase trafficking compartments. *Nature Cell Biology* **11**: 797–806.

Haigler CH, Brown RM. **1986**. Transport of rosettes from the golgi apparatus to the plasma membrane in isolated mesophyll cells of Zinnia elegans. *Protoplasma* **134**: 111–120.

Haigler CH, Ivanova-Datcheva M, Hogan PS, *et al.* 2001. Carbon partitioning to cellulose synthesis. *Plant Molecular Biology* **47**: 29–51.

Harada H, Côté WA. **1985**. Structure of Wood In: Higuchi T, ed. *Biosynthesis and Biodegradation of Wood Components*. Orlando: Academic Press, 1–41.

Harholt J, Suttangkakul A, Scheller HV. **2010**. Biosynthesis of Pectin. *Plant Physiology* **153**: 384–395.

Heilmann M, Heilmann I. **2015**. Plant phosphoinositides - Complex networks controlling growth and adaptation. *Biochimica et Biophysica Acta - Molecular and Cell Biology of Lipids* **1851**: 759–769.

Helariutta Y, Fukaki H, Wysocka-Diller J, *et al.* 2000. The SHORT-ROOT Gene Controls Radial Patterning of the Arabidopsis Root through Radial Signaling. *Cell* **101**: 555–567.

Hématy K, Höfte H. **2008**. Novel receptor kinases involved in growth regulation. *Current Opinion in Plant Biology* **11**: 321–328.

Hepler PK, Fosket DE. **1971**. The role of microtubules in vessel member differentiation in Coleus. *Protoplasma* **72**: 213–236.

Herth W. **1980**. Calcofluor white and Congo red inhibit chitin microfibril assembly of Poterioochromonas: evidence for a gap between polymerization and microfibril formation. *The Journal of Cell Biology* **87**: 442–450.

Herth W. **1985**. Plasma-membrane rosettes involved in localized wall thickening during xylem vessel formation of Lepidium sativum L. *Planta* **164**: 12–21.

Hill Jr. JL, Hammudi MB, Tien M, Hill JLJ, Hammudi MB, Tien M. **2014**. The Arabidopsis Cellulose Synthase Complex: A Proposed Hexamer of CESA Trimers in an Equimolar Stoichiometry. *The Plant Cell* **26**: 4834–4842.

Hon DNS. **1994**. Cellulose: a random walk along its historical path. *Cellulose* **1**: 1–25.

Jacob-Wilk D, Kurek I, Hogan P, Delmer DP. **2006**. The cotton fiber zinc-binding domain of cellulose synthase A1 from Gossypium hirsutum displays rapid turnover in vitro and in vivo. *Proceedings of the National Academy of Sciences* **103**: 12191–12196.

Joshi CP, Mansfield SD. **2007**. The cellulose paradox — simple molecule, complex biosynthesis. *Current Opinion in Plant Biology* **10**: 220–226.

Kang B-HH, Nielsen E, Preuss ML, *et al.* 2011. Electron Tomography of RabA4b- and PI-4K-1-Labeled Trans Golgi Network Compartments in Arabidopsis. *Traffic* **12**: 313–329.

Kasai K, Takano J, Miwa K, Toyoda A, Fujiwara T. **2011**. High boron-induced ubiquitination regulates vacuolar sorting of the BOR1 borate transporter in Arabidopsis thaliana. *Journal of Biological Chemistry* **286**: 6175–6183.

Kerr T, Bailey IW. **1934**. The Cambium and It's Derivative Tissues: No. X Structure, Optical Properties and Chemical Composition of the So-called Middle Lamella. *Journal of the Arnold Arboretum* **15**: 327–349.

Kim SH, Lee CM, Kafle K. **2013**. Characterization of crystalline cellulose in biomass: Basic principles, applications, and limitations of XRD, NMR, IR, Raman, and SFG. *Korean Journal of Chemical Engineering* **30**: 2127–2141.

Kimura S, Laosinchai W, Itoh T, Cui X, Linder CR, Brown RM. **1999**. Immunogold labeling of rosette terminal cellulose-synthesizing complexes in the vascular plant vigna angularis. *The Plant Cell* **11**: 2075–2086.

Kirik A, Ehrhardt DW, Kirik V. **2012**. TONNEAU2/FASS Regulates the Geometry of Microtubule Nucleation and Cortical Array Organization in Interphase Arabidopsis Cells. *The Plant Cell* **24**: 1158–1170.

Kobayashi H, Fukuda H, Shibaoka H. **1988**. Interrelation between the spatial disposition of actin filaments and microtubules during the differentiation of tracheary elements in culturedZinnia cells. *Protoplasma* **143**: 29–37.

Korbei B, Luschnig C. **2013**. Plasma membrane protein ubiquitylation and degradation as determinants of positional growth in plants. *Journal of Integrative Plant Biology* **55**: 809–823.

Krishnamoorthy P, Sánchez-Rodríguez C, Heilmann I, Persson S. **2014**. Regulatory roles of phosphoinositides in membrane trafficking and their potential impact on cell-wall synthesis and re-modelling. *Annals of Botany* **114**: 1049–1057.

Kubo M, Udagawa M, Nishikubo N, *et al.* 2005. Transcription switches for protoxylem and metaxylem vessel formation. *Genes & Development* **19**: 1855–1860.

Kumar M, Atanassov II, Turner SR. **2017**. Functional Analysis of Cellulose Synthase (CESA) Protein Class Specificity. *Plant Physiology* **173**: 970–983.

Kumar M, Wightman R, Atanassov I, *et al.* 2016. S-Acylation of the cellulose synthase complex is essential for its plasma membrane localization. *Science* **353**: 166–169.

Lane DR, Wiedemeier A, Peng L, *et al.* 2001. Temperature-Sensitive Alleles of RSW2 Link the KORRIGAN Endo-1,4-β-Glucanase to Cellulose Synthesis and Cytokinesis in Arabidopsis. *Plant Physiology* **126**: 278–288.

Ledbetter MCC, Porter KRR. **1963**. A "MICROTUBULE" IN PLANT CELL FINE STRUCTURE. *The Journal of Cell Biology* **19**: 239–250.

Lei L, Li S, Bashline L, Gu Y. **2014**. Dissecting the molecular mechanism underlying the intimate relationship between cellulose microfibrils and cortical microtubules. *Frontiers in Plant Science* **5**: 1–8.

Lei L, Li S, Du J, Bashline L, Gu Y. **2013**. CELLULOSE SYNTHASE INTERACTIVE3 Regulates Cellulose Biosynthesis in Both a Microtubule-Dependent and Microtubule-Independent Manner in Arabidopsis. *The Plant Cell* **25**: 4912–4923.

Lei L, Li S, Gu Y. **2012**. Cellulose synthase interactive protein 1 (CSI1) mediates the intimate relationship between cellulose microfibrils and cortical microtubules. *Plant Signaling & Behavior* **7**: 714–718.

Leitner J, Petrasek J, Tomanov K, *et al.* 2012. Lysine63-linked ubiquitylation of PIN2 auxin carrier protein governs hormonally controlled adaptation of Arabidopsis root growth. *Proceedings of the National Academy of Sciences* **109**: 8322–8327.

Li S, Bashline L, Zheng Y, *et al.* 2016. Cellulose synthase complexes act in a concerted fashion to synthesize highly aggregated cellulose in secondary cell walls of plants. *Proceedings of the National Academy of Sciences* **113**: 11348–11353.

Li S, Chen M, Yu D, *et al.* 2013. EXO70A1-Mediated Vesicle Trafficking Is Critical for Tracheary Element Development in Arabidopsis. *The Plant Cell* **25**: 1774–1786.

Li Z, Fernie AR, Persson S. **2016a**. Transition of primary to secondary cell wall synthesis. *Science Bulletin* **61**: 838–846.

Li S, Lei L, Somerville CR, Gu Y. **2012**. Cellulose synthase interactive protein 1 (CSI1) links microtubules and cellulose synthase complexes. *Proceedings of the National Academy of Sciences* **109**: 185–190.

Li Z, Omranian N, Neumetzler L, *et al.* 2016b. A Transcriptional and Metabolic Framework for Secondary Wall Formation in Arabidopsis. *Plant Physiology* **172**: 1334–1351.

Li Y, Qian Q, Zhou Y, *et al.* 2003. BRITTLE CULM1, Which Encodes a COBRA-Like Protein, Affects the Mechanical Properties of Rice Plants. *The Plant Cell* **15**: 2020–2031.

Liesche J, Ziomkiewicz I, Schulz A. **2013**. Super-resolution imaging with Pontamine Fast Scarlet 4BS enables direct visualization of cellulose orientation and cell connection architecture in onion epidermis cells. *BMC Plant Biology* **13**.

Liu Z, Schneider RR, Kesten C, *et al.* 2016. Cellulose-Microtubule Uncoupling Proteins Prevent Lateral Displacement of Microtubules during Cellulose Synthesis in Arabidopsis. *Developmental Cell* **38**: 305–315.

Liu L, Shang-Guan K, Zhang B, *et al.* 2013. Brittle Culm1, a COBRA-Like Protein, Functions in Cellulose Assembly through Binding Cellulose Microfibrils (L-J Qu, Ed.). *PLoS Genetics* **9**: e1003704-15.

Löfke C, Luschnig C, Kleine-Vehn J. **2013**. Posttranslational modification and trafficking of PIN auxin efflux carriers. *Mechanisms of Development* **130**: 82–94.

Maloney VJ, Mansfield SD. **2010**. Characterization and varied expression of a membrane-bound endo-β-1,4-glucanase in hybrid poplar. *Plant Biotechnology Journal* **8**: 294–307.

Maloney VJ, Samuels AL, Mansfield SD. **2011**. The endo-1,4-β-glucanase Korrigan exhibits functional conservation between gymnosperms and angiosperms and is required for proper cell wall formation in gymnosperms. *New Phytologist* **193**: 1076–1087.

Manders EMM, Verbeek FJ, Aten JA. **1993**. Measurement of co-localization of objects in dual-colour confocal images. *Journal of Microscopy* **169**: 375–382.

Mansoori N, Timmers J, Desprez T, *et al.* 2014. KORRIGAN1 Interacts Specifically with Integral Components of the Cellulose Synthase Machinery (TI Baskin, Ed.). *PLoS ONE* **9**: e112387.

Manzano C, Abraham Z, López-Torrejón G, Del Pozo JC. **2008**. Identification of ubiquitinated proteins in Arabidopsis. *Plant Molecular Biology* **68**: 145–158.

McCartney L, Marcus SE, Knox JP. **2005**. Monoclonal antibodies to plant cell wall xylans and arabinoxylans. *Journal of Histochemistry and Cytochemistry* **53**: 543–546.

McDonnell LM. **2010**. Investigating the Role of Cellulose Synthases in the Biosynthesis and Properties of Cellulose in Secondary Cell Walls. *University of British Columbia*.

McFarlane HE, Döring A, Persson S. **2014**. The Cell Biology of Cellulose Synthesis. *Annual Review of Plant Biology* **65**: 69–94.

McFarlane HE, Watanabe Y, Gendre D, *et al.* 2013. Cell Wall Polysaccharides are Mislocalized to the Vacuole in echidna Mutants. *Plant and Cell Physiology* **54**: 1867–1880.

McNeil M, Darvill AG, Fry SC, Albersheim P. **1984**. Structure and function of the primary cell walls of plants. *Annual Review of Biochemistry* **53**: 625–663.

Meijering E, Dzyubachyk O, Smal I. **2012**. Methods for cell and particle tracking. *Methods Enzymology* **504**: 183–200.

Men S, Boutté Y, Ikeda Y, *et al.* 2008. Sterol-dependent endocytosis mediates post-cytokinetic acquisition of PIN2 auxin efflux carrier polarity. *Nature Cell Biology* **10**: 237–244.

Mendu V, Griffiths JS, Persson S, *et al.* 2011. Subfunctionalization of Cellulose Synthases in Seed Coat Epidermal Cells Mediates Secondary Radial Wall Synthesis and Mucilage Attachment. *Plant Physiology* **157**: 441–453.

Miart F, Desprez T, Biot E, *et al.* 2014. Spatio-temporal analysis of cellulose synthesis during cell plate formation in Arabidopsis. *The Plant Journal* **77**: 71–84.

Michniewicz M, Zago MK, Abas L, *et al.* 2007. Antagonistic Regulation of PIN Phosphorylation by PP2A and PINOID Directs Auxin Flux. *Cell* **130**: 1044–1056.

Morgan JLW, Strumillo J, Zimmer J. **2013**. Crystallographic snapshot of cellulose synthesis and membrane translocation. *Nature* **493**: 181–186.

Mueller SC, Brown RM. **1980**. Evidence for an intramembrane component associated with a cellulose microfibril-synthesizing complex in higher plants. *Journal of Cell Biology* **84**: 315–326.

Newman RH, Hill SJ, Harris PJ. **2013**. Wide-Angle X-Ray Scattering and Solid-State Nuclear Magnetic Resonance Data Combined to Test Models for Cellulose Microfibrils in Mung Bean Cell Walls. *Plant Physiology* **163**: 1558–1567.

Nicol F, His I, Jauneau A, Vernhettes S, Canut H, Höfte H. **1998**. A plasma membrane-bound putative endo-1, 4-β-d-glucanase is required for normal wall assembly and cell elongation in Arabidopsis. *The EMBO journal* **17**: 5563–5576.

Nishiyama Y. **2009**. Structure and properties of the cellulose microfibril. *Journal of Wood Science* **55**: 241–249.

Nixon BT, Mansouri K, Singh A, *et al.* 2016. Comparative Structural and Computational Analysis Supports Eighteen Cellulose Synthases in the Plant Cellulose Synthesis Complex. *Scientific Reports* **6**: 28696.

Oda Y, Fukuda H. **2012a**. Secondary cell wall patterning during xylem differentiation. *Current Opinion in Plant Biology* **15**: 38–44.

Oda Y, Fukuda H. **2012b**. Initiation of Cell Wall Pattern by a Rho- and Microtubule-Driven Symmetry Breaking. *Science* **337**: 1333–1336.

Oda Y, Fukuda H. **2013**. Rho of Plant GTPase Signaling Regulates the Behavior of Arabidopsis Kinesin-13A to Establish Secondary Cell Wall Patterns. *The Plant Cell* **25**: 4439–4450.

Oda Y, Iida Y, Nagashima Y, Sugiyama Y, Fukuda H. **2015**. Novel coiled-coil proteins regulate exocyst association with cortical microtubules in xylem cells via the conserved oligomeric golgi-complex 2 protein. *Plant and Cell Physiology* **56**: 277–286.

Oehme DP, Downton MT, Doblin MS, Wagner J, Gidley MJ, Bacic A. **2015**. Unique Aspects of the Structure and Dynamics of Elementary I βCellulose Microfibrils Revealed by Computational Simulations. *Plant Physiology* **168**: 3–17.

Ohashi-Ito K, Oda Y, Fukuda H. **2010**. Arabidopsis VASCULAR-RELATED NAC-DOMAIN6 Directly Regulates the Genes That Govern Programmed Cell Death and Secondary Wall Formation during Xylem Differentiation. *The Plant Cell* **22**: 3461–3473.

Omadjela O, Narahari A, Strumillo J, *et al.* 2013. BcsA and BcsB form the catalytically active core of bacterial cellulose synthase sufficient for in vitro cellulose synthesis. *Proceedings of the National Academy of Sciences* **110**: 17856–17861.

Paredez AR, Persson S, Ehrhardt DW, Somerville CR. **2008**. Genetic evidence that cellulose synthase activity influences microtubule cortical array organization. *Plant Physiology* **147**: 1723–1734.

Paredez AR, Somerville CR, Ehrhardt DW. **2006**. Visualization of Cellulose Synthase Demonstrates Functional Association with Microtubules. *Science* **312**: 1491–1495.

Park JI, Ishimizu T, Suwabe K, *et al.* 2010. UDP-glucose pyrophosphorylase is rate limiting in vegetative and reproductive phases in arabidopsis thaliana. *Plant and Cell Physiology* **51**: 981–996.

Pattathil S, Avci U, Miller JS, Hahn MG. **2012**. Immunological Approaches to Plant Cell Wall and Biomass Characterization: Glycome Profiling In: Himmel ME, ed. *Biomass Conversion: Methods and Protocols*. Totowa, NJ: Humana Press, 61–72.

Pear JR, Kawagoe Y, Schreckengost WE, Delmer DP, Stalker DM. **1996**. Higher plants contain homologs of the bacterial celA genes encoding the catalytic subunit of cellulose synthase. *Proceedings of the National Academy of Sciences* **93**: 12637–12642.

Persson S, Paredez AR, Carroll A, *et al.* 2007. Genetic evidence for three unique

components in primary cell-wall cellulose synthase complexes in Arabidopsis. *Proceedings of the National Academy of Sciences* **104**: 15566–15571.

Persson S, Wei H, Milne J, Page GP, Somerville CR. **2005**. Identification of genes required for cellulose synthesis by regression analysis of public microarray data sets. *Proceedings of the National Academy of Sciences* **102**: 8633–8638.

Purushotham P, Cho SH, Díaz-Moreno SM, *et al.* 2016. A single heterologously expressed plant cellulose synthase isoform is sufficient for cellulose microfibril formation in vitro. *Proceedings of the National Academy of Sciences* **113**: 11360–11365.

Rejab NA, Nakano Y, Yoneda A, Ohtani M, Demura T. **2015**. Possible contribution of TED6 and TED7, secondary cell wall-related membrane proteins, to evolution of tracheary element in angiosperm lineage. *Plant biotechnology* **32**: 343–347.

Robinson DG, Jiang L, Schumacher K. **2008**. The Endosomal System of Plants: Charting New and Familiar Territories. *Plant Physiology* **147**: 1482–1492.

Rudolph U. **1987**. Occurrence of rosettes in the ER membrane of young Funaria hygrometrica protonemata. *Naturwissenschaften* **74**: 439.

Rudolph U, Gross H, Schnepf E. **1989**. Investigations of the turnover of the putative cellulose-synthesizing particle “rosettes” within the plasma membrane ofFunaria hygrometrica protonema cells II. Rosette structure and the effects of cycloheximide, actinomycin D, 2.6-dichlorobenzonitrile, bi. *Protoplasma* **148**: 57–69.

Rudolph U, Schnepf E. **1988**. Investigations of the turnover of the putative Cellulose-synthesizing particle “rosettes” within the plasma membrane of Funaria hygrometrica protonema cells - I. Effects of monensin and cytochalasin B. *Protoplasma* **143**: 63–73.

Ruhnow F, Zwicker D, Diez S. **2011**. Tracking single particles and elongated filaments with nanometer precision. *Biophysical Journal* **100**: 2820–2828.

Salnikov V V, Grimson MJ, Delmer DP, Haigler CH. **2001**. Sucrose synthase localizes to cellulose synthesis sites in tracheary elements. *Phytochemistry* **57**: 823–833.

Sampathkumar A, Gutierrez R, McFarlane HE, *et al.* 2013. Patterning and lifetime of plasma membrane-localized cellulose synthase is dependent on actin organization in Arabidopsis interphase cells. *Plant Physiology* **162**: 675–688.

Sanchez-Rodriguez C, Bauer S, Hematy K, *et al.* 2012. CHITINASE-LIKE1/POM-POM1 and Its Homolog CTL2 Are Glucan-Interacting Proteins Important for Cellulose Biosynthesis in Arabidopsis. *The Plant Cell* **24**: 589–607.

Sánchez-Rodríguez C, Ketelaar K, Schneider R, *et al.* 2017. BRASSINOSTEROID INSENSITIVE2 negatively regulates cellulose synthesis in Arabidopsisby phosphorylating

cellulose synthase 1. *Proceedings of the National Academy of Sciences* **114**: 3533–3538.

Sato S, Kato T, Kakegawa K, *et al.* 2001. Role of the Putative Membrane-Bound Endo-1,4-beta-Glucanase KORRIGAN in Cell Elongation and Cellulose Synthesis in Arabidopsis thaliana. *Plant and Cell Physiology* **42**: 251–263.

Saxena IM, Brown RM. **2005**. Cellulose Biosynthesis: Current Views and Evolving Concepts. *Annals of Botany* **96**: 9–21.

Saxena IM, Lin FC, Brown RM. **1990**. Cloning and sequencing of the cellulose synthase catalytic subunit gene of Acetobacter xylinum. *Plant Molecular Biology* **15**: 673–683.

Scheible W-R, Eshed R, Richmond T, Delmer D, Somerville C. **2001**. Modifications of cellulose synthase confer resistance to isoxaben and thiazolidinone herbicides in Arabidopsis Ixr1 mutants. *Proceedings of the National Academy of Sciences* **98**: 10079–10084.

Scheller HV, Ulvskov P. **2010**. Hemicelluloses. *Annual Review of Plant Biology* **61**: 263–289.

Schindelin J, Arganda-Carreras I, Frise E, *et al.* 2012. Fiji: An open-source platform for biological-image analysis. *Nature Methods* **9**: 676–682.

Schneider R, Hanak T, Persson S, Voigt CA. **2016**. ScienceDirect Cellulose and callose synthesis and organization in focus, what's new? *Current Opinion in Plant Biology* **34**: 9–16.

Schneider B, Herth W. **1986**. Distribution of Plasma Membrane Rosettes and Kinetics of Cellulose Formation in Xylem Development of Higher Plants. *Protoplasma* **131**: 142–152.

Schneider R, Tang L, Lampugnani ER, *et al.* 2017. Two Complementary Mechanisms Underpin Cell Wall Patterning during Xylem Vessel Development. *The Plant Cell* **29**: 2433–2449.

Schrick K, Fujioka S, Takatsuto S, *et al.* 2004. A link between sterol biosynthesis, the cell wall, and cellulose in Arabidopsis. *The Plant Journal* **38**: 227–243.

Schuetz M, Benske A, Smith RA, *et al.* 2014. Laccases direct lignification in the discrete secondary cell wall domains of protoxylem. *Plant Physiology* **166**: 798–807.

Schuetz M, Smith R, Ellis B. **2013**. Xylem tissue specification, patterning, and differentiation mechanisms. *Journal of Experimental Botany* **64**: 11–31.

Sethaphong L, Davis JK, Slabaugh E, Singh A, Haigler CH, Yingling YG. **2015**. Prediction of the structures of the plant-specific regions of vascular plant cellulose synthases and correlated functional analysis. *Cellulose* **23**: 145–161.

Simon MLA, Platre MP, Assil S, *et al.* 2014. A multi-colour/multi-affinity marker set to visualize phosphoinositide dynamics in Arabidopsis. *The Plant Journal* **77**: 322–337.

Slabaugh E, Davis JK, Haigler CH, Yingling YG, Zimmer J. **2014**. Cellulose synthases: new insights from crystallography and modeling. *Trends in Plant Science* **19**: 99–106.

Somerville CR. **2006**. Cellulose Synthesis in Higher Plants. *Annual Review of Cell and Developmental Biology* **22**: 53–78.

Song D, Shen J, Li L. **2010**. Characterization of cellulose synthase complexes in Populus xylem differentiation. *New Phytologist* **187**: 777–790.

Synek L, Sekereš J, Žárský V. **2014**. The exocyst at the interface between cytoskeleton and membranes in eukaryotic cells. *Frontiers in Plant Science* **4**: 1–7.

Szyjanowicz PMJ, McKinnon I, Taylor NG, Gardiner J, Jarvis MC, Turner SR. **2004**. The irregular xylem 2 mutant is an allele of korrigan that affects the secondary cell wall of Arabidopsis thaliana. *The Plant Journal* **37**: 730–740.

Taiz L, Zeiger E. **2015**. *Plant Physiology and Development*. Oxford University Press.

Taylor NG. **2007**. Identification of cellulose synthase AtCesA7 (IRX3) in vivo phosphorylation sites—a potential role in regulating protein degradation. *Plant Molecular Biology* **64**: 161–171.

Taylor NG, Howells RM, Huttly AK, Vickers K, Turner SR. **2003**. Interactions among three distinct CesA proteins essential for cellulose synthesis. *Proceedings of the National Academy of Sciences* **100**: 1450–1455.

Taylor NG, Laurie S, Turner SR. **2000**. Multiple Cellulose Synthase Catalytic Subunits Are Required for Cellulose Synthesis in Arabidopsis. *The Plant Cell* **12**: 2529–2539.

Taylor NG, Scheible W-R, Cutler S, Somerville CR, Turner SR. **1999**. The irregular xylem3 Locus of Arabidopsis Encodes a Cellulose Synthase Required for Secondary Cell Wall Synthesis. *The Plant Cell* **11**: 769–779.

Thévenaz P, Ruttimann UE, Unser M. **1998**. A pyramid approach to subpixel registration based on intensity. *IEEE Transactions on Image Processing* **7**: 27–41.

Thole JM, Nielsen E. **2008**. *Phosphoinositides in plants: novel functions in membrane trafficking*.

Thomas LH, Forsyth VT, Sturcova A, *et al.* 2013. Structure of Cellulose Microfibrils in Primary Cell Walls from Collenchyma. *Plant Physiology* **161**: 465–476.

Tominaga M, Ito K. **2015**. The molecular mechanism and physiological role of

cytoplasmic streaming. *Current Opinion in Plant Biology* **27**: 104–110.

Turner SR, Somerville CR. **1997**. Collapsed xylem phenotype of Arabidopsis identifies mutants deficient in cellulose deposition in the secondary cell wall. *The Plant Cell* **9**: 689–701.

Updegraph DM. **1969**. Semi-micro determination of cellulose in biological materials Anal. Biochem. *Analytical Biochemistry* **32**: 420–424.

Vain T, Crowell EF, Timpano H, *et al.* 2014. The Cellulase KORRIGAN Is Part of the Cellulose Synthase Complex. *Plant Physiology* **165**: 1521–1532.

Vandavasi VG, Putnam DK, Zhang Q, *et al.* 2015. A Structural Study of CESA1 Catalytic Domain of Arabidopsis Cellulose Synthesis Complex: Evidence for CESA Trimers. *Plant Physiology* **170**: 123–135.

VanderHart DL, Atalla RH, VanderHart DL, Atalla RH, VanderHart DL. **1984**. Native Cellulose: A Composite of Two Distinct Crystalline Forms. *Science* **223**: 283–284.

Vermeer JEM, van Leeuwen W, Tobeña-Santamaria R, *et al.* 2006. Visualization of PtdIns3 Pdynamics in living plant cells. *The Plant Journal* **47**: 687–700.

Vermeer JEM, Thole JM, Goedhart J, Nielsen E, Munnik T, Gadella TWJ. **2009**. Imaging phosphatidylinositol 4-phosphate dynamics in living plant cells. *The Plant Journal* **57**: 356–372.

Viotti C, Bubeck J, Stierhof Y-D, *et al.* 2010. Endocytic and Secretory Traffic in Arabidopsis Merge in the Trans-Golgi Network/Early Endosome, an Independent and Highly Dynamic Organelle. *The Plant Cell* **22**: 1344–1357.

Vukašinović N, Oda Y, Pejchar P, *et al.* 2017. Microtubule-dependent targeting of the exocyst complex is necessary for xylem development in Arabidopsis. *New Phytologist* **213**: 1052–1067.

Wang J, Howles PA, Cork AH, Birch RJ, Williamson RE. **2006**. Chimeric Proteins Suggest That the Catalytic and/or C-Terminal Domains Give CesA1 and CesA3 Access to Their Specific Sites in the Cellulose Synthase of Primary Walls. *Plant Physiology* **142**: 685–695.

Wang W, Vignani R, Scali M, Cresti M. **2006**. A universal and rapid protocol for protein extraction from recalcitrant plant tissues for proteomic analysis. *Electrophoresis* **27**: 2782–2786.

Wardrop AB, Harada H. **1965**. The formation and structure of the cell wall in fibres and tracheids. *Journal of Experimental Botany* **16**: 356–371.

Wardrop AB, Preston RD. **1947**. Organisation of the Cell Walls of Tracheids and Wood

Fibres. *Nature* **160**: 911–913.

Wasteneys GO. **2004**. Progress in understanding the role of microtubules in plant cells. *Current Opinion in Plant Biology* **7**: 651–660.

Wasteneys GO, Fujita M. **2006**. Establishing and maintaining axial growth: Wall mechanical properties and the cytoskeleton. *Journal of Plant Research* **119**: 5–10.

Watanabe Y, Meents MJ, McDonnell LM, *et al.* 2015. Visualization of cellulose synthases in Arabidopsis secondary cell walls. *Science* **350**: 198–203.

Wightman R, Marshall R, Turner SR. **2009**. A cellulose synthase-containing compartment moves rapidly beneath sites of secondary wall synthesis. *Plant and Cell Physiology* **50**: 584–594.

Wightman R, Turner SR. **2008**. The roles of the cytoskeleton during cellulose deposition at the secondary cell wall. *The Plant Journal* **54**: 794–805.

Wightman R, Turner SR. **2010a**. Trafficking of the cellulose synthase complex in developing xylem vessels. *Biochemical Society transactions* **38**: 755–760.

Wightman R, Turner SR. **2010b**. Trafficking of the plant cellulose synthase complex. *Plant Physiology* **153**: 427–432.

Winter H, Huber SC. **2000**. Regulation of sucrose metabolism in higher plants: Localization and regulation of activity of key enzymes. *Critical Reviews in Plant Sciences* **19**: 31–67.

Wong HC, Fear AL, Calhoon RD, *et al.* 1990. Genetic organization of the cellulose synthase operon in Acetobacter xylinum. *Proceedings of the National Academy of Sciences* **87**: 8130–8134.

Xiong G, Li R, Qian Q, *et al.* 2010. The rice dynamin-related protein DRP2B mediates membrane trafficking, and thereby plays a critical role in secondary cell wall cellulose biosynthesis. *The Plant Journal* **64**: 56–70.

Yamaguchi M, Goue N, Igarashi H, *et al.* 2010. VASCULAR-RELATED NAC-DOMAIN6 and VASCULAR-RELATED NAC-DOMAIN7 Effectively Induce Transdifferentiation into Xylem Vessel Elements under Control of an Induction System. *Plant Physiology* **153**: 906–914.

Yamaguchi M, Mitsuda N, Ohtani M, Ohme-Takagi M, Kato K, Demura T. **2011**. VASCULAR-RELATED NAC-DOMAIN 7 directly regulates the expression of a broad range of genes for xylem vessel formation. *The Plant Journal* **66**: 579–590.

Zhang X, Henriques R, Lin S-S, Niu Q-W, Chua N-H. **2006**. Agrobacterium-mediated transformation of Arabidopsis thaliana using the floral dip method. *Nature Protocols* **1**:

641–646.

Zhang D, Hrmova M, Wan CH, *et al.* 2004. Members of a new group of chitinase-like genes are expressed preferentially in cotton cells with secondary walls. *Plant Molecular Biology* **54**: 353–372.

Zhang Y, Nikolovski N, Sorieul M, *et al.* 2016. Golgi-localized STELLO proteins regulate the assembly and trafficking of cellulose synthase complexes in Arabidopsis. *Nature Communications* **7**: 1–14.

Zhao X, Li R, Lu C, Baluška F, Wan Y. **2015**. Di-4-ANEPPDHQ, a fluorescent probe for the visualisation of membrane microdomains in living Arabidopsis thaliana cells. *Plant Physiology and Biochemistry* **87**: 53–60.

Zhong R, Burk DH, Morrison WH, Ye Z-H. **2004**. FRAGILE FIBER3, an Arabidopsis Gene Encoding a Type II Inositol Polyphosphate 5-Phosphatase, Is Required for Secondary Wall Synthesis and Actin Organization in Fiber Cells. *The Plant Cell* **16**: 3242–3259.

Zhong R, Morrison WH, Freshour GD, Hahn MG, Ye Z-H. **2003**. Expression of a Mutant Form of Cellulose Synthase AtCesA7 Causes Dominant Negative Effect on Cellulose Biosynthesis. *Plant Physiology* **132**: 786–795.

Zhong R, Peña MJ, Zhou G-K, *et al.* 2005. Arabidopsis fragile fiber8, which encodes a putative glucuronyltransferase, is essential for normal secondary wall synthesis. *The Plant Cell* **17**: 3390–3408.

Zhu C, Ganguly A, Baskin TI, *et al.* 2015. The Fragile Fiber1 Kinesin Contributes to Cortical Microtubule-Mediated Trafficking of Cell Wall Components. *Plant Physiology* **167**: 780–792.